•UNIVERSITY OF OXFORD•

•DEPARTMENT OF ENGINEERING SCIENCE•

UV-C Short-Range Wireless Quantum Key Distribution

Feng Liu

Balliol College

A thesis submitted for the degree of

Doctor of Philosophy

in the

Department of Engineering Science

Supervisor: Prof. Dominic O’Brien

November 2025

Abstract

The rapid advancement of quantum technology increases the security risks of conventional encryption schemes, such as the Rivest-Shamir-Adleman (RSA) algorithm. Quantum key distribution (QKD) has emerged as a secure cryptographic solution, using Heisenberg’s uncertainty principle and the no-cloning theorem to ensure unconditional security in key exchange. Significant progress has been made in fibre-based and satellite QKD systems, achieving long transmission distances and high secure key rates (SKR). However, short-range wireless QKD remains largely unexplored, primarily due to severe ambient light interference, which degrades system performance and limits practical deployment.

This thesis reports a short-range wireless QKD operating in the ultraviolet-C (UV-C) spectrum, utilizing the solar-blind region to mitigate ambient light interference. A high-sensitivity UV-C receiver was developed using a cooled silicon photomultiplier (SiPM), enabling a 1 Mbit/s optical wireless communication (OWC) link. Subsequently, ultralow photon flux links were demonstrated using a UV-C micro-LED and a single-photon detector (SPD), achieving a maximum data rate of 120 Mbit/s with a minimum transmitted photon number per bit of 7.7. Finally, the world’s first wireless QKD system operating in the UV-C region was implemented, inferring an SKR exceeding 1 Mbit/s. Additionally, the impact of LED-based ambient light and sunlight interference was analysed, and mitigation strategies were proposed to enhance system robustness.

Overall, this work establishes the feasibility of UV-C wireless QKD and provides a foundation for future improvements in ambient light

rejection and real-world deployment.

Acknowledgements

Pursuing a DPhil has been an extraordinary journey, filled with challenges, discoveries, and profound learning moments. This thesis would not have been possible without the support and guidance of many individuals, to whom I owe my deepest gratitude.

First and foremost, I would like to extend my sincerest appreciation to my supervisor, Professor Dominic O'Brien, for his invaluable mentorship, insightful advice, and unwavering support throughout my DPhil research journey. His depth of knowledge and dedication to academic excellence are truly inspiring. His guidance has not only shaped my work but has also refined my approach to problem-solving and scientific exploration. I am immensely grateful for his patience, encouragement, and support, which have enabled me to navigate the field of optical communications with growing confidence and mastery. It has been an honour to work under his supervision and to be a member of the Optical Wireless Communications (OWC) Group at the University of Oxford.

I would also like to express my heartfelt gratitude to my colleagues in the OWC Group. The intellectual exchanges, collaborative efforts, and shared moments of triumph and frustration have profoundly enriched my experience. The support and camaraderie of this brilliant team have made every challenge more manageable and every success more meaningful. In particular, I am deeply thankful to Andy Schreier for his selfless guidance when I first embarked on my DPhil journey, feeling lost and uncertain, and to James Farmer for his crucial technical and moral support throughout my studies.

Beyond the academic sphere, I am profoundly grateful to my family and friends, whose unwavering encouragement has been the foundation of my DPhil journey. To my parents, your boundless love, patience, and support have made all this possible. Your belief in me has been my greatest source of strength, and I will always endeavour to make you proud. To my friends, both near and far, thank you for your companionship, laughter, and countless moments of support. The memories we created in Oxford will forever hold a special place in my heart, and I look forward to more moments we will share in the future.

Finally, my deepest and most profound gratitude goes to my belove, Shuwen Yin. Meeting her, getting to know her, and falling in love with her in Oxford has been the most extraordinary fortune of my life. Her unwavering choice and love have been an endless source of motivation on my path. I am the big bunny and will say to my little bunny all my life: “I love you to the moon and back”. This thesis is as much hers as it is mine, and I dedicate it entirely to her with all my heart.

Publications

[1] **F. Liu**, J. Farmer, A. Schreier, G. Faulkner, H. Chun, W. Matthews, Z. Wang and D. O'Brien, "Ultra-sensitive UV solar-blind optical wireless communications with an SiPM," *Optics Letters,* vol. 48, no. 20, pp. 5387-5390, 2023/10/15 2023.

[2] **F. Liu**, J. Farmer, G. Faulkner, Z. Wang, J. Wang, D. O'Brien, E. Xie, J. Hill, J. Herrnsdorf, J. McKendry and M. Dawson, "10 Mbit/s UV Solar-Blind OWC at 30 Photons Per Bit," in *2024 Conference on Lasers and Electro-Optics (CLEO)*, 5-10 May 2024, pp. 1-2.

[3] **F. Liu**, J. Farmer, G. Faulkner, J. McKendry, E. Xie, Q. Zheng, Z. Wang, J. Wang, J. Hill, J. Herrnsdorf, M. Dawson and D. O'Brien, "Ultralow Photon Flux OWC Links Using UV-C Single-Photon Detection," *Laser & Photonics Reviews*, vol. n/a, no. n/a, p. 2401804.

[4] **F. Liu** et al., "UV-C Wireless Quantum Key Distribution," *Nature Communications* (Submitted).

Contents

Chapter 1:

Introduction

1.1 OVERVIEW

With the increasing demand for wireless capacity, optical wireless communication (OWC) is regarded as a promising technology for providing wireless access services in future wireless communication systems because of its broad bandwidth, low latency and lack of regulatory requirements [1-3]. In comparison to the 1 Tbit/s peak data rate target for next-generation wireless systems (6G) [4], OWC systems with data rates of Tbit/s have already been demonstrated, with peak values reaching 100 Tbit/s [5-8]. However, with the rapid development of quantum computing, encryption and data security are increasing concerns for future secure wireless communications [9, 10]. In a typical communication system, traditional asymmetric encryption algorithms, such as the Rivest-Shamir-Adleman (RSA) algorithm, elliptic-curve cryptography (ECC) and Diffie-Hellman (DH) key exchange, are used to provide security [11-13]. Asymmetric encryption algorithms are based on the principle that solving certain mathematical problems, including large integer factorisation and discrete logarithms, is computationally infeasible for classical computers. However, these traditional encryption algorithms may not remain secure in the long term, given the development of quantum computing [14-19]. This is because Shor's algorithm provides a method for quantum computers to efficiently solve the large integer factorisation problem and the discrete logarithm problem [20]. Classical algorithms require exponential time to solve these problems as the key size increases, but quantum computers running Shor's algorithm can solve them in polynomial time. This means that a quantum computer with sufficient scale could derive the private key from the public key, effectively breaking the encryption. As a result, the data encrypted or signed with these schemes could be intercepted by quantum-capable eavesdroppers.

To prevent information interception against quantum computing, quantum cryptography offers a new paradigm for secure communications even in the presence of quantum computers [21]. It primarily includes quantum key distribution (QKD) and post-quantum cryptography (PQC), two complementary approaches that aim to ensure long-term security in the quantum era [21-27]. QKD provides theoretically full security to generate secure keys and encrypt data based on fundamental quantum mechanics, including Heisenberg's uncertainty principle and the no-cloning theorem [21-24]. Heisenberg's uncertainty principle states that accurately measuring a pair of conjugate properties, such as the position and momentum of a photon, simultaneously is impossible [28, 29]. This is because measuring one property of one particle inevitably perturbs it and thus makes the measurement of another property inaccurate. The non-cloning theorem states that exactly replicating arbitrary unknown quantum states is impossible [30-34]. Thus, in a QKD system, the eavesdropper (Eve) can only attempt to eavesdrop and measure the quantum states directly (she cannot accurately measure and replicate states) from the transmitter (Alice) and transmit these states to the receiver (Bob). Thus, eavesdropping will change the quantum states, allowing the transmitter and receiver to detect eavesdropping by a change in the link error rate. PQC resists attacks from quantum computers based on mathematical problems believed to be hard even for quantum computers, such as lattice-, code-, hash-, and multivariate-based problems [35-38]. Unlike QKD, PQC can be deployed using conventional hardware without requiring quantum channels, making it more accessible to integrate into existing communication networks. PQC is especially suitable for applications such as digital signatures and public-key encryption and is expected to operate with QKD to create robust and flexible quantum-secure communication systems.

This thesis focuses on the development of QKD. The first QKD protocol was the BB84 protocol which was proposed by C. H. Bennett and G. Brassard in 1984 [23]. In the past approximately 4 decades, different types of QKD protocols have been developed, including Discrete-Variable QKD (DV-QKD), Coherent-One Way QKD (COW-QKD), Continuous-Variable QKD (CV-QKD), Measurement-Device-Independent QKD (MDI-QKD) and Twin-Field QKD (TF-QKD) [23, 39-41]. For QKD experimental demonstrations, a maximum distance of more than 1000 km and a secure key rate (SKR) of over 110 Mbit/s have been achieved [42, 43]. However, previous QKD research has mainly focused on fibre-based or satellite systems [42-45], and there are a very limited number of short-range wireless QKD demonstrations [46-50].

Short-range wireless QKD has the potential to provide encryption services for wireless information in mobile devices in the future, such as smartphones and wireless payments [47]. However, short-range wireless QKD faces the challenge of severe ambient light interference, mainly due to sunlight [46-50]. According to the sunlight spectrum near the ground [51], there exists a “solar-blind” region in the ultraviolet-C (UV-C) band (less than 280 nm). The sunlight irradiance in this region is extremely low because of absorption by the ozone layer in the atmosphere. Therefore, a short-range wireless QKD system operating in daylight in the UV-C region is feasible.

However, available devices operating in the UV-C region are very limited, especially high-bandwidth UV-C transmitters and a high-sensitivity UV-C receiver. To address the challenges from individual components to the complete QKD system, this thesis details the development of the UV-C transmitter and receiver, and a demonstration of a UV-C wireless QKD system. The layout of this thesis is outlined below.

1.2 LAYOUT OF THE THESIS

In Chapter 2, the theory and background of the QKD are provided. The structure and scheme of QKD systems are presented. Then, different QKD protocols are listed and compared, followed by summarized wireless QKD demonstrations. Additionally, the potential of operating wireless QKD in the UV-C region is analysed.

In Chapter 3, ultra-sensitive UV solar-blind OWC links based on a commercial UV-C LED and a high-sensitivity receiver are reported. The receiver was designed based on a cooled silicon photomultiplier (SiPM). A 1 Mbit/s UV-C OWC link was demonstrated, with an average received photon number per bit of approximately 40. The successful design of the high-sensitivity receiver paves the way for the receiver design for the final UV-C wireless QKD systems. Results are published in [52] (listed below).

F. Liu, J. Farmer, A. Schreier, G. Faulkner, H. Chun, W. Matthews, Z. Wang and D. O’Brien, "Ultra-sensitive UV solar-blind optical wireless communications with an SiPM," *Optics Letters*, vol. 48, no. 20, pp. 5387-5390, 2023/10/15 2023.

In Chapter 4, ultralow photon flux links are reported. These are based on a UV-C micro-LED and a UV-C single-photon detector (SPD). The UV-C SPD achieved a lower dark count rate (DCR) compared to the receiver described in Chapter 3, due to a lower temperature and a smaller active area. A maximum data rate of 120 Mbit/s and a minimum transmitted average photon number per bit of 7.7 was demonstrated. Moreover, a 500 MHz repetition rate single-photon link was demonstrated, showing the potential of building a UV-C wireless QKD. Results are reported in [53, 54] (listed below):

F. Liu, J. Farmer, G. Faulkner, Z. Wang, J. Wang, D. O'Brien, E. Xie, J. Hill, J. Herrnsdorf, J. McKendry and M. Dawson, "10 Mbit/s UV Solar-Blind OWC at 30 Photons Per Bit," *in 2024 Conference on Lasers and Electro-Optics (CLEO)*, 5-10 May 2024, pp. 1-2.

F. Liu, J. Farmer, G. Faulkner, J. McKendry, E. Xie, Q. Zheng, Z. Wang, J. Wang, J. Hill, J. Herrnsdorf, M. Dawson and D. O'Brien, "Ultralow Photon Flux OWC Links Using UV-C Single-Photon Detection," *Laser & Photonics Reviews*, vol. n/a, no. n/a, p. 2401804.

Chapter 5 describes the design and demonstration of a UV-C wireless B92 QKD system, which to the best of our knowledge is the first demonstration operating in the UV-C region. The modelling of the system is presented and then details of the demonstration are reported. The system was operated with an inferred SKR of over 1 Mbit/s. Details of strategies to reject ambient light from LEDs and sunlight are proposed, together with a detailed analysis. The corresponding publications are in preparation and listed below:

***F.* Liu** et al., "UV-C Wireless Quantum Key Distribution," *Nature Communications* (Submitted).

In Chapter 6, the contributions of this thesis are summarized, and conclusions are drawn. Future work on the potential improvement of ultralow photon flux links and QKD links is discussed.

Chapter 2:

Literature Review

This Chapter begins by introducing the architecture and operation of QKD systems. Then, different protocols are analysed and compared, highlighting their respective advantages and disadvantages in terms of performance and implementation. State-of-the-art wireless QKD demonstrations are reviewed and summarized, identifying UV-C regions that remain underexplored. Finally, the potential of pursuing a UV-C wireless QKD system is discussed.

2.1 QKD ARCHITECTURE

A block diagram of a QKD scheme, consisting of a transmitter (Alice), a receiver (Bob) and channels between them, is illustrated in Fig. 2.1. The goal of a QKD system is to generate secure keys that can be used to encrypt information data. Photons are sent from Alice to Bob in the physical layer. Sifted keys are then obtained by matching compatible transmitted and received photons. Error correction removes errors in the sifted keys, and privacy amplification eliminates the information intercepted by an eavesdropper (Eve). A detailed description of the process is provided in the following sections.

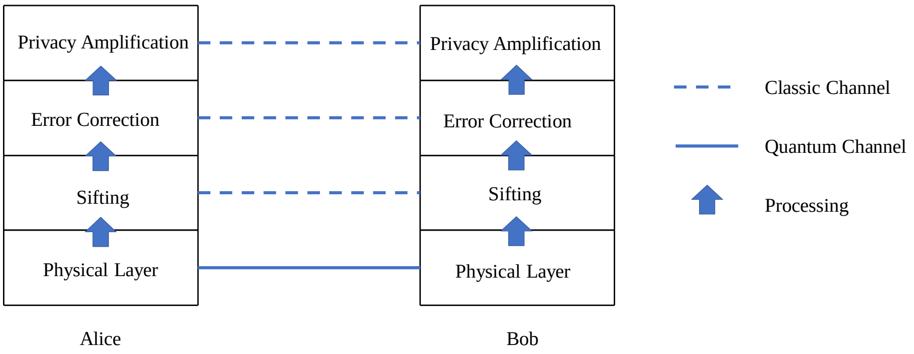

Figure 2.1 QKD scheme block diagram

2.1.1 Physical Layer

Alice uses single-photon sources to generate and transmit photons. However, ideal single-photon sources are unavailable, and weak light sources serve as an alternative. A weak light source is typically implemented as a light source with an attenuator to reduce the average number of emitted photons in each qubit to less than one. The transmitted photons are randomly encoded in one of several bases. The type of basis varies across different QKD systems, and the use of polarization, phase, or orbital angular momentum (OAM) has all been demonstrated [23, 55, 56]. Bob implements a corresponding detection channel for each basis. One of these bases is randomly selected to decode the received photons using SPDs. An SPD-based receiver typically consists of a high-sensitivity photodetector and subsequent amplification.

The channel between Alice and Bob can be classified into either a guided (predominantly fibre-based) or free-space channel. The channel loss in fibre-based QKD comes from material absorption, bending, fibre splices and fibre connections, while geometrical loss and atmospheric attenuation are the primary contributors in free space QKD [57]. Beyond channel loss, fibre-based systems are also affected by noise sources, mainly spontaneous Raman scattering

(SRS) induced by co-propagating classical signals [58, 59]. SRS is particularly prominent in wavelength-division multiplexed systems where quantum and classical signals share the same fibre. Free-space systems, on the other hand, experience noise from ambient light, which increases background noise at the receiver, as well as beam wandering and wavefront distortion caused by atmospheric turbulence [60-62]. Thus, fibre-based QKD provides stable and environmentally isolated links suitable for metropolitan networks, while free-space QKD offers greater flexibility for infrastructure-limited environments, such as ground-to-satellite or mobile links.

2.1.2 Sifting

Bob sends his chosen decoding bases to Alice, who compares them with the encoding bases. Alice then informs Bob of the incompatible bases, and they discard the corresponding qubits. The remaining qubits with compatible bases are referred to as the sifted keys.

2.1.3 Error Correction

The sifted keys still have residual errors because of the imperfection in data transmission, detection and processing. Thus, error correction, also known as information reconciliation in QKD, is carried out to make sure that the sifted keys in Alice and Bob are the same [63, 64]. Unlike conventional communications, where error correction aims to recover the information from noisy data, QKD transmits random numbers rather than live data. As a result, QKD error correction focuses on reconciling minor discrepancies between the two parties’ sifted keys, rather than reconstructing the information data. Low-density parity code check (LDPC) codes are typically applied with a small quantum bit error rate (QBER ≤ 5%), as their performance theoretically approaches the Shannon limit [65]. When the QBER is relatively high (QBER > 5%), alternative methods, such as segmented error correction and cascade protocols, can be employed, or the corresponding sifted keys can be discarded to ensure security [66, 67]. Removing these errors does not affect the overall randomness of keys, ensuring their security. The keys after error correction are termed corrected keys.

2.1.4 Privacy Amplification

Guaranteeing that Alice and Bob have the same keys is not enough, because the influence of the eavesdropper may still exist. However, Alice and Bob cannot identify which qubits have been intercepted by Eve in the corrected keys. Privacy amplification addresses this issue by reducing Eve's knowledge to a negligible level using universal hash functions [68-74]. By applying a universal hash function, corrected keys with and without eavesdropping will produce entirely different outputs, due to the sensitivity of the hash function. Thus, the parts possibly known by Eve are effectively removed. This means that Alice and Bob compress the key length to ensure that any partial knowledge Eve may have is eliminated.

2.1.5 Attacks

The number of photons (emitted by a weak light source) in each qubit follows a Poisson distribution. As a result, a small proportion of qubits contain more than one photon, which makes a QKD system more vulnerable to attacks, such as a photon-number-splitting (PNS) attack [75-77]. In a PNS attack, Eve allows one photon to pass through to Bob and intercepts all other photons in each qubit. One method to reduce the impact of PNS attacks is using decoy states [78]. Eavesdropping on the communication link can be discovered by a rising QBER [78, 79].

2.2 QKD PROTOCOLS

2.2.1 DV-QKD Protocols

This section introduces different DV-QKD protocols, including BB84, B92, six-state, SARG04, KMB09, T12 and S13, along with their respective advantages and disadvantages. BB84 is the most widely studied and implemented, offering strong security but lower efficiency in noisy environments. B92 simplifies the protocol by using fewer states, but it is more sensitive to noise. Six-State and SARG04 enhance security compared to BB84 but at the cost of increased hardware complexity and lower efficiency. KMB09 and T12 introduce advanced techniques to improve noise resistance, in cost of requiring more complex implementations. Additionally, T12 offers improved transmission efficiency.

2.2.1.1 BB84 Protocol

The BB84 protocol is the first QKD protocol, which was proposed in 1984 by C. H. Bennett and G. Brassard [23]. BB84 is straightforward to implement, with many experimental validations [43, 80-87]. However, BB84 has drawbacks in high-noise and long-distance applications, where error rate increases and key generation efficiency decreases.

In this protocol, Alice first prepares two random bit strings a and b. The first string a represents the bit values (0 or 1) that Alice wants to send to Bob. The second string b is applied to encode the bit in two different bases (the X-basis and Y-basis), and each basis contains two states representing 0 and 1, respectively. The description of these bases is illustrated in Fig. 2.2. The rectilinear basis includes a horizontal state (0°) and a vertical state (90°), and the diagonal basis contains a diagonal state (45°) and an anti-diagonal state (135°).

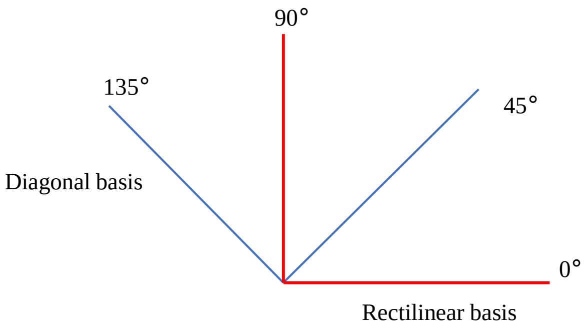

Figure 2.2 Bases used in BB84

The encoded bits are called qubits and are transmitted to Bob via quantum channels. Bob chooses the bases randomly to decode the received qubits and obtains a measured string. Then, the sifting, error correction and privacy amplification are performed to generate the final secure keys. The process of BB84 can be summarized as follows:

- Alice chooses random bases to encode a string of generated bits to create qubits. Then, the qubits are sent to Bob via the quantum channel.
- Bob receives qubits and applies a random basis to measure each qubit. The measurement result is called the raw key.
- Bob sends his chosen bases to Alice, and Alice compares them with the bases she used. Then, Alice tells Bob which of the bases he used are incorrect. The corresponding bits are discarded, and the others are reserved. The reserved bits are known as the sifted key.
- Bob sends part of his sifted keys to Alice, and Alice calculates

the error rate, which is called QBER. Then, error correction, typically using an LDPC code, is carried out to remove the errors in the sifted keys. The generated bits are called the corrected keys.

- Based on the calculated QBER, privacy amplification is undertaken using universal hash functions to remove the eavesdropped information by Eve and obtain final secure keys.

A block diagram of a typical polarization-based BB84 QKD system is shown in Fig. 2.3 [88]. There are four light sources in Alice, which generate photons polarized at 0°, 45°, 90° and 135°, respectively. Only one light source is randomly chosen to be triggered at the same time. Then, the generated photons are combined by three beam splitters (BSs). An attenuator is installed to reduce the number of photons in each qubit to less than one. The photons emitted from Alice travel through the quantum channel to Bob. A BS randomly allocates received photons to two polarizing beam splitters (PBSs), with one waveplate in front of one of these two PBSs. Then, photons are detected by four SPDs (each SPD detects photons in one of four polarization states) behind PBSs.

Apart from the polarization-based BB84 system, a phase-based BB84 system is an alternative way to realize the protocol in practice [89, 90]. A corresponding block diagram is shown in Fig. 2.4. In Alice, a BS splits light from a source into two paths: a short arm with a delay module and a long arm with a phase modulator φ_a. The light through two paths is combined by a BS and attenuated for transmission. In Bob, by using a BS, the photons passing Alice's long arm go into Bob's short (L-S route) arm and vice versa (S-L route). The delay modules in Alice and Bob ensure that the two routes are the same length. The photons sent by Alice are detected by only one of the two SPDs with a probability based on the phase difference $\Delta\varphi=\varphi_a-\varphi_b$.

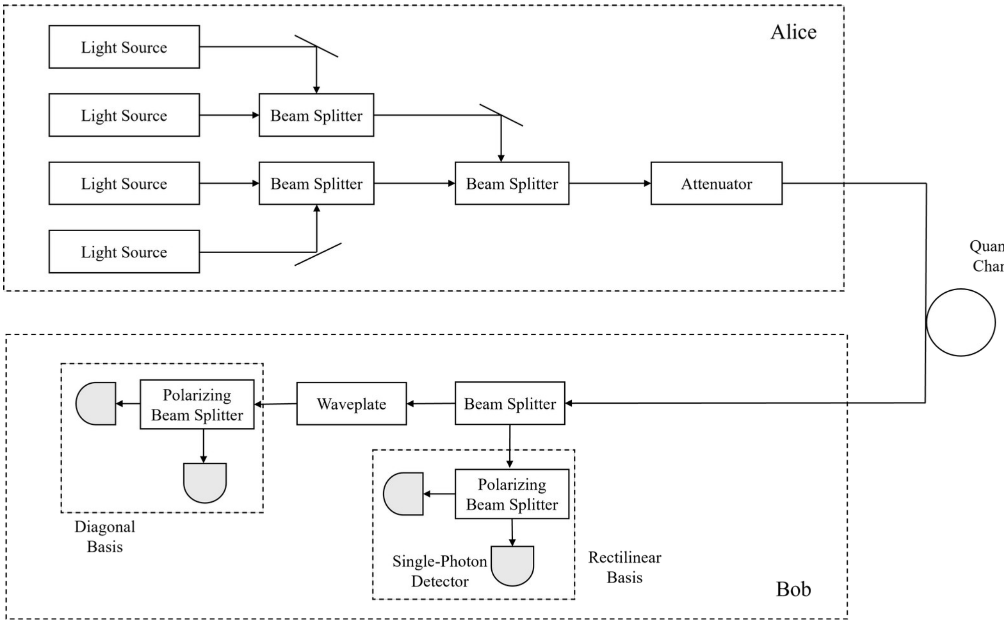

Figure 2.3 Block diagram of a typical polarization-based BB84 QKD system

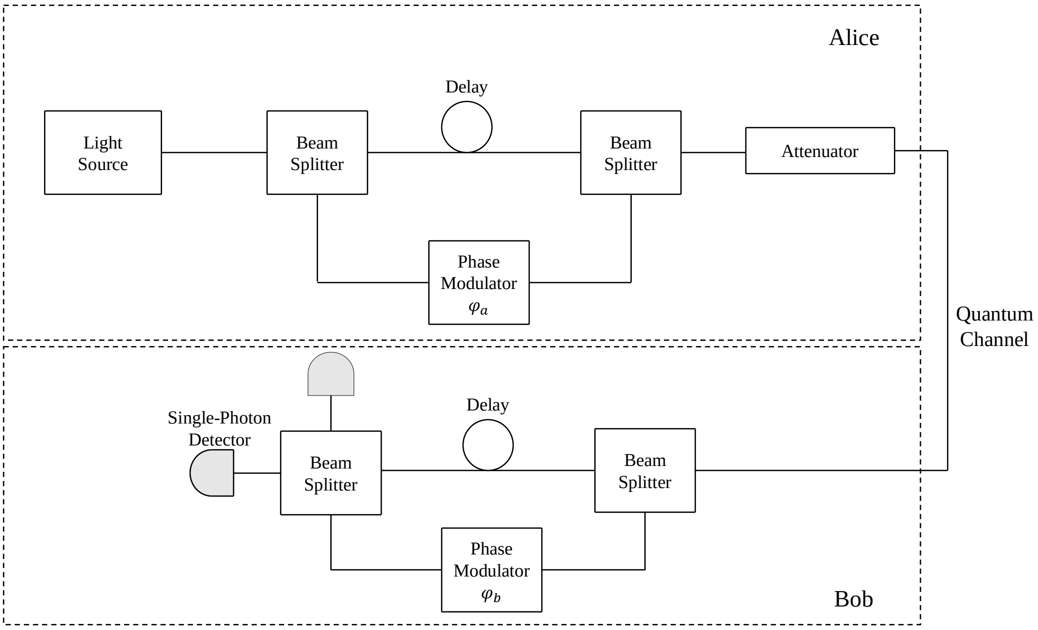

Figure 2.4 Block diagram of a typical phase-based BB84 QKD system

2.2.1.2 B92 Protocol

In 1992, Bennett found that only two nonorthogonal states were enough for quantum communications, rather than using four states in the BB84 protocol [90]. As a result, B92 is more resource-efficient, requiring fewer components such as half light sources and half SPDs, though the key generation rate is reduced by approximately half. Moreover, the impact of noise in B92 is greater, which makes it harder to implement in practice. This is because B92 relies on unambiguous state measurement, where each SPD detection directly corresponds to a key bit. In noisy channels, the nonorthogonal states become harder to distinguish, thereby increasing the error rate. By contrast, BB84 benefits from basis comparison and redundancy in state choices, which enhances its noise resistance. Thus, B92 is more sensitive to noise, leading to higher QBER in practice.

A block diagram of a typical polarization-based B92 QKD system is shown in Fig. 2.5. In Alice, there are only two light sources, generating photons polarized at 0° (H, horizontal) and 45° (D, diagonal), respectively. Then, the generated photons are combined by a BS, and an attenuator reduces the number of photons in each qubit to less than one. In Bob, a BS randomly allocates received photons to two polarizers, selecting photons with specific polarizations (V, vertical or A, anti-diagonal). Then, photons are detected by two SPDs.

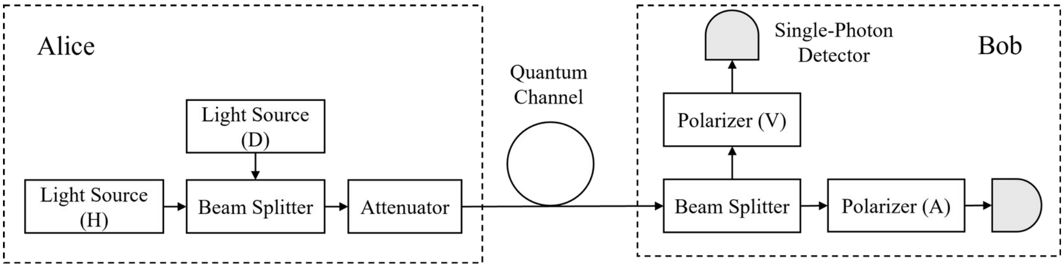

Figure 2.5 Block diagram of a polarization-based typical B92 QKD system

The working principle of the B92 protocol is shown in Table 2.1. Alice first randomly chooses one of the horizontal (“0”) and diagonal (“1”) states to generate a qubit sequence. Then, the generated qubits are sent to Bob via the quantum channel. To measure one qubit, Bob randomly chooses a state (vertical or anti-diagonal). When the qubit is received and the measurement result is (↑), Bob knows the qubit sent by Alice is → ( ). Sifting is omitted and Bob keeps all received bits.

Table 2.1 Working principle of the B92 protocol

Bit sequences in Alice	0	1	1	0	0	1
States in Alice	→			→	→	
States in Bob	↑	↑	↑			
Reserved or not	N	Y (50%)	N (50%)	Y (50%)	N (50%)	N
Measurement result		1		0		

2.2.1.3 Six-State Protocol

The six-state protocol improves upon BB84 by using six states for encoding and decoding [91, 92]. Compared to BB84, the two additional bases are a right-circular state and a left-circular state. This protocol provides better noise resistance and reduces the alignment complexity[46]. However, the key generation rate is lower.

2.2.1.4 SARG04 Protocol

The SARG04 protocol is another version of the BB84 protocol [77, 93, 94], which provides better robustness against channel loss and eavesdropping and can be compatible with BB84 hardware. However, SARG04 is more complex in terms of protocol design and implementation.

The SARG04 protocol utilizes a different sifting procedure from the BB84 protocol. Instead of revealing the bases used to encode qubits, Alice selects one state from the rectilinear basis and one state from the diagonal basis and sends them to Bob. For Bob, his goal is to distinguish which state is the correct one. Based on his measurement, he checks which states his result is consistent with. If the result is consistent with both states, the bit will be discarded because Bob cannot know which state is used by Alice. If one of the states is inconsistent with Bob's measurement result, he will keep this bit and extract the correct sifting key. For example, Alice generates qubits in rectilinear basis, including a horizontal state ("0") and a vertical state ("1"), and a diagonal basis, including a diagonal state ("0") and an anti-diagonal state ("1"). Suppose that a horizontal state is sent from Alice. Then, she publicly announces two "0" states (horizontal state and diagonal state). Depending on the basis Bob applies to measure the qubit, two situations occur:

- If Bob uses the rectilinear basis to measure the received qubit, the measurement result must be 0. This result is obviously consistent with the transmitted state. However, if the transmitted state is the diagonal state, the measurement result can also be the horizontal state with a probability of 50 %. Therefore, Bob cannot know which state is sent by Alice. This bit is invalid and discarded.

- If Bob uses the diagonal basis to measure the received qubit, he can obtain a diagonal state or an anti-diagonal state, each with a probability of 50 %. Thus, if the outcome is the diagonal state, it can be obtained by transmitting either the horizontal state or the diagonal state. However, when the outcome is the anti-diagonal state, Bob can be certain that the correct state is the horizontal state because the anti-diagonal state can never be obtained from the diagonal state. Therefore, Bob announces that this bit is valid and extracts a sifting key.

2.2.1.5 KMB09 Protocol

The KMB09 protocol builds on BB84 by introducing decoy states to mitigate the impact of PNS attacks and improve performance in high channel loss scenarios. However, the use of decoy states adds complexity to implementation and post-processing [95].

2.2.1.6 T12 Protocol

The T12 protocol is designed based on BB84 and adjusts the usage rates of two bases [96]. Thus, the key generation rate is improved, but the device calibration and system implementation are more complex.

Table 2.2 A survey of DV-QKD protocols

Protocol	Year	Advantage	Disadvantage	Reference
BB84	1984	Easy to understand and widely implement	Limited performance with high-loss and long-distance	C. H. Bennett and G. Brassard [23]
B92	1992	Resource-efficient	Low key generation rate and sensitive to noise	C. H. Bennett [90]
Six-state	1998 &1999	Robust against noise and mitigate alignment complexity	Low key generation rate	D. Bruß [91] & H. Bechmann-Pasquinucci and N. Gisin [92]

SARG04	2004	Robust against channel loss and eavesdropping, and compatible with BB84 hardware	Complex protocol design and implementation	V. Scarani, A. Acín, G. Ribordy and N. Gisin [77]
KMB09	2009	Mitigate PNS attacks and robust against path loss	Complex implementation and post-processing	M. Mubashir Khan, M. Murphy and A. Beige [95]
T12	2013	High key generation rate	Complex device calibration and system implementation	M. Lucamarini *et al.* [96]

In the BB84 protocol, the number of qubits encoded by each basis is identical (50 % on the *X* basis and 50 % on the *Y* basis). Then, Bob chooses one of the two bases randomly to measure every qubit, so the possibility of getting the correct outcome is 50 %. Thus, only $50\%\times 50\%+50\%\times 50\%=50\%$ of initial qubits can be converted into raw keys. However, the numbers of qubits encoded and decoded in two bases are different in the T12 protocol. For instance, the usage rates of *Y* basis and *X* basis in both Alice and Bob are 80 % and 20 %, respectively. The conversion ratio from initial qubits to raw keys is $80\%\times 80\%+20\%\times 20\%=68\%$ which is 18 % higher than standard BB84 protocol. Further increase in the number of qubits in the *Y* basis can further increase the length of raw keys. 1/16 of total qubits for the *X* basis and 15/16 for the *Y* basis were applied in [96] and nearly 88.3 % of initial qubits can be used to generate raw keys.

A summary of the above DV-QKD protocols is shown in Table 2.2.

2.2.2 COW-QKD Protocol

In 2004, D. Stucki, N. Brunner, N. Gisin, V. Scarani, and H. Zbinden proposed the COW-QKD protocol [97, 98] and a wireless QKD demonstration based on COW-QKD has been demonstrated

[48]. The COW-QKD protocol obtains secure keys based on measuring the arrival time of qubits [99]. A typical block diagram of the COW-QKD system is illustrated in Fig. 2.6.

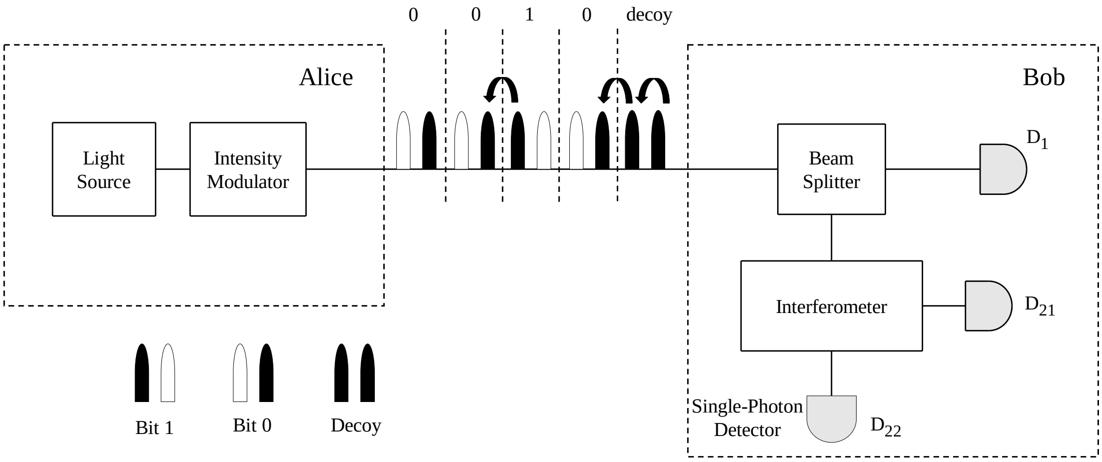

Figure 2.6 A typical block diagram of a COW-QKD syste

Alice prepares non-empty pulses with an average photon number μ or empty pulses by using a coherent light source and an intensity modulator. Each bit “1” or “0” contains an empty pulse and a non-empty pulse: $|1_k\rangle=|\sqrt{\mu}\rangle_{2k-1}-|0\rangle_{2k}$, $|0_k\rangle=|0\rangle_{2k-1}-|\sqrt{\mu}\rangle_{2k}$, where k is the bit number. Bob obtains the bit value by measuring the arrival time of non-empty pulses. Most of the pulses go through the BS in Bob to D_1 to generate raw keys and the rest are reflected to the interferometer to check the coherence both within a bit and across bit separations. By adding decoy states, checking coherence can detect a PNS attack from Eve.

2.2.3 CV-QKD Protocols

There are two kinds of CV-QKD protocols: the squeezed-state Gaussian protocol [100] and the coherent-state Gaussian protocol [39]. This section focuses on the coherent-state Gaussian protocol because it is easier to implement and more robust against noise and loss, making it more suitable for practical applications.

The coherent-state CV-QKD protocol was proposed by F. Grosshans and P. Grangier in 2002 [39]. The protocol operates as follows:

- Alice generates two random numbers x_A and p_A. These both obey a Gaussian distribution with variance $V_A N_0$ and mean 0, where V_A is an integer and N_0 is the variance of the noise. Then, x_A and p_A are respectively applied to modulate the amplitude and phase of a coherent laser beam to generate a coherent state to be transmitted to Bob.

- Bob receives the coherent states and measures either X or P randomly. X and P can be seen as bases for encoding and decoding the amplitude value x_A and the phase value p_A.

- Bob tells Alice about X or P that he measured. Alice compares the bases she used with Bob's and removes incompatible ones.

- Error correction and privacy amplification are carried out to further exclude the errors and Eve's knowledge to obtain final secure keys.

The implementation of coherent CV-QKD can be divided into two categories: homodyne and heterodyne [100-103]. Fig. 2.7 shows a block diagram for a real coherent CV-QKD system using the homodyne detection scheme [101]. In Alice, a weak coherent light source is used to generate initial coherent laser beams which are then passed through a BS. The optical power from each of the two paths of the BS is different. Only a small portion of light goes into the I/Q modulator and is modulated using Gaussian random numbers x_A and p_A. Then, the light from the two paths is multiplexed together to be transmitted to Bob. In Bob, the received light is separated into two paths by a demultiplexer. The light in one path passes through a phase modulator and combines with the light from another path via a BS. A balanced detector is then used to measure the amplitude or phase.

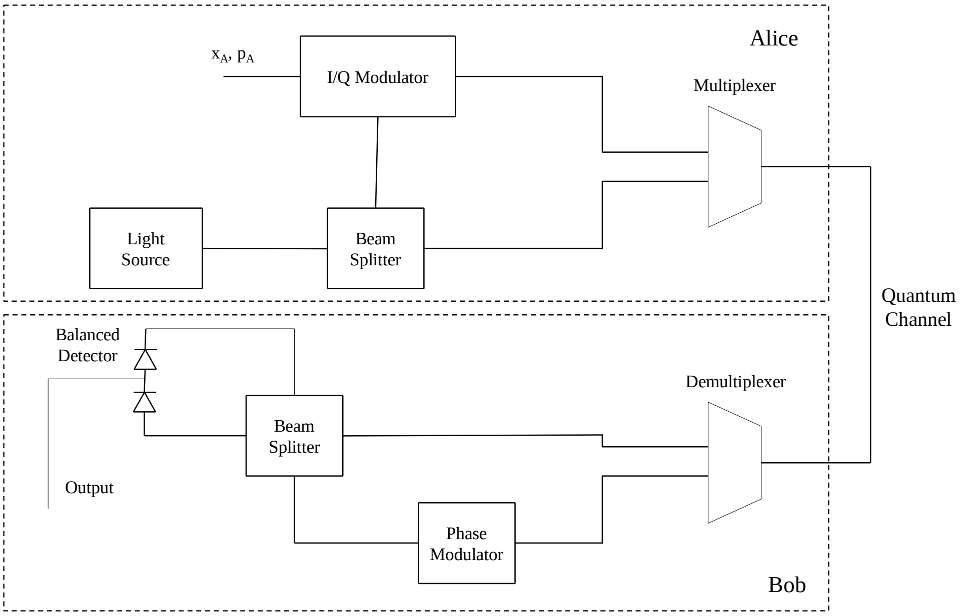

Figure 2.7 A block diagram for a coherent-state Gaussian protocol using the homodyne detection

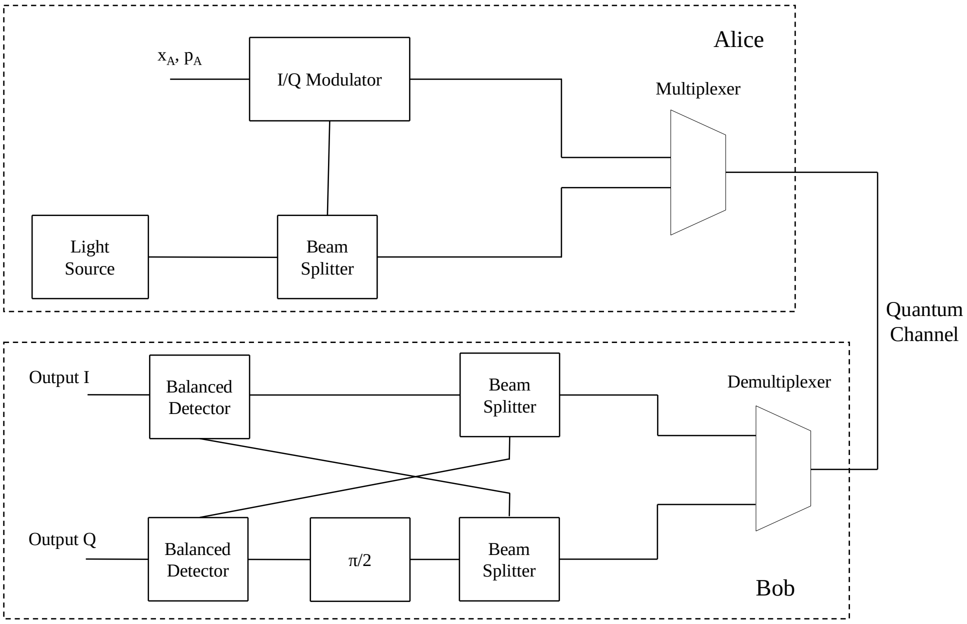

Figure 2.8 A block diagram for a coherent-state Gaussian protocol using the heterodyne detection

The heterodyne detection is another approach for coherent CV-QKD protocols [102]. A block diagram of the heterodyne system is shown in Fig. 2.8. The main difference when compared with the homodyne structure is the structure of the receiver that Bob uses. A 90-degree hybrid is used to process received light and two balanced detectors are installed to measure both the in-phase and orthogonal components (X and P components). Therefore, x_A and p_A can both be obtained so that the secure key generation rate is increased compared to measuring one quadrature in homodyne detection.

2.2.4 MDI-QKD Protocol

In 2012, the MDI-QKD protocol was proposed by H. Lo, M. Curty, and B. Qi, in order to eliminate detector side-channel attacks [104]. An intermediate station, referred to as “Charlie”, is introduced between Alice and Bob as a receiver to collect and process the quantum information sent from Alice and Bob. The MDI-QKD protocol offers the advantage of achieving twice the communication distance compared to DV-QKD, COW-QKD and CV-QKD.

A typical block diagram of an MDI-QKD system is shown in Fig. 2.9. Alice and Bob both generate qubits and send them to Charlie simultaneously. The structures of Alice and Bob are the same. Each has a weak coherent light source, a polarization modulator and an intensity modulator. Charlie collects and measures the Bell state of qubits from Alice and Bob simultaneously using one BS, two PBSs and four SPDs. Only when two specific SPDs are triggered, the Bell state measurement is successful. The Bell state ¿ is obtained when D_{11} and D_{22} or D_{21} and D_{12} are triggered. When D_{11} and D_{12} or D_{21} and

D_{22} are clicked, the measured Bell state is ¿. Then, Charlie announces the measurement results publicly. Alice and Bob keep the corresponding successful bits and discard the rest. In addition, either Alice or Bob needs to flip her or his data to guarantee the bit strings in Alice and Bob are the same.

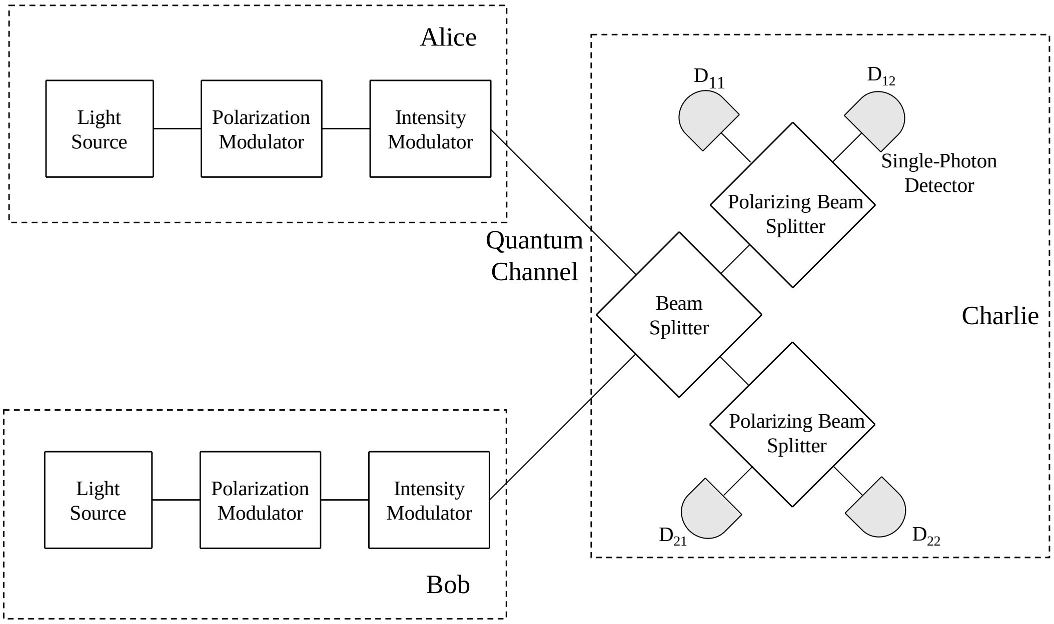

Figure 2.9 A typical block diagram of an MDI-QKD system

2.2.5 TF-QKD Protocol

The TF-QKD protocol was developed based on the MDI-QKD by M. Lucamarini, Z. L. Yuan, J. F. Dynes and A. J. Shields [41]. The communication distance is further improved compared to MDI-QKD because it measures single-photon interference instead of two-photon interference. A block diagram of a typical TF-QKD system is illustrated in Fig. 2.10.

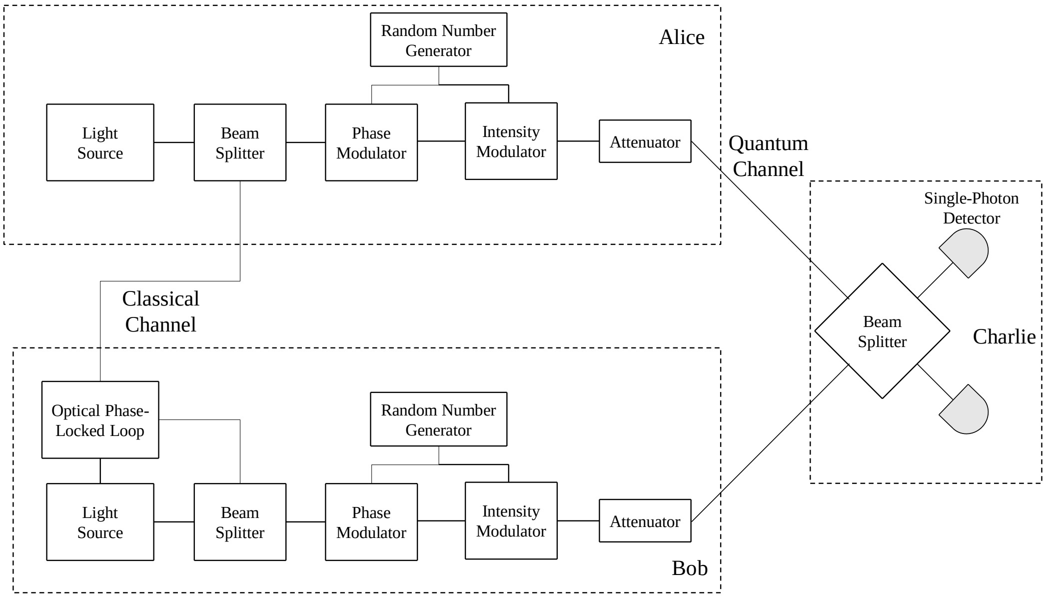

Figure 2.10 A typical block diagram of a TF-QKD system

Alice or Bob randomly chooses the bit value $\alpha_i=\{0,1\}$, the basis value $\beta_i=\left\{0,\frac{\pi}{2}\right\}$ and the global phase value $\gamma_i \in$ ¿, where i is *A* or *B*, representing Alice or Bob, respectively. The distribution of the global phase value is uniform between 0 and 2π. The coherent state $\left|\sqrt{\mu_i}e^{j\varphi_i}\right\rangle$ can be generated by intensity and phase modulation, where μ_i is the intensity and $\varphi_i=\alpha_i\pi+\beta_i+\gamma_i$. The intensity μ_i can have different values used to implement the decoy-state strategy. Then, the modulated quantum information from both Alice and Bob is sent to Charlie. Charlie measures the output of the beam splitter and publicly announces the measurement results. Alice and Bob also announce their intensity values μ_i, basis values β_i and global phase values γ_i. If the phase difference ($|\varphi_A-\varphi_B|$) announced by Charlie is less than a threshold Δ, these two phases are called “twins” and the corresponding qubits in Alice and Bob are kept. For example, Δ is set to be $\frac{\pi}{16}$. When the phase difference is $\frac{\pi}{20}$, the corresponding qubits are kept. If the phase difference is $\frac{\pi}{3}$, the corresponding qubits are discarded. When the phase difference is $\frac{21\pi}{20}$, the corresponding bits are kept. This is because $\left|\varphi_A-\varphi_B\right|-\pi<\Delta$. It means that $\beta_A=\beta_B$ and $\left|\gamma_A-\gamma_B\right|<\Delta$. In addition, if the phase difference is 0, the corresponding bit values can be directly seen as the raw key. When the phase difference is π, Bob should flip his bit values to obtain the raw key. Finally, error correction and privacy amplification are operated to get the final secure key.

2.3 WIRELESS QKD DEMONSTRATIONS

There have been a substantial number of QKD demonstrations focused on fibre-based QKD systems [42, 43, 80-87, 101, 105-118]. The maximum SKR achieved is more than 100 Mbit/s using BB84 at a distance of approximately 10 km [43] and the longest transmission distance is more than 1000 km based on TF-QKD [42]. However, there are very few demonstrations of short-range wireless QKD. These are summarized in Table 2.3 [46-50, 119-121]. The maximum SKR achieved so far reaches 0.322 Mbit/s working at 1550 nm.

Table 2.3 Summary of short-range wireless QKD demonstrations

Year	Authors	Protocol	Wavelength	Link length	SKR
2017	H. Chun et al. [46]	DV	658nm	0.5 m	30kbit/s

2021	D. Lowndes et al. [47]	DV	650nm	N/A	20kbit/s
2021	M. Avesani et al. [119]	DV	1550nm	145 m	30kbit/s
2022	A. T. Castillo et al. [48]	COW	850nm	1 m	6.4kbit/s
2023	X. Zheng et al. [49]	CV	1550nm	1 m	322kbit/s
2023	A. T. Castillo et al. [50]	COW	850nm	N/A	50kit/s
2024	F. Honz et al. [121]	BB84	1400nm	63m	<3.7kbit/s

A key factor causing limited wireless QKD demonstrations is ambient light interference. The ambient light within the optical bandwidth of the wireless QKD system is detected by the receiver, potentially dominating the detected signal. The strongest source of ambient light is sunlight. Fig. 2.11 shows the near-ground sunlight irradiance according to ASTM 1.5 Spectra [51]. There are several potential wavelengths for short-range wireless QKD. Wavelengths around 1370 nm and in the UV-C region of the optical spectrum (less than 280 nm) are of particular interest because of the extremely low sunlight irradiance. The irradiance at 1370 nm and 280 nm is $1\times10^{-11} W/(m^2\cdot nm)$ and $5\times10^{-23} W/(m^2\cdot nm)$ while over $0.8\,W/(m^2\cdot nm)$ for the visible light. A wireless QKD system around 1370 nm has been investigated [60], but the establishment of a wireless QKD system in the UV-C region is an issue to be explored.

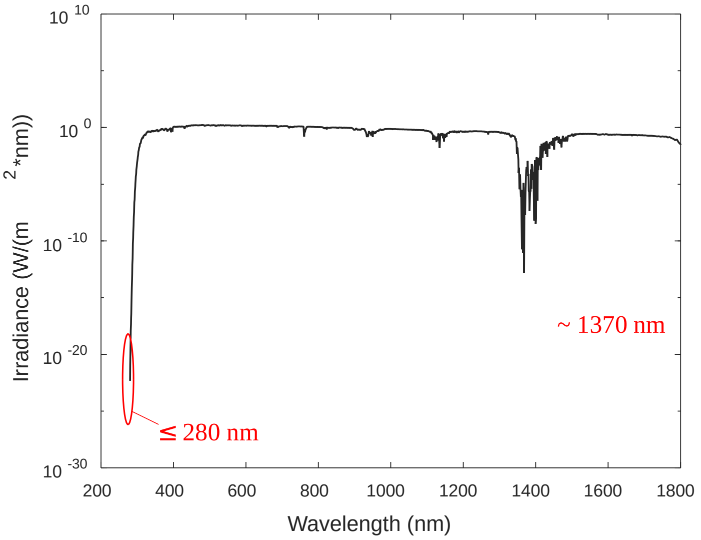

Figure 2.11 Near-ground sunlight irradiance

2.4 POTENTIAL OF UV-C SHORT-RANGE WIRELESS QKD

The lack of sunlight interference in the UV-C region provides the potential to develop a wireless QKD system, but the available light sources and photodetectors in the UV-C region are very limited. At the transmitter, the options for UV-C light sources are limited. There is no commercial laser diode (LD) operating below 300 nm. However, commercial UV-C LEDs are available with an operating wavelength even below 250 nm. The bandwidth of commercial LEDs is limited, however, typically these are around 10 MHz [122, 123]. One potential option is to use UV-C micro-LEDs, which have been fabricated with a peak wavelength of ≤ 280 nm and bandwidth exceeding 100 MHz [124, 125]. Therefore, UV-C micro-LEDs are a good candidate for a UV-C wireless QKD transmitter. At the receiver, there are very few UV-C SPDs reported [126-132]. Moreover, each of these reported UV-C SPD has obvious disadvantages, such as requiring an ultralow working temperature (4 K) or having a high DCR (≥ 500 kcps). One potential option is to use an SiPM, which is designed for photon counting. In the UV-C region, SiPMs typically have a usable photon detection efficiency (PDE) of ~15%, a DCR of ~$50\,kcps/mm^2$ and a gain of 1×10^6 [133]. Therefore, an SiPM is potentially a good choice for a UV-C wireless QKD receiver, but the DCR is too high at room temperature.

In addition, the B92 protocol is selected because of its resource-efficient characteristics. The final goal of the work reported in this thesis is to develop a short-range wireless B92 QKD system operating in the UV-C region, utilizing UV-C micro-LEDs and SiPMs.

2.5 CONCLUSIONS

This Chapter has reviewed different QKD protocols and state-of-the-art wireless QKD research. The typical structure of a QKD system was presented, including the physical layer, sifting, error correction and privacy amplification. A comparison of different QKD protocols was introduced, including DV-QKD, COW-QKD, CV-QKD, MDI-QKD and TF-QKD, followed by the summary of state-of-art wireless QKD demonstrations. Finally, the potential of building a UV-C short-range wireless QKD system was discussed.

A QKD system requires ultralow photon flux links with an average photon number per bit of less than 1. In the next Chapter, the development of a low photon flux link is discussed. This serves as the initial work leading to a QKD link.

Chapter 3:

Ultra-Sensitive UV Solar-Blind OWC with an SiPM

3.1 INTRODUCTION

OWC is a promising technology to provide high-quality wireless access service because of its high bandwidth, low latency, robustness to electromagnetic interference and lack of regulatory requirements [1, 3, 134]. A typical OWC system uses a light source to transmit and a photodetector to receive optical signals. Transmitters either use Light Emitting Diodes (LEDs) or Lasers. Receivers consist of a photodetector, amplification and subsequent decoding and decision-making.

There are typically three bands used for OWC: Infrared (IR) band (760 nm – 2000 nm), visible band (390 nm – 760 nm) and ultraviolet (UV) band (10 nm – 390 nm). According to the sunlight spectrum, to avoid sunlight interference, there is a “solar-blind” region within the UV band whose wavelength is from 200 nm to 280 nm [51]. Sunlight within this spectrum is absorbed by the ozone, resulting in an extremely low irradiance near the ground. Thus, this solar-blind spectrum is a potential solution for both indoor and outdoor OWC. Several devices for solar-blind communications have been developed [135-141] and links operating at the Gbit/s level have been demonstrated [142-144].

However, compared to visible and IR light, the safe irradiance level of UV light is much lower. According to eye safety standards, the irradiance of light between 200 – 400 nm should be no more than $1\,mW/m^2$ [145]. Recent UV solar-blind OWC link demonstrations use received power levels of microwatts, corresponding to ~10^4 photons per bit [146, 147]. For these demonstrations, the corresponding beam irradiance (considering the detected power divided by the receiver collection area) is estimated to be more than $10\,mW/m^2$, exceeding the safe irradiance level at the receiver. To the best of our knowledge, there was no demonstration showing a UV solar-blind OWC system, using a high-sensitivity receiver, that meets this eye safety criterion. Thus, to build OWC in the UV solar-blind region, improving receiver sensitivity to allow low transmission power is a key step.

Several materials are promising candidates for developing high-sensitivity detectors in the UV solar-blind band, including Molybdenum Silicide (MoSi), SiC, Gallium nitride (GaN) and Silicon (Si) [126-132]. A MoSi superconducting nanowire single-photon detector (SNSPD) reported in [128] has a PDE exceeding 70% and a DCR of approximately 0.25 count per second (cps) but is limited in its applicability due to the low operating temperature of 4K. In the case of SiC and GaN single-photon avalanche diodes (SPAD), the DCR is over $1\,Mcps/mm^2$ at room temperature with a PDE typically at around 10 % [129]. Among all Si-based photodetectors, the SiPM is specifically designed for photon counting [148-152]. Compared with the above three materials, typical SiPMs have a low DCR (~ $50\,kcps/mm^2$), can have a large active area (≥1 mm^2) and a high enough PDE (~15 %) for UV detection at room temperature [153]. Thus, an SiPM has the potential to form the basis of a high-sensitivity receiver working in this UV solar-blind region.

This Chapter presents a UV solar-blind OWC scheme based on such an ultra-sensitive receiver. First, a modelling of UV OWC links is reported. Then, a cooled UV-sensitive SiPM is described. This is combined with a commercial 275 nm LED used as a transmitter. Results from several different link demonstrations are then reported.

3.2 MODELLING OF UV WIRELESS COMMUNICATION LINKS

3.2.1 SiPM Operation

A key component providing high sensitivity in detecting ultralow received power signals is an SiPM. An SiPM is an array of Si-based single-photon avalanche diodes (SPADs), as shown in Fig. 3.1 [154]. Each SPAD operates in Geiger mode, due to the device design and the high bias voltage that reverse biases each diode.

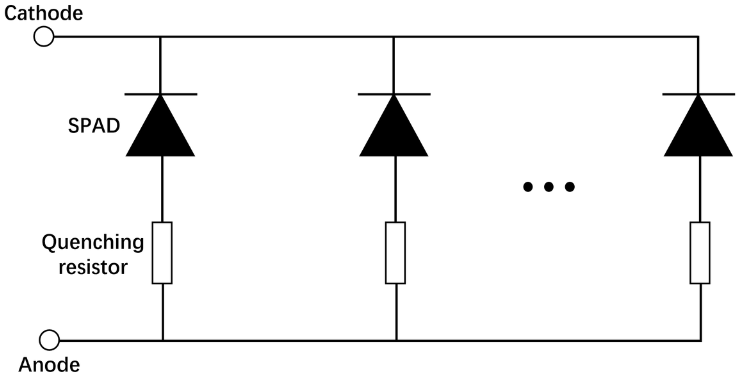

Figure 3.1 Structure of SPADs in an SiPM [154]

The SPADs in an SiPM are wired in parallel, and the photocurrent from SPADs are therefore summed together. For each SPAD, a detected photon causes avalanche multiplication and, in turn, generates a current pulse flowing through a quenching resistor. As the avalanche current increases, the quenching resistor develops a voltage drop, which effectively reduces the bias across the SPAD below its breakdown voltage. This causes the SPAD to exit the Geiger mode, thereby quenching the avalanche. As the avalanche current dissipates, the bias is gradually restored, and the SPAD becomes ready for the next photon detection. Dark Counts are spontaneously generated current pulses that occur without a detected photon and ultimately limit the sensitivity of the SiPM. When the number of detected photons and dark counts are low, the distribution of pulses follows a Poisson distribution [155].

3.2.2 System Model and Simulation

The UV wireless communication system model used in this section is a simple line-of-sight (LOS) model, including a transmitter, a receiver and an LOS wireless channel (see Fig. 3.2). The transmitter is assumed to be a commercial light source, such as a UV LED, transmitting OOK signals. The receiver is assumed to be a photon counting detector, such as an SiPM.

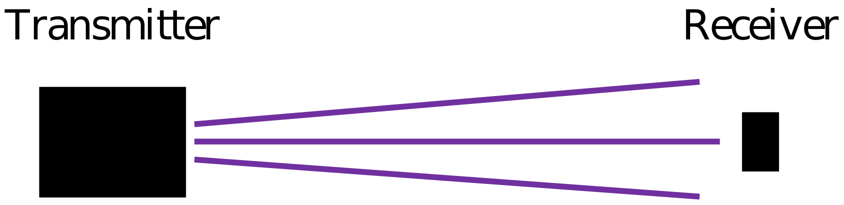

Figure 3.2 UV wireless communication model

The following theoretical analysis and simulation focus on the operation of the receiver and the estimation of the Bit Error Rate (BER) of the system. This is a function of the number of detected signal counts (caused by incident photons) and errors due to dark counts and the incorrect transmission of bits due to the Poisson statistics of the source. It is assumed that the transmitter sends photons as short pulses, and that the receiver has a detector that is sensitive over a detection window that is matched to the width of the transmitted pulse. This ensures that the receiver has a maximum received signal-to-noise ratio as it is not sensitive when there is no transmitted signal.

The probability of detecting dark counts is:

$$P_d = 1 - \frac{\left(DCR \cdot t_d\right)^0}{0!} e^{-DCR \cdot t_d} = 1 - e^{-DCR \cdot t_d} \qquad (3.1)$$

where t_d is the time duration of the detection window. The probability of transmitting a bit “1” when no photons are detected is:

$$P_n = \frac{\mu^0}{0!} e^{-\mu} = e^{-\mu} \qquad (3.2)$$

Where μ is the average number of detected photons per bit, which can be obtained from:

$$\mu = PDE \cdot P / \left(h \cdot c / \lambda\right) \qquad (3.3)$$

Where PDE and P are the photon detection efficiency and received power of the SiPM, respectively. Thus, the total BER is:

$$BER = \frac{1}{2} P_d + P_n - P_d \cdot P_n \qquad (3.4)$$

The factor $1/2$ originates from the 50% probability of dark counts occurring in bits “1”, which will not cause an error. $P_d \cdot P_n$ is the probability that bits “1” are correctly detected due to dark counts instead of detected photons.

Simulation was conducted to examine the effect of DCR and detection window on BER. The parameters and corresponding values are listed in Table 3.1. At the transmitter, 1 Mbit/s OOK signals are emitted with a wavelength of 280 nm. At the receiver, the received power is varied, changing from 10 pW to 30 pW. The detection window varies from 50 ns to 200 ns. The DCR changes from 30 kcps to 180 kcps, and the PDE is assumed to be 15% for 280 nm. These are typical values for an SiPM.

Table 3.1. Simulation parameters and values

Parameters	Values
Wavelength λ	280 nm
Data rate	1 Mbit/s
Received power	10 pW ~ 30 pW
DCR	30 kcps ~ 180 kcps
Detection window t_d	50 ns ~ 200 ns
PDE	15%

Fig. 3.3 shows a plot of BER versus the received power, with varying DCR and detection window size. The detection window and DCR are fixed at 50 ns and 50 kcps in Fig. 3.3 (a) and Fig. 3.3 (b) respectively. The figure shows a forward error correction (FEC) threshold of 3.8×10^{-3}, at which bit error-free can be achieved with a 7% coding overhead [125]. The results show the BER decreases with the rise of received power. This is because the probability of transmitting a bit “1” when no photons are detected is reduced according to Eq. (3.2). When the received power is over 25 pW, there is little change in BER. This is because the probability of transmitted bits “1” without detected photons is very small, and the

unchangeable error of transmitted bits “0” detected as “1” due to DCR dominates the total BER, according to Eq. (3.1). Moreover, the product of DCR and detection window should not exceed $7500\,kcps \cdot ns$, or the BER will be over the FEC threshold.

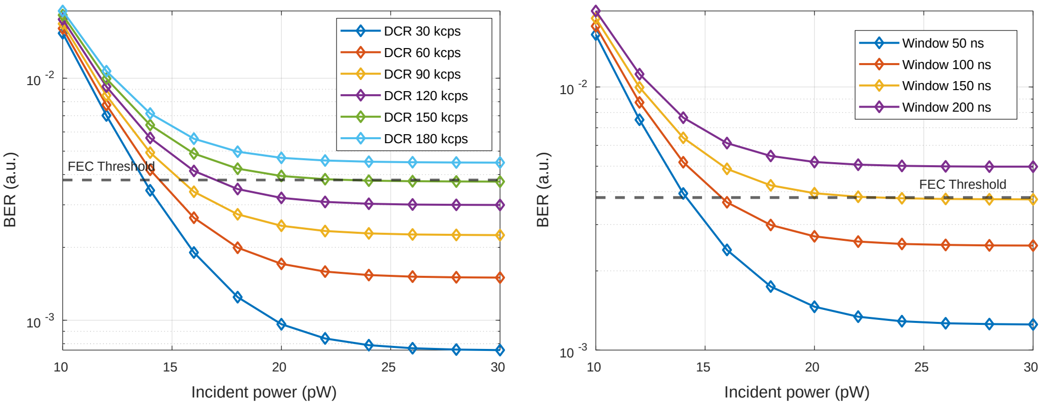

(a) (b)

Figure 3.3 BER versus received power, DCR and detection window (a) with a detection window of 50 ns (b) with a DCR of 50 kcps

Therefore, with a receiver having a DCR of less than 50 kcps and a detection window of lower than 100 ns, modelling indicates that a practical UV wireless communication system can be established.

The following sections describe the design of the transmitter and receiver for a link that will meet these requirements.

3.3 TRANSMITTER CHARACTERIZATION

To build a UV solar-blind OWC link, a transmitter should have a central wavelength <280 nm, with as large a modulation bandwidth as possible. Because of the lack of commercial LDs operating below 300 nm, a UV LED is the only option for the light source.

The Thorlabs LED275J was selected because the LEDs from different manufacturers are roughly the same. According to the datasheet, the central wavelength is 275 nm and the FWHM is 12 nm. The LED is packaged with an integrated ball lens to control emission from the device and the field-of-view (FOV) is 15°. Additionally, the maximum output optical power is approximately 1 mW with a drive current of 100 mA.

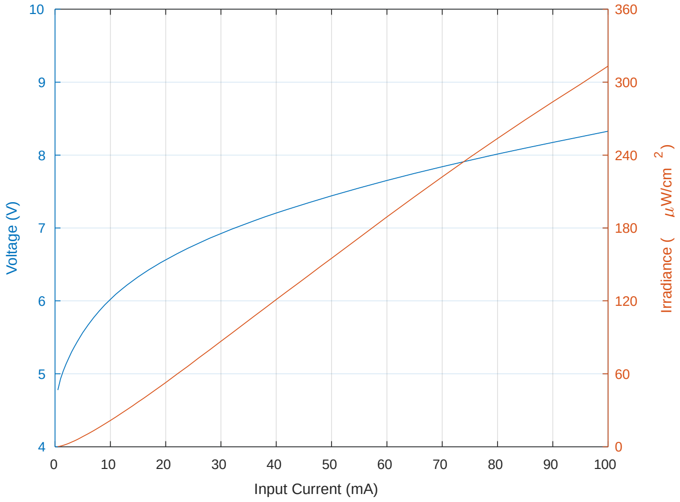

Figure 3.4 Plot of I-V and I-I for Thorlabs LED275J LED

In addition to the above characteristics the current-voltage-irradiance (I-V-I) curves and bandwidth need to be determined. An experiment to measure the I-V-I curves was undertaken. A source meter (KEITHLEY 2636B) was used to drive the LED and measure the voltage across it. The optical power emitted by the LED was measured by a power meter (Newport 843-R) with a UV-enhanced silicon (Si) head (818-UV/DB). The corresponding irradiance was calculated by dividing the measured power by the detection area of the Si head. The LED's output power was not measured due to its relatively large divergence angle and the limited detection area of the Si head. Even when the LED and Si head are placed nearby, the Si head is unable to collect all the emitted power from the LED. Thus, the LED and the Si head were aligned with a separation of approximately 10 cm, in order to match the transmitter-to-receiver distance used in the OOK link experiment in this Chapter (see section 3.5). The measured I-V-I curves are illustrated in Fig. 3.4. The result shows the turn-on voltage is approximately 5 V.

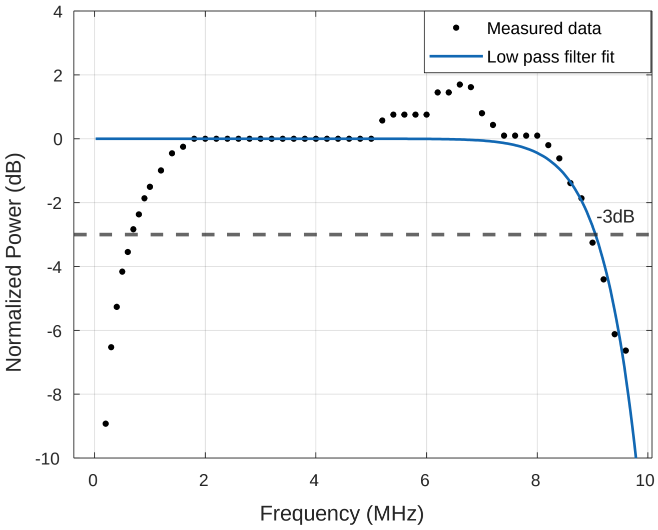

Figure 3.5 Normalized signal power versus frequency

The bandwidth was then measured. DC bias provided by a laser driver (Thorlabs LDC205C) and an AC signal (sine wave) provided by an arbitrary waveform generator (AWG, AGILENT 81150A) were combined by a Bias Tee (Mini-Circuits ZFBT-6GW). The combined signal was used to drive the LED. Two convex lenses (LA4647-UV and LA4130-UV) were used to collimate the light from LED275J and focus light onto the active area of a SiC APD (GaNo Optoelectronics SPAD-ABC-S) detector. According to the SiC APD's datasheet, the rise time is ns-level, so the corresponding bandwidth is at least over 35 MHz (Bandwidth$\approx 0.35/rise\,time$). Moreover, the PDE at 275 nm, the diameter of the active area and the gain are 10%, 120 μm and 100, respectively. The APD was used in combination with a trans-impedance amplifier (TIA) MAX3665 with a gain of 8kΩ and a bandwidth of over 100 MHz. A small Printed Circuit Board (PCB) was used to ensure a good connection between the TIA and APD. The amplified signal was then recorded on an oscilloscope (AGILENT MSO6104A).

The AWG frequency was varied between 100 kHz and 10 MHz, and the signal level on the Oscilloscope was recorded. This signal level is proportional to the optical power received by the APD. Fig. 3.5 shows the frequency response of the link, showing an electrical-to-optical (E-O) bandwidth of approximately 9 MHz. Although it is not possible to accurately determine the bandwidth of the receiver the estimated bandwidth is much greater than 9MHz, indicating that this is the bandwidth of the LED device. The other notable feature in the figure is the lower frequency cut-off which is due to the response of the Bias Tee.

3.4 RECEIVER DESIGN AND CHARACTERIZATION

To build a UV solar-blind OWC link, an SiPM-based receiver should meet the following criteria: (1) enough PDE (2) high gain (3) wide bandwidth and (4) low DCR. Because of the lack of a suitable commercial detector module, a new receiver needs to be developed. The next section describes the choice of detector.

3.4.1 SiPM Selection

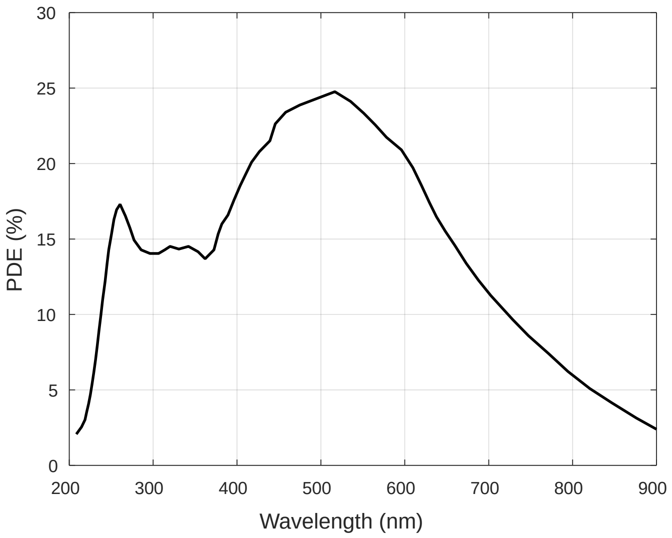

Figure 3.6 PDE of HAMAMATSU S13360-3025UQ-SPL

SiPMs with a range of different characteristics are available. A typical SiPM (HAMAMATSU S13360-3025UQ-SPL) is a feasible option. This SiPM has a 3x3 mm^2 active area and is designed for UV photon counting, with a window material of quartz glass, allowing UV light to pass through. The corresponding PDE curve is shown in Fig. 3.6. It shows the PDE at 280 nm is approximately 15 %.

The gain is significant for pulse detection because every pulse generated by a detected photon should be at least at the mV level to be observed by an oscilloscope. The gain of the S13360-3025UQ-SPL is 7×10^5, which is significantly higher than the gains of 10 -100 for linear mode APDs. The rise time of the S13360-3025UQ-SPL is ns-level, corresponding to a bandwidth of at least tens of MHz. The fall time is on the order of tens of ns and is limited by the quenching time. This quenching time can be approximated by the RC time constant, $T_f = R_{quench} \cdot C_{SPAD}$, where R_{quench} is the quenching resistor and C_{SPAD} is the capacitance of the SPAD.

However, the DCR of S13360-3025UQ-SPL is over 400 kcps, which is higher than the required value of 50 kcps according to the simulation in section 3.2. Thus, a method of cooling the detector is necessary to reduce the temperature to achieve a small enough DCR [153].

3.4.2 Cooling Design

A passive cooling design for the S13360-3025UQ-SPL using a Peltier cooler (Laird SH10-23-06-L1-W4.5) was developed and is shown in Fig 3.7.

The Peltier cooler has a centre hole and is sandwiched between a cold plate and a hot plate, both made of Al. A thermistor is connected to the cold plate to measure its temperature, representing the temperature of the SiPM. The SiPM was placed on the top of the cold plate, with its leads going through the Peltier cooler to connect to an evaluation board (HAMAMATSU C12332-02). The evaluation board was remotely controlled to provide the bias voltage to the SiPM. The dark current of the SiPM was measured by connecting the output of the evaluation board to a source meter (KEITHLEY 2636B).

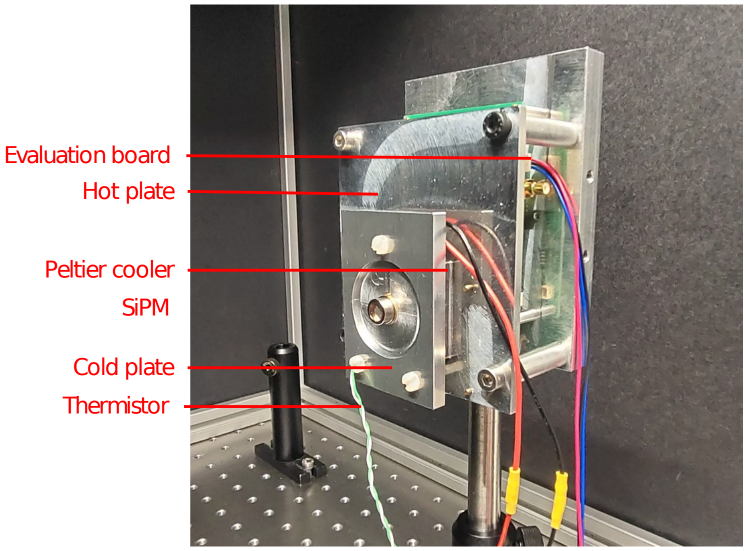

Figure 3.7 Passive cooling design for S13360-3025UQ-SPL

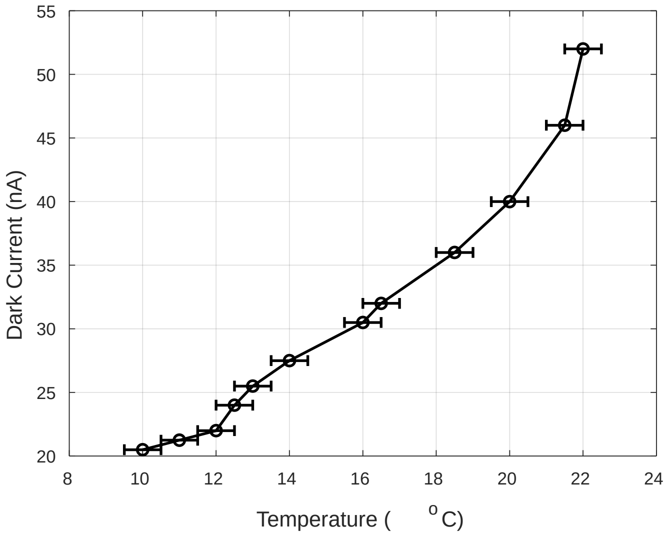

Figure 3.8 Dark current versus temperature for S13360-3025UQ-SPL

The bias voltage was fixed at 56.86 V, which is the recommended value for the SiPM. The measured dark current versus temperature is shown in Fig. 3.9. (An error bar of 1 ℃ is added because the temperature values were measured as integers.) The results show the dark current decreases from 52 nA to 20 nA with the temperature reduced from 22 ℃ to 10 ℃. A current of 20 nA corresponds to approximately 180 kcps, which is still too high to establish a UV solar-blind OWC link. The temperature cannot be further reduced, as the cooling capacity is limited by the heat dissipation capacity of the hot plate. However, cooling has proved to be effective in reducing DCR. A new cooling design is needed to further reduce the temperature of the SiPM.

An alternative method to improve heat dissipation is using active liquid cooling instead of passive cooling. This is because the heat transfer coefficient of flowing liquid ($¿500\,W/\left(m^2\cdot K\right)$) is much higher than that of still air ¿$10\,W/\left(m^2\cdot K\right)$. Thus, liquid cooling has the potential to efficiently dissipate the heat of the hot plate, which in turn allows the Peltier cooler to cool the SiPM to a low enough temperature.

The goal of the liquid cooling design is to achieve an SiPM temperature of -10 ℃, ensuring a DCR of below 50 kcps (see section 3.2.2). This is determined by an over 400 kcps of S13360-3025UQ-SPL at room temperature and a 10 dB reduction in DCR per 30 ℃ decrease [153]. There are two key considerations for the cooling design: (1) high-efficiency heat dissipation on the hot side and (2) overcoming the condensation on the SiPM’s surface as the temperature of the SiPM falls below the dew point, which is typically around 10 ℃. A liquid CPU cooler (MASTER LIQUID LITE 240) was used to cool the hot plate. An image of the liquid cooling design is shown in Fig. 3.9 (a), and Fig. 9 (b) illustrates the sectional view.

The Peltier cooler (Laird SH10-23-06-L1-W4.5) is at the centre. At its cold side, there is a small Al plate (cold plate) held in place by an auxiliary plastic plate, thus reducing the overall thermal load that must be cooled. The SiPM is positioned on top of the cold plate and is held in place by an SM1 to TO-5 adaptor (Thorlabs S1LM05). To avoid condensation, the SM1 tube is glued on an auxiliary plastic plate with a UV filter (Thorlabs FGUV5M) on top to make a confined environment, and the air around the SiPM is pumped away by a vacuum pump (RS vacuum pump). The hot side of the Peltier and the CPU cooler are thermally connected through a large Al plate (hot plate). Graphene sheets are placed on the surface of adjacent components (SiPM, cold plate, Peltier cooler, hot plate and CPU cooler) to ensure efficient heat conduction. To connect the SiPM to the PCB board, there is a hole in the middle of the cold plate, Peltier cooler and hot plate and a horizontal trench in the hot plate for the wires to pass through.

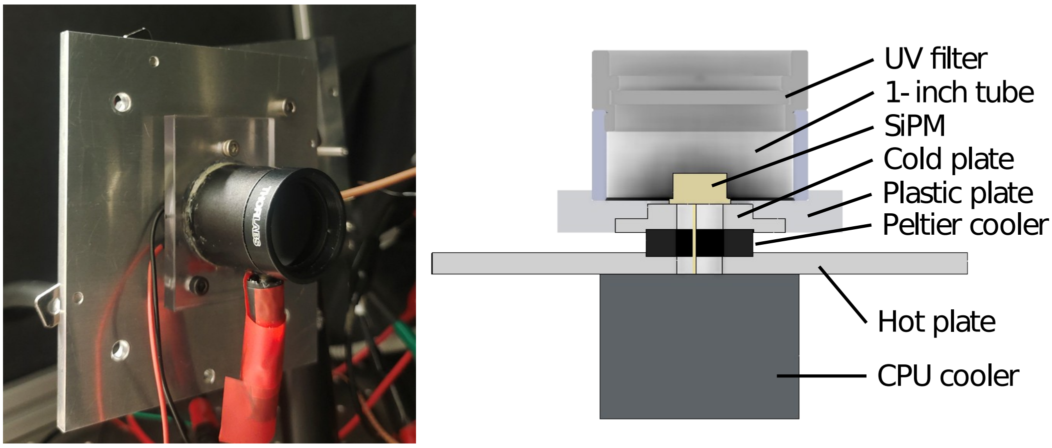

(a) (b)

Figure 3.9 Liquid cooling design (a) Image (b) Sectional view

3.4.3 Amplification Circuit Design

An amplification circuit using a TIA (ADA4817) was designed by James Farmer, a postdoctoral researcher in our group. The ADA4817 has a gain bandwidth product (GBWP) of 410 MHz. The theoretical 3-dB bandwidth of this amplification circuit can be calculated as [156]:

$$f_{3dB} \approx \sqrt{\frac{GBWP}{2\pi R_F C_{\text{¿}}}} \quad (3.5)$$

where R_F is the resistance of the trans-impedance load and $C_{\text{¿}}$ is the total capacitance at the input of the TIA. The resistance of the trans-impedance load is 7500 Ω, and the total capacitance is dominated by the SiPM capacitance of approximately 320 pF. Thus, the theoretical 3-dB bandwidth of the receiver is calculated as 5.2 MHz.

3.4.4 Receiver Characterization

The cooling performance of the receiver was characterized by measuring the dark current as a function of temperature and bias voltage. A source meter (KEITHLEY 2636B) provided the bias voltage to the SiPM and measured the SiPM’s output current as the dark current. The temperature of the SiPM is represented by the temperature of the cold plate, which was measured by a thermistor (TDK B57703M). The measured result is shown in Fig. 3.10. The SiPM was cooled from 21 °C to -10 °C. Further reducing the temperature is difficult because of the limitations of the Peltier cooler and CPU cooler.

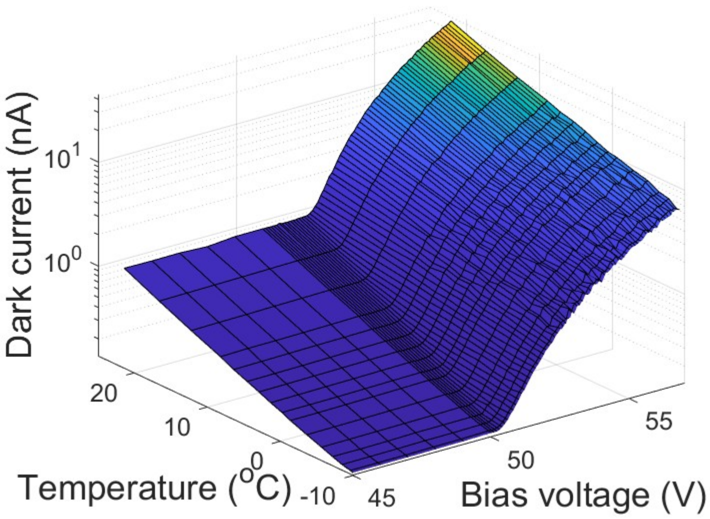

Figure 3.10 Dark current versus temperature and bias voltage

The breakdown voltage of the detector decreases with decreasing temperatures by 54 mV/K. In order to keep a constant overvoltage, the bias voltage (breakdown voltage + overvoltage) must be adjusted according to the temperature setting. Thus, at -10 ℃ the bias voltage was set to 55.2 V resulting in a measured dark current of 3.9 nA compared to 56.8 V and 42 nA at 21°C. The corresponding DCRs are 35 kcps and 375 kcps, respectively. These measurement values correspond to a reduction in the dark current of about 10 dB with 30 K of cooling. This gradient agrees with previously reported values for SiPMs [153]. The temperature cannot be further reduced because of the limitation of the Peltier cooler and CPU cooler.

The gain of the SiPM can be obtained by:

$$G=\frac{I_d}{DCR\cdot e_0} \quad (3.8)$$

where I_d is the dark current and e_0 is the elementary charge. Thus, the gain of the SiPM is approximately 7×10^5.

The current from the SiPM versus irradiance from the LED275J was measured to obtain the PDE. The LED275J was driven by a laser driver (Thorlabs LDC205C), and the irradiance was measured by a power meter (Newport 843-R with a UV-enhanced Si head 818 UV/DB). Then, the receiver replaced the power meter at the same position to obtain the photocurrent from the SiPM. The bias voltage was adjusted to recommended values with temperature change. The measured result is shown in Fig. 3.11, considering both 21 ℃ and -10 ℃. The difference between the two curves at the beginning reflects different dark currents at these two temperatures.

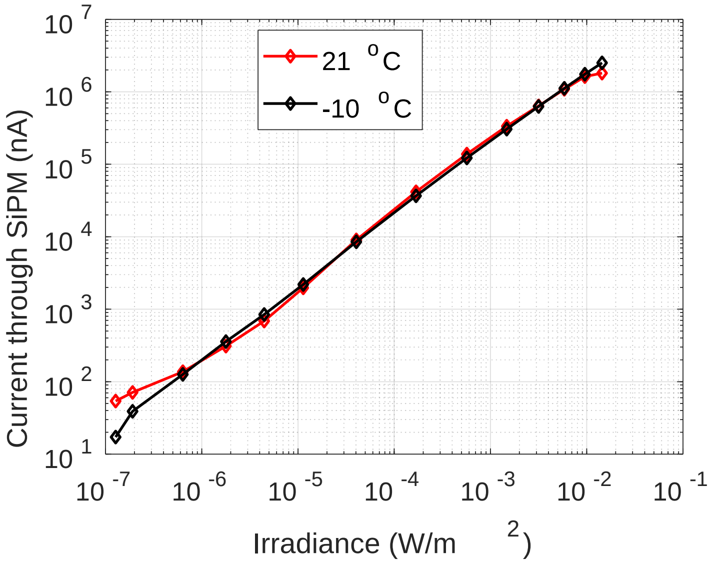

Figure 3.11 Current from the SiPM versus irradiance from LED275J

As the plots for both temperatures are similar to each other, the gain and the PDE of the SiPM can be considered constant. The PDE can be obtained by:

$$PDE = \frac{(I_t - I_d) \cdot h \cdot c}{G \cdot e_0 \cdot E \cdot A \cdot \lambda} \quad (3.9)$$

where I_t is the total current from the SiPM, including photocurrent and dark current. E is the irradiance and A is the detection area of SiPM. h is Planck's constant and c is the speed of light. λ is the operating wavelength. Thus, the PDE is calculated as 15.38 %.

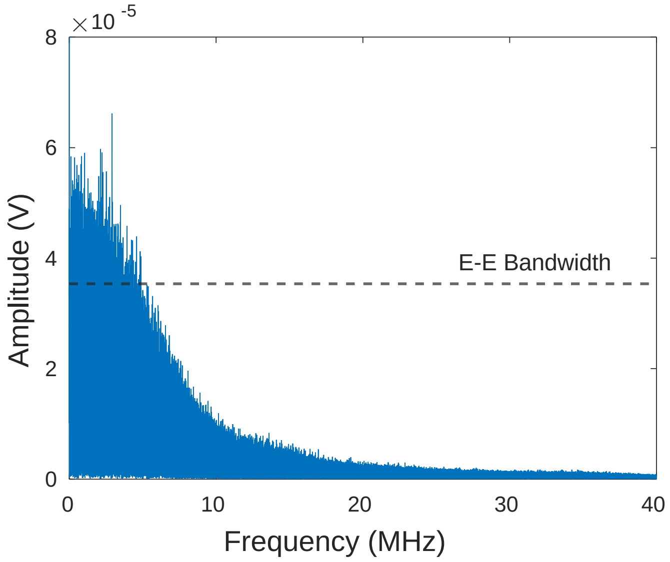

Figure 3.12 The frequency domain of dark pulses

The bandwidth of this receiver can be estimated by Fourier transforming the output signal from the receiver due to dark counts. An individual dark count gives rise to a very short output pulse whose shape corresponds to the impulse response of the system so that the Fourier transform can be used to estimate bandwidth. The Fourier transform of a sequence of dark pulses recorded over 20 ms is shown in Fig. 3.12. The result shows the amplitude of around 0 MHz is approximately 55 μV. The receiver's electrical-to-electrical (E-E) bandwidth is estimated to be approximately 5 MHz, corresponding to an amplitude of $55\,\mu V/\sqrt{2} \approx 39\,\mu V$. The measured E-E bandwidth matches the theoretical bandwidth calculated in section 3.4.3, with the limitation caused by the amplifier.

3.5 ULTRA-SENSITIVE UV SOLAR-BLIND OWC LINKS

A UV solar-blind OWC link was established to test the sensitivity of the receiver. The block diagram of the corresponding experimental setup is shown in Fig. 3.13. Initially, an On-Off-Key (OOK) link was tested.

A pseudorandom binary sequence (PRBS) OOK sequence with a length of 2^{10} = 1024 bits was generated by a PC. This sequence length exceeds that of the standard PRBS9 (511 bits), making it suitable for high-speed communication link testing. The generated sequence was then loaded into an arbitrary waveform generator (AWG, AGILENT 81150A) with a memory depth of 512k samples, which was used to drive LED275J. Light from the LED propagates to the receiver, which was placed 10 cm from the transmitter. A source meter (KEITHLEY 2636B) provided the bias voltage to the receiver. The OOK signal detected by the receiver was sent to an oscilloscope (AGILENT MSO6104A). The data captured by the oscilloscope was post-processed offline. In addition, the AWG, source meter and oscilloscope were remotely controlled by a PC.

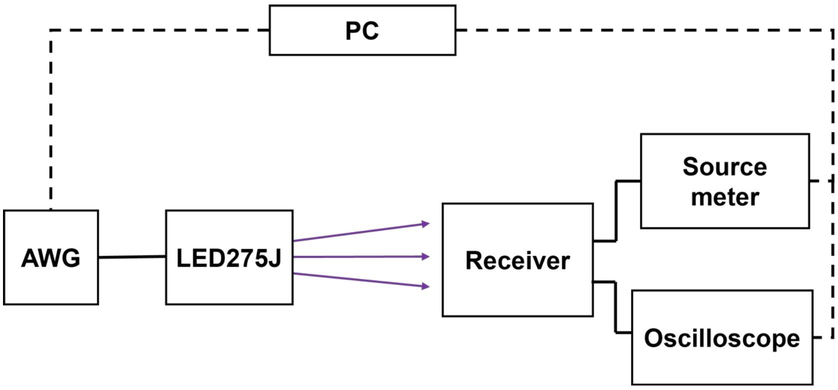

Figure 3.13 Block diagram of links' experimental setup

The link was characterized by transmitting a range of sequences at different data rates and different received power. Firstly, the received power was varied from 10 pW to 40 pW with a fixed data rate of 1 Mbit/s to measure the receiver's sensitivity. The duty cycle was set as 5%. Both 21 ℃ and -10 ℃ conditions were considered and the corresponding bias voltages were 56.8 V and 55.2 V, respectively. The overvoltage was constant, so the PDE and gain were fixed at 15.38 % and 7×10^5, respectively. The detection window was set as 50 ns to match the duty cycle of 5%. The values of the detection window and the duty cycles are a compromise choice because they are a trade-off between BER and the transmitter's bandwidth. The data of the received signal was synchronized with the transmitted PRBS sequences by correlation in the time domain.

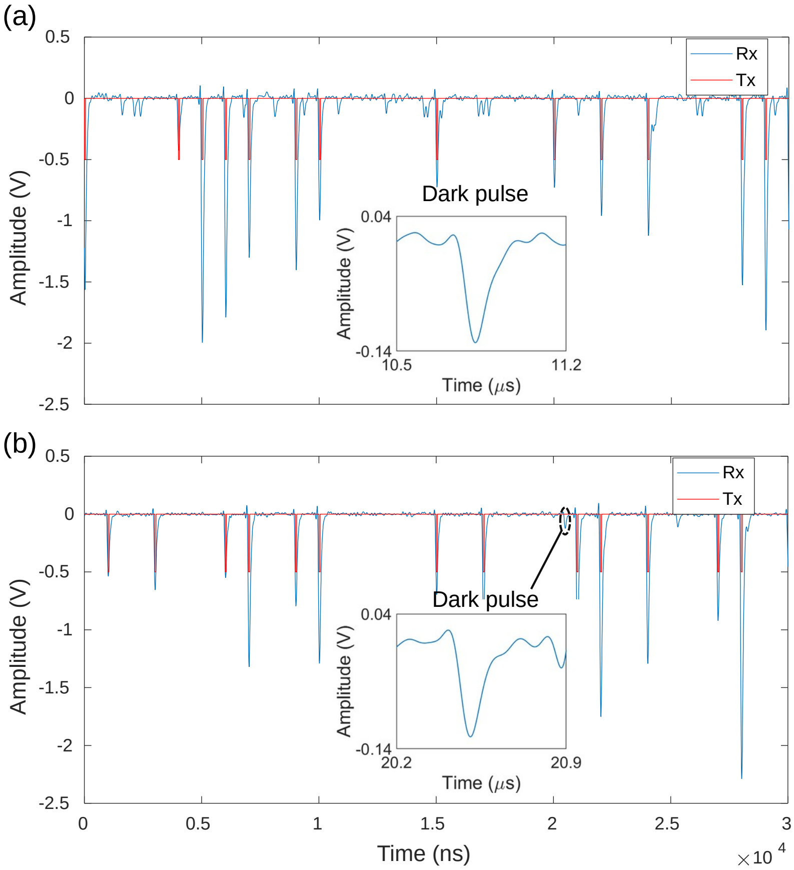

Figure 3.14 Synchronized transmitted sequences and received signal at (a) 21 ℃ (b) -10 ℃

Fig. 3.14 shows the synchronized transmitted sequences and received signal during 30 μs at both 21 ℃ and -10 ℃. In the figure, the data rate shown is 1 Mbit/s, and the received power is 30 pW (corresponding to 41.5 photons per bit). In the transmitted sequence (red line), the value -0.5 V represents the transmitted bit “1”. In the received pulses (blue line), the amplitude of each “1” bit has different amplitudes. This is because the number of detected photons in each bit is different, following a Poisson distribution. The zoomed single dark pulses in Fig. 3.14 (a) and (b) are nearly identical, including the shape and amplitude, because of the unchanged overvoltage. Moreover, the number of dark pulses is significantly reduced from 21 ℃ to -10 ℃.

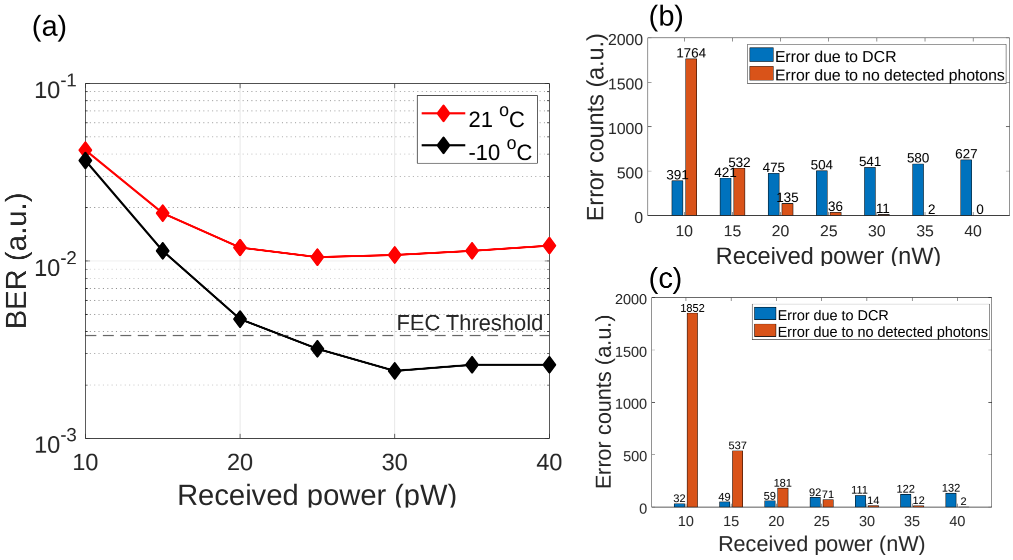

Figure 3.15 (a) BER versus received power and temperature (b) Error counts versus received power measured at 21 ℃ (c) Error counts versus received power measured at -10 ℃

The bit decision (whether “1” or “0”) depends on whether there is any detected photon within the bit. This is achieved by comparing the values of the received signal within the detection window to a decision threshold. The decision threshold was set as -125 mV, corresponding to approximately 90 % of a single pulse’s peak value to ensure the counts from pulses with irregular shapes, without losing generality. It is noted that the values of the received signal are negative, due to the inverting operation of TIA. Thus, the bit is determined to be “1” if the minimum value within the detection window is below the decision threshold. The BER versus received power and temperature are plotted in Fig. 3.15 (a) for the data rate of 1 Mbit/s.

Each BER point is obtained by transmitting 50×2^{10} bits. The results show that the BER at -10 ℃ is always lower than the BER at 21 ℃ due to the reduction of DCR. The two BER curves each drop to a minimum value (2.4×10^{-3} with 30 pW at -10 ℃) because the error due to transmitted “1” detected as “0” decreases (referred to as the error due to no detected photons in the figure). This error occurs when there are no detected photons in a bit that should be “1”, due to the Poisson distribution of photon numbers. The two BERs slightly increase when the received power exceeds 30 pW, due to the increase of afterpulses. Afterpulses are delayed pulses following pulses due to detected photons and dark counts, and are generated with a specific probability when a threshold current from SiPMs is exceeded [157]. Assuming the optimal power corresponds to a BER equal to the FEC threshold, the optimal received power is 23 pW. This corresponds to 32 photons per bit, approaching the quantum limit [158].

These experimental results in Fig. 3.15 (a) are worse than the simulation shown in Fig. 3.3. When the BER is equal to the FEC threshold, the received power in Fig. 3.3 is ~14 pW while 23 pW in Fig. 3.15 (a). In order to investigate the reason for the difference between the simulation and experiment, the numbers of errors due to DCR and the error due to no detected photons versus received power are plotted in Fig. 3.15 (b) and (c). The reduction of error due to no detected photons with increasing received power is because of the increased number of average detected photons per bit. The error of DCR slightly increases with received power due to afterpulses. Due to the bandwidth limitation of the detector, the time-broadened afterpulse falls into the detection window of the next bit. Thus, inter-symbol interference (ISI) occurs and a transmitted “0” can be detected as “1” due to the afterpulse from a previously transmitted bit. Higher received power increases the proportion of photon pulses exceeding the afterpulses threshold current and in turn, increases the number of afterpulses, resulting in higher BER.

Table 3.2 Duty cycle for different data rates

Data rate (Mbit/s)	0.1	0.2	0.5	1	2
Duty cycle (%)	0.5	1	2.5	5	10

Then, the bit rate was varied from 100 kbit/s to 2 Mbit/s with a fixed received power per bit (41.5 photons per bit). The corresponding duty cycles were varied to match the detection window of 50 ns, which are listed in Table 3.2. The BER versus data rate is shown in Fig. 3.16 (a). Each BER point is obtained by transmitting 50×2^{10} bits. The result shows a maximum data rate of 1 Mbit/s with a BER of 2.4×10^{-3}. The corresponding numbers of two categories of errors are shown in Fig. 3.16 (b). It can be seen that the error due to DCR is the dominant error and increases with data rate resulting in the BER at 2 Mbit/s exceeding the FEC threshold. This is because increasing the data rate will increase the probability of detecting afterpulses and ISI is more severe at higher data rates because the response of the receiver is longer than the bit duration [159].

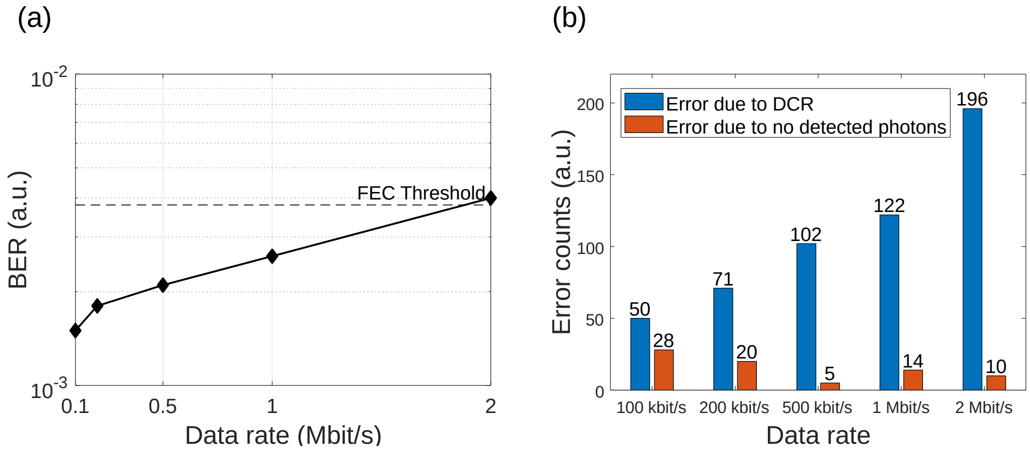

Figure 3.16 (a) BER versus data rate (b) Error counts versus data rate

3.6 CONCLUSIONS

This Chapter details work on building ultra-sensitive UV solar blind OWC links, including light source characterization, receiver design and a link demonstration. Overall, a 1 Mbit/s OOK UV-C OWC communication link was demonstrated with a measured BER of 2.4×10^{-3} and an average received photon number per bit of 41.5. This shows the potential for building ultralow photon flux links for a UV-C QKD system.

However, the receiver's sensitivity shown in this Chapter is not high enough to reach single-photon link level performance. The receiver design needs to be improved to further reduce the SiPM temperature for a lower DCR. The next Chapter will show an upgraded receiver design and ultralow photon flux links that are feasible for the final UV-C wireless QKD.

Chapter 4:

Ultralow Photon Flux Links Using UV-C Single-Photon Detection

4.1 INTRODUCTION

Ultralow photon flux links have applications in such areas as deep-space communication and QKD [23, 160-162]. Building on the foundation established in Chapter 3, this Chapter will further reduce DCR to enhance SiPM-based receiver sensitivity to a single-photon sensitivity level.

In addition to the SPD, a high-speed transmitter is another significant element for building high data rate UV-C ultralow photon flux links. Due to the lack of a commercial UV-C LD and the low speed of commercial UV-C LEDs (with a typical bandwidth of ≤10 MHz), micro-LEDs become an attractive option. Micro-LEDs have been used to implement high-speed data links [124, 125, 163, 164], and are available in the UV-C wavelength band of interest. In this region AlGaN micro-LEDs with a diameter of around 100 µm have been reported [125, 163]. They exhibit a peak wavelength of ≤280 nm, an output power of ≤ 1 mW, and a bandwidth exceeding 100 MHz [124, 125]. Over 1 Gbit/s OWC links using UV-C micro-LEDs have been reported and the maximum transmission distance has reached 100 m [146, 165, 166].

In this Chapter, a UV-C micro-LED with a bandwidth of over 400 MHz and an enhanced SiPM-based UV-C SPD are introduced. Then, ultralow photon flux links, including pulse position modulation (PPM) links and single-photon links are described.

4.2 UV-C MICRO-LED CHARACTERIZATION

As reported in Chapter 3, 1 Mbit/s is the maximum data rate that can be achieved for an OOK link [52], because of the low modulation bandwidth of the commercial UV-C LED (Thorlabs LED275J) used and the high DCR of the SiPM (HAMAMATSU S13360-3025UQ-SPL). In order to achieve a higher data rate link, a new high-bandwidth UV light source is a key goal. This section will introduce a high-bandwidth UV-C micro-LED.

UV-C micro-LEDs have been widely reported [124, 125, 163, 164]. There are several potential materials for manufacturing these devices, including AlGaN [125, 163], ZnO [167], Ga2O3 [168] and perovskite [169]. AlGaN-based UV-C LEDs have demonstrated the best performance. The emission wavelengths for these devices range from 200 nm to 400 nm, due to the bandgaps of GaN and AlN of 3.4 eV and 6.2 eV respectively. By tuning the Al content within the AlGaN-based alloy material, the emission wavelength can be continuously adjusted within the UV range of wavelengths.

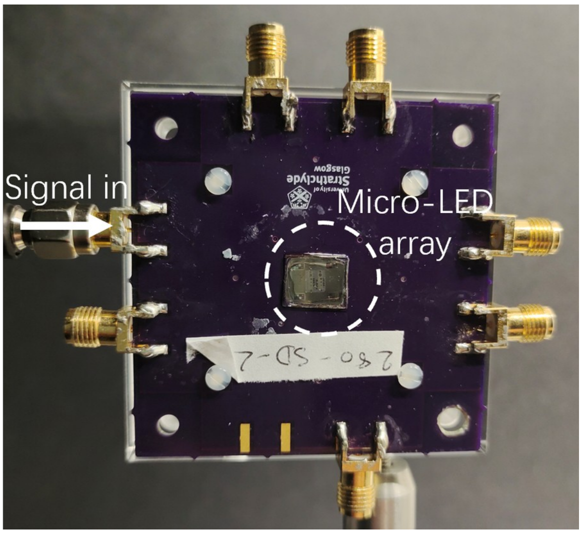

Figure 4.1. UV-C micro-LED array image

The AlGaN-based micro-LED used in this Chapter is a micro-LED array comprising three different diameters of micro-LEDs (100 µm, 200 µm and 300 µm). These micro-LEDs are manufactured at the Institute of Photonics, Department of Physics, SUPA, University of Strathclyde [125]. An image of the device is shown in Fig. 4.1. The three micro-LEDs are bonded at the central region of the PCB, with each micro-LED being connected to an externally mounted SMA port.

The 100 µm micro-LED (the smallest available) is selected to pursue the highest data rate because the micro-LED’s modulation bandwidth increases with decreasing diameter [163]. Note that all micro-LEDs mentioned in the rest of this Chapter refer to the 100 µm micro-LED.

An initial experiment to characterize these devices was undertaken. The micro-LED was driven by a source meter (KEITHLEY 2636B), and the irradiance was measured by a power meter (Newport 843-R with a UV-enhanced Si head 818 UV/DB) to obtain the I-V-I curves. The divergence angle of the micro-LED is over 120°, so the irradiance was measured instead of power (because the emitted power of the micro-LED is unable to be fully collected by the Si head even when they are placed nearby) [163]. The distance between the micro-LED and Si head is 6.5 cm. Fig. 4.2 (a) presents the I-V-I curves of the device. The result shows the turn-on voltage of the micro-LED is approximately 5 V.

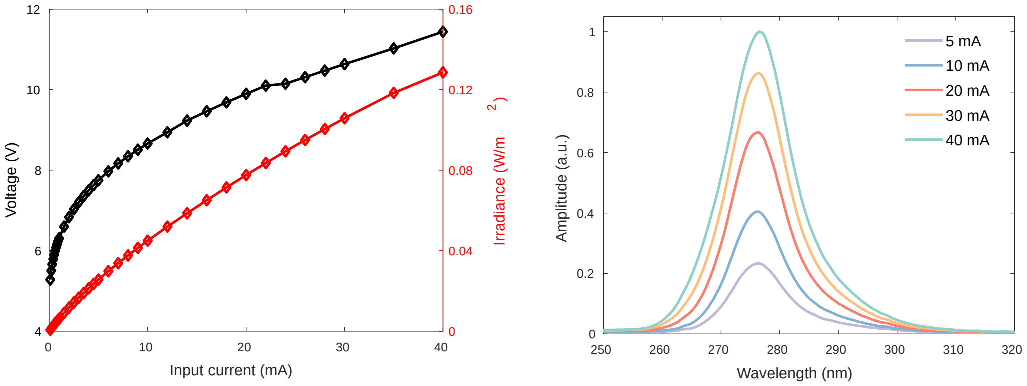

(a) (b)

Figure 4.2 (a) Plot of I-V and I-I for the micro-LED (b) Emission spectrum for a range of driving current from 5 mA to 40 mA

The emission spectrum of the micro-LED was measured by using an optical spectrum analyzer (Ocean Insight OFX00951). Fig. 4.2 (b) shows the spectrum versus wavelength with driving current varying from 5 mA to 40 mA. The spectrum covers both parts of the UV-B and UV-C regions and the FWHM is approximately 11 nm. The emitted peak wavelength is 276 nm.

The bandwidth of the micro-LED was then measured. Signals were generated by a vector network analyzer (VNA, Agilent Technologies FieldFox N9923A) and DC bias was provided by a power supply (ROHDE & SCHWARZ HMP4040). These were combined by a Bias Tee (Mini-Circuits ZFBT-6GW) and then used to drive the micro-LED. Two convex lenses (Thorlabs LA4052-UV) collimated light from the micro-LED and focused it on the active area of a 1 GHz bandwidth optical receiver (HAMAMATSU C5658 APD module). The output from the receiver was then connected to the VNA.

The 3-dB bandwidth was obtained by sweeping the S21 value versus frequency. Fig. 4.3 (a) shows the normalized response of the VNA’s S21 value with the micro-LED bias current ranging from 5 mA to 25 mA. The electrical-to-electrical (E-E) is defined as the frequency at which there is a 3dB attenuation of electrical power relative to a reference, and the (E-O) bandwidth is defined as the frequency at which the optical power drops by 3dB relative to a reference. As the VNA measures the E-E response the 3dB E-O bandwidth corresponds to a 6dB drop in E-E response.

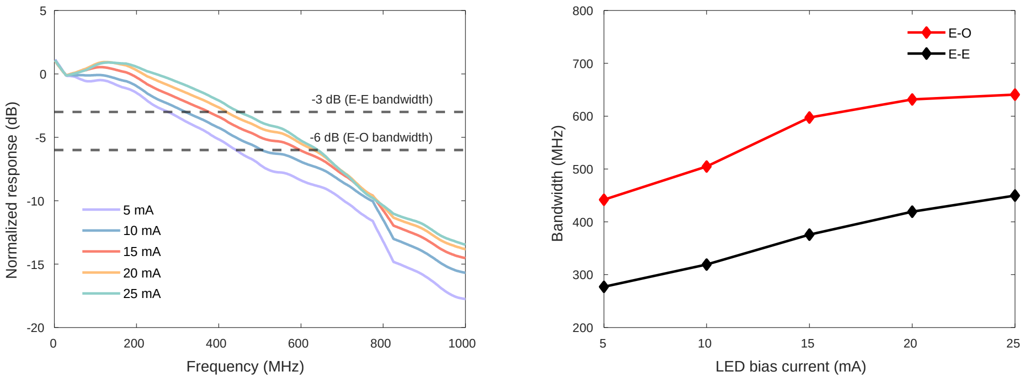

(a) (b)

Figure 4.3 (a) Normalized response of micro-LED versus frequency (b) Measured E-E and E-O bandwidth versus LED bias current

The measured E-E and E-O bandwidth values versus LED bias current are shown in Fig. 4.3 (b). This shows that as the bias current increases from 5 mA to 25 mA, the E-E bandwidth increases from 277 MHz to 450 MHz, and the E-O bandwidth increases from 442

MHz to 641 MHz.

4.3 UV-C SPD DESIGN AND CHARACTERIZATION

4.3.1 SiPM Selection

The SiPM used in Chapter 3 has an active area of 3 mm x 3 mm, which has a DCR of approximately 400 kcps at room temperature. Reducing the temperature to about -10 ℃, the measured DCR was still 35 kcps, which is higher than is required. There are two methods to further reduce the DCR: (1) reduce the active area of the SiPM and (2) further reduce the temperature of the SiPM.

A new SiPM (HAMAMATSU S13360-1350 SPL) with an active area of 1.3 mm x 1.3 mm was used for the enhanced SPD design. This SiPM is not usually used for UV-C applications but was custom-packaged in a TO-18 can with a quartz window by the manufacturer. This package has high transmission in the UV-C region. The reduced area of the device leads to a DCR of 90 kcps at room temperature according to the datasheet.

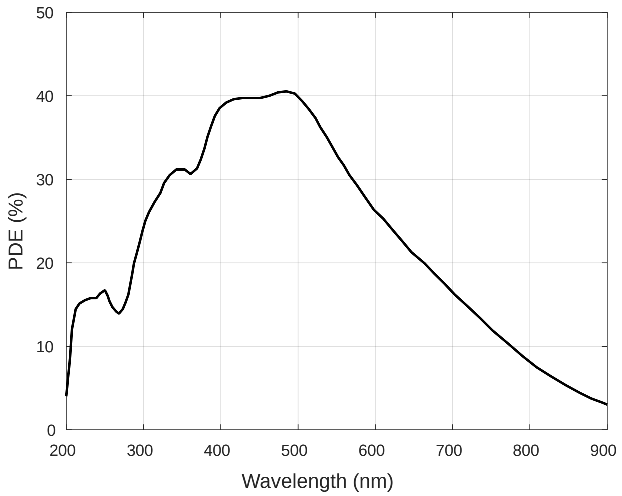

Figure 4.4 PDE of HAMAMATSU 13360-1350SPL

The device is available with a range of pixel sizes (25 µm, 50 µm and 75 µm), and a pixel size of 50 µm was chosen as it provided a balanced trade-off between bandwidth and PDE. Typically, smaller pixels offer higher bandwidth but lower PDE, and 50 µm pixels provide a good compromise between these two [154]. The PDE of the HAMAMATSU S13360-1350 SPL chip is shown in Fig. 4.4. The diagram shows the PDE at 280 nm is approximately 15 %.

4.3.2 PCB Design

A custom PCB was designed for the receiver. This has two functions: (1) supplying a bias voltage to the SiPM and (2) amplifying the signal generated by the SiPM sufficient for detection by an oscilloscope.

4.3.2.1 Bias Voltage Supply

The bias voltage is supplied by an on-chip power supply module (HAMAMATSU C11204-01). The output voltage ranges from 20 V to 90 V, which is sufficient for HAMAMATSU S13360 series SiPMs with a breakdown voltage between 50 V and 60 V. The output voltage is adjusted by software running on a connected PC.

4.3.2.2 Signal Amplification

There are three requirements for signal amplification: (1) sufficient gain for observing pulses resulting from single-photon detection using an oscilloscope, (2) high bandwidth to prevent pulse distortion and (3) low noise.

The amplifier gain was determined based on the amplitude of a single-photon pulse. The data of a single pulse from a HAMAMATSU S13360-1350 SPL is not provided. Thus, the data is obtained from a HAMAMATSU 13360-3050 CS SiPM datasheet. This device has the same pixel size as the SiPM we are considering (so their single pulse outputs should be the same). Fig. 4.5 shows the current of a single pulse versus time (taken from the datasheet). The peak amplitude is around 14.3 µA. Considering the resolution of a typical oscilloscope (e.g. AGILENT MSO6104A) of 2 mV, an amplifier with a trans-impedance load of at least 150 Ω is needed to reach this minimum level.

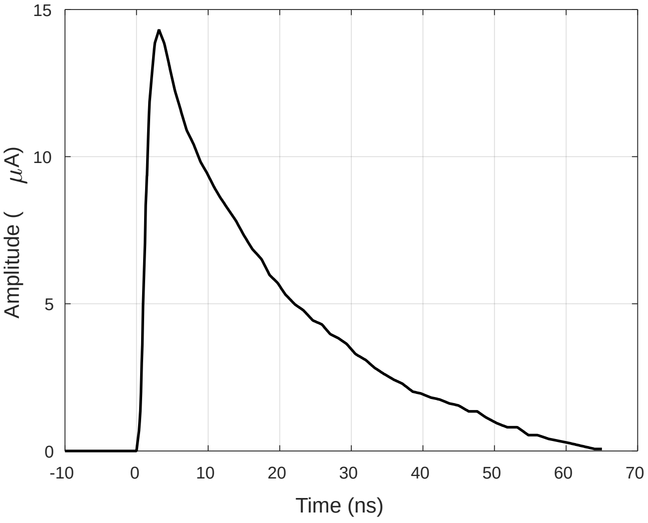

Figure 4.5 Current of a single pulse versus time of an SiPM with 50 µm pixel

The bandwidth of the amplifier should be no less than the bandwidth of the SiPM. Based on the single-pulse shape shown in Fig. 4.5, the bandwidth of the SiPM can be calculated from the rise time of a single pulse by:

$$BW_{SiPM} \approx 0.35/rise\,time \tag{4.1}$$

With a rise time of 1.7 ns, the SiPM bandwidth is calculated as approximately 200 MHz. Thus, the bandwidth of the amplifier should be around this value. A TIA (Texas OPA855-Q1) was chosen because of its high GBWP of 8 GHz and low amplifier noise. The trans-impedance was chosen as 1500 Ω to achieve a sufficiently high single pulse amplitude to be clearly distinguished from a typical oscilloscope's noise floor. Considering the SiPM's capacitance of 60 pF, the estimated bandwidth of the amplifier is calculated as approximately 120 MHz (corresponding to a rise time of 2.9 ns). Thus, there is some distortion when a single pulse from the SiPM passes through the amplifier due to the bandwidth being reduced from 200 MHz to 120 MHz. However, the key factor that affects the performance of ultralow photon flux links is the single pulse width, which is dominated by the fall time (~40 ns). Thus, the predicted increase in the rise time from 1.7 ns to 2.9 ns is acceptable.

4.3.2.3 Noise Analysis

A typical TIA noise model schematic is shown in Fig. 4.6 [170]. The total noise consists of amplifier voltage noise, amplifier current noise, thermal noise $i_{thermal}$ and shot noise i_{shot}. i_a is the input-referred current noise and v_a is the input-referred voltage noise.

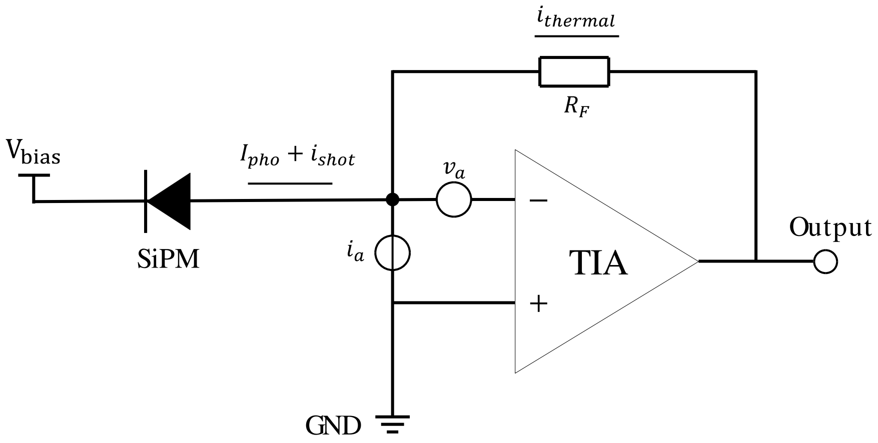

Figure 4.6 A typical TIA noise model schematic

The amplifier voltage noise and current noise can be combined as an amplifier noise [171]:

$$i_{amplifier} = \left(i_a + \pi C_{¿} v_a f_{3dB}\right) \cdot \sqrt{f_{3dB}} \quad (4.2)$$

The thermal noise mainly comes from the trans-impedance load:

$$i_{thermal} = \sqrt{\frac{4 k_B T_R f_{3dB}}{R_F}} \quad (4.3)$$

Where k_B is the Boltzmann constant and T_R is the temperature of the trans-impedance load. The shot noise can be obtained by:

$$i_{shot} = \sqrt{2 q I_{pho} f_{3dB}} \quad (4.4)$$

Where q is the elementary charge and I_{pho} is the photocurrent into the amplifier. Thus, the total noise is:

$$i_{noise}^{2} = i_{amplifier}^{2} + i_{thermal}^{2} + i_{shot}^{2} \quad (4.5)$$

To verify the feasibility of using the OPA855-Q1 for the UV-C SPD, the noise was estimated using the parameters in Table 4.1.

Table 4.1 Parameters and values used for simulating noise

Parameters	Values
Bandwidth	120 MHz
Input-referred current noise	2.5 $pA/\sqrt{Hz}$
Input-referred voltage noise	0.98 $nV/\sqrt{Hz}$
Temperature of the trans-impedance load	300 K
Trans-impedance load	1500 Ω (refer to section 4.3.2.2)

The input-referred current noise and input-referred voltage noise were obtained from the datasheet of the TIA. The temperature of the trans-impedance load was assumed to be room temperature. The calculated current version of input amplifier noise, thermal noise and shot noise are 0.24 μA, 36 nA and 24 nA, respectively. These noises were used to simulate a noisy received single pulse. The single pulse was also filtered using a first-order Butterworth filter with a cutoff frequency of 120 MHz, matching the amplifier bandwidth described in section 4.3.2.2. The corresponding simulation result is shown in Fig. 4.7. The results show the pulse shape is distinguishable after adding the simulated noise. The peak amplitude of the single pulse in Fig. 4.7 is slightly lower than that in Fig. 4.5. This is because the bandwidth is reduced from 200 MHz (see Fig. 4.5) to 120 MHz. The peak amplitude of a single pulse at the amplifier output is expected to be 18 mV with a 1500 Ω trans-impedance gain. However, considering the 50 Ω output resistance of the amplifier and the 50 Ω input impedance of the oscilloscope, the peak amplitude displayed on the oscilloscope is expected to be 9 mV. Therefore, the amplifier design with OPA855-Q1 and a 1500 Ω trans-impedance load should satisfy the requirements of the system.

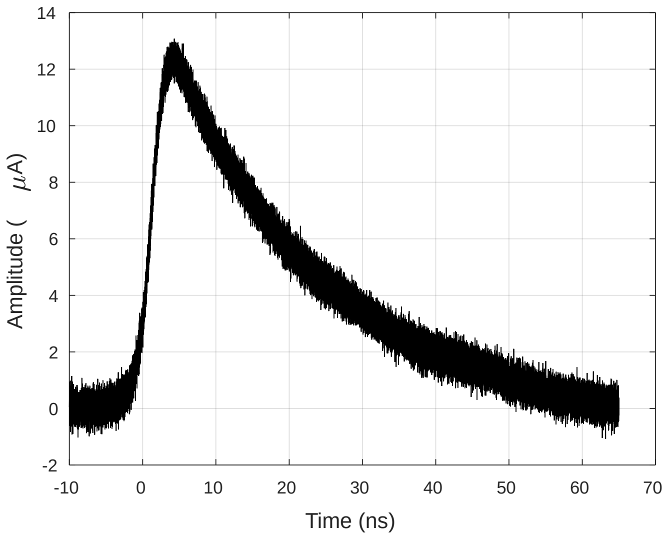

Figure 4.7. Simulated amplitude of a single pulse with noise versus

time

4.3.2.4 PCB Production

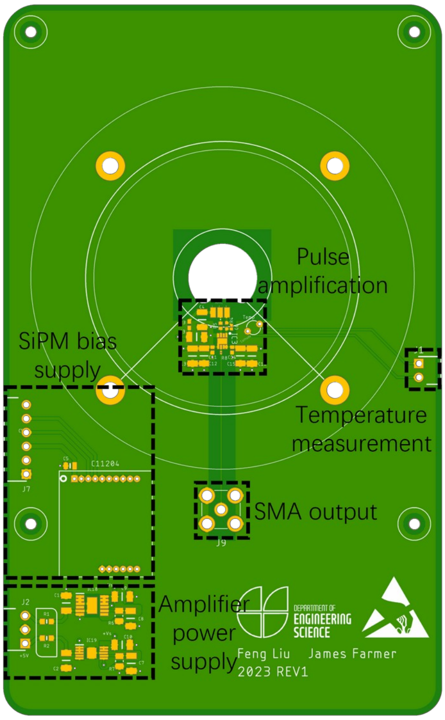

Figure 4.8 Layout of PCB

A PCB that contains the amplifier and SiPM bias was designed and produced. This is a 4-layer board, which allows multiple ground layers to prevent interference and ensure good low-noise performance. Fig. 4.8 shows the layout of PCB. The SiPM bias supply uses an integrated HAMAMATSU C11204-01 to provide a bias voltage to the SiPM. There are two regulators (LT3093 and LT3042) within the amplifier power supply, supplying +2.5 V and -2.5 V to the amplifier. A Texas OPA855-Q1 is used as a TIA to amplify pulses from the SiPM. The temperature of the SiPM is measured by a sensor and a signal is sent to the TEC controller. The output of the TIA is connected to the oscilloscope via a SMA connection.

4.3.3 Liquid Cooling Design

Chapter 3 describes a liquid cooling design with a separate SiPM and amplifier. The relatively long cable connecting the SiPM and the amplification circuit will introduce capacitance and potential interference. For these reasons, a modified liquid cooling design was developed, with the SiPM and amplifier mounted on a single PCB. A sectional view of the design is shown in Fig. 4.9.

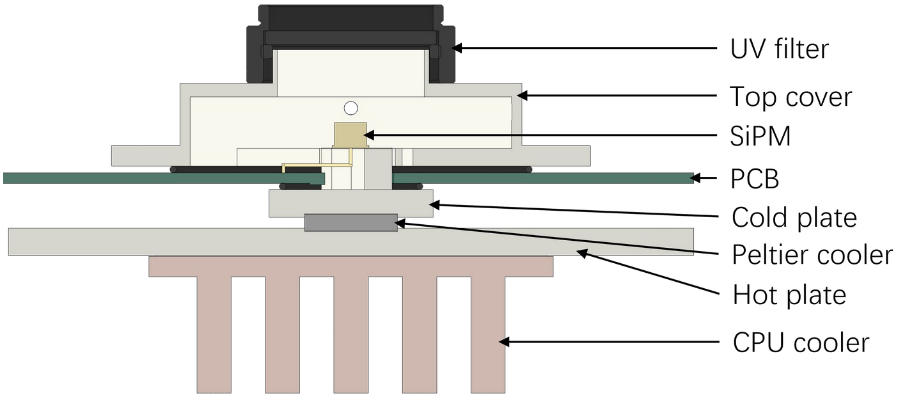

Figure 4.9 Sectional view of modified cooling design

The central component is a Peltier cooler (OTX20-68-F1A-1313-11-W2.25). On the cold side, a cold plate with a “pedestal” that passes through a hole in the PCB, establishes a thermal connection between the SiPM and the Peltier cooler. The cold plate is fabricated from ceramic aluminium oxide because of its high thermal conductivity (~30 W/mK) and effective electrical isolation. Because the temperature will be reduced to below 0 ℃, to prevent condensation, a plastic top cover and a UV filter (Thorlabs FGUV5M) are used to create a confined space around the SiPM. A vacuum pump (RS vacuum pump) is used to evacuate the air from the confined space. In addition, O-rings are used to ensure a good seal.

On the hot side, the heat flows to a liquid CPU cooler (MASTER LIQUID LITE 240) through the hot plate, which is also made of aluminium oxide. The purpose of the CPU cooler is to remove heat from the hot side, rather than to directly cool the temperature of the SiPM. To achieve temperature control, an NTC thermistor (TDK B57540G1103F005) is placed on the cold plate close to the SiPM using thermal adhesive (Electrolube TBS20S). A TEC controller (Meerstetter Engineering TEC-1161-4A) obtains the temperature value from the thermistor through the PCB (see section 4.3.2.4) and dynamically drives the Peltier cooler to control the temperature of the SiPM.

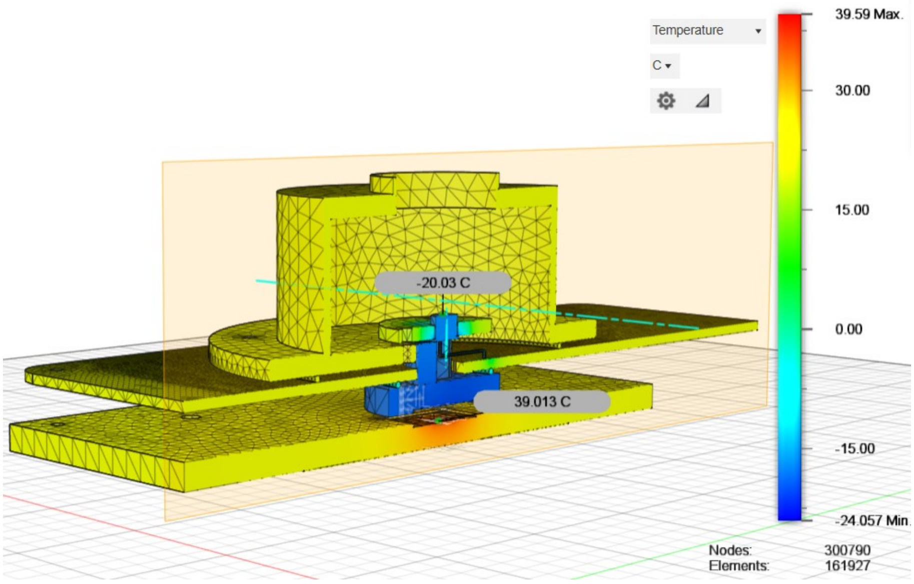

Figure 4.10 Sectional view of the liquid cooling structure with simulated temperature

A thermal simulation was carried out to estimate the performance of the liquid cooling design using Autodesk Fusion 360. The cold side (hot side) of the Peltier cooler was a cold (hot) heat source with a power of -1.6 W (10.95 W). This value was obtained from the datasheet of the Peltier cooler, assuming a driving current of 1.4 A. The convective heat transfer coefficient of the surface between the hot plate and the CPU cooler was 1600 $W/m^2 \cdot K$ (obtained from the datasheet of the CPU cooler). The convective heat transfer coefficient of other surfaces was 20 $W/m^2 \cdot K$, which is a typical value of natural convection of air [172]. A sectional view of the liquid cooling structure with simulated temperature is shown in Fig. 4.10. The result shows the temperature of the SiPM is approximately -20 ℃, while the hot side of the Peltier cooler stabilizes at around 40 ℃, thanks to the effective heat dissipation by the CPU cooler.

4.3.4 UV-C SPD Characterization

An image of the UV-C SPD is shown in Fig. 4.11. The UV-C SPD was mounted on the optical table within a light-tight enclosure to ensure a dark operating environment.

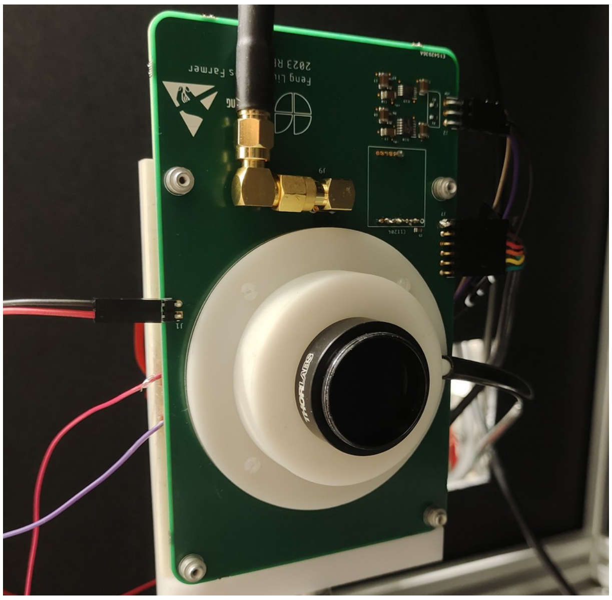

Figure 4.11 An image of the UV-C SPD

Dark current versus temperature was measured to test the UV-C SPD. The PCB and TEC controller were remotely controlled by a PC to change the bias voltage and temperature, respectively. The dark current was measured by a source meter (KEITHLEY 2636B). The bias voltage was varied (from 54.34 V to 51.91 V) with temperature (from 25 ℃ to -20 ℃) to ensure the overvoltage remained constant. This ensured constant PDE and gain.

Fig. 4.12 (a) shows the dark current of the SiPM changing with bias voltage and temperature. The red curve in Fig. 4.12 (b) shows the dark current versus temperature under the recommended bias voltage. The dark current reduces by approximately 11 dB with a 30 ℃ temperature reduction, consistent with the result reported in [153] and section 3.4.4. The dark current at 25℃ and -20℃ are 29.08 nA and 0.57 nA, respectively. Further reducing the temperature is challenging, limited by the capability of the Peltier cooler, CPU cooler and SiPM construction.

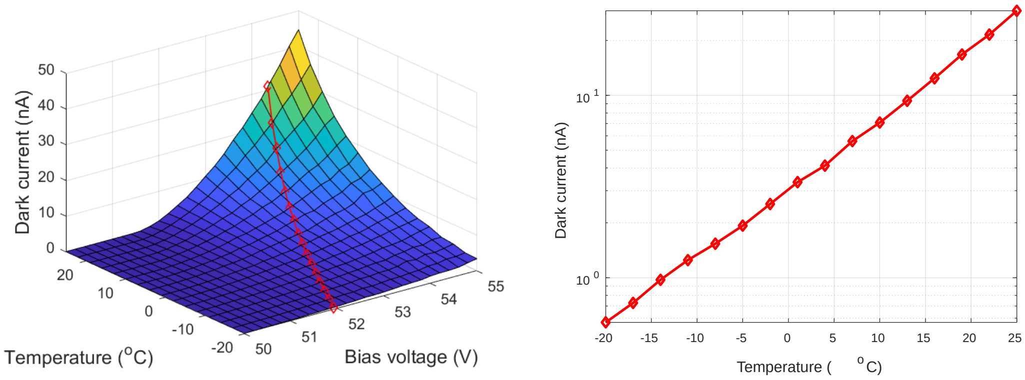

(a) (b)

Figure 4.12 (a) Dark current versus bias voltage and temperature (b) Dark current versus temperature under recommended bias voltage

Then, the responsivity of the SiPM and DCR were measured to obtain the PDE and gain. A power meter (Newport 843-R with a UV-enhanced Si head 818 UV/DB) was used to measure the irradiance from the micro-LED. Subsequently, the UV-C SPD replaced the power meter at the same position. A source meter (KEITHLEY 2636B) was used to measure the output current of the SiPM. The current from the SiPM, including both photocurrent and dark current, varying with irradiance at both 25 ℃ and -20 ℃ is shown in Fig. 4.13. It can be seen that the two curves overlap each other well, indicating that the PDE and gain remain constant at 25℃ and -20℃.

The SiPM approaches saturation when the irradiance exceeds 10 mW/m^2, corresponding to a received power of 17 nW. The difference between the two curves at the beginning reflects different dark currents at these two temperatures.

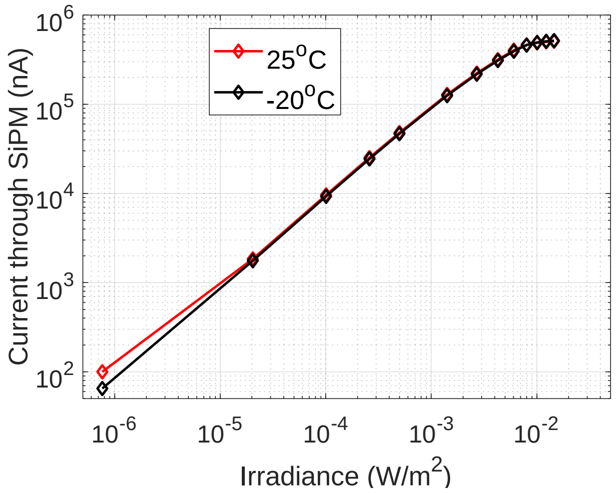

Figure 4.13 Current from the SiPM versus irradiance at the aperture of the UV-C SPD

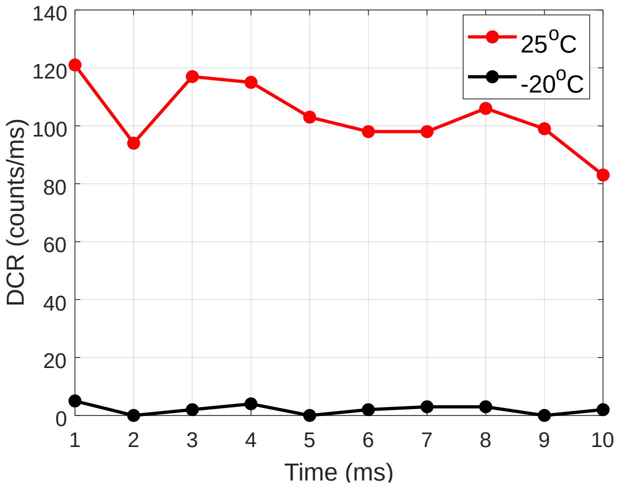

Figure 4.14 DCR versus time

The output from the amplifier was captured by an oscilloscope (AGILENT MSO6104A) to obtain the DCR. The number of dark counts during a 10 ms period, summed every 1 ms, is shown in Fig. 4.14. The DCR at 25℃ and -20℃ are calculated as 103.4 kcps and 2.1

kcps, respectively. Considering the dark current values in Fig. 4.12, the gain of the SiPM is calculated as 1.76×10^{6} and 1.7×10^{6} at 25℃ and -20℃. The PDE is calculated as 14.24% and 14.76% at 25℃ and -20℃.

The captured dark pulses at 25℃ and -20℃ are plotted in Fig. 4.15. Fig. 4.15 (a) and (c) represent dark pulses within a 1 ms period, showing a significant reduction in the number of dark counts with cooling. Fig. 4.15 (b) and (d) show two zoomed-in single pulses at 25℃ and -20℃, respectively.

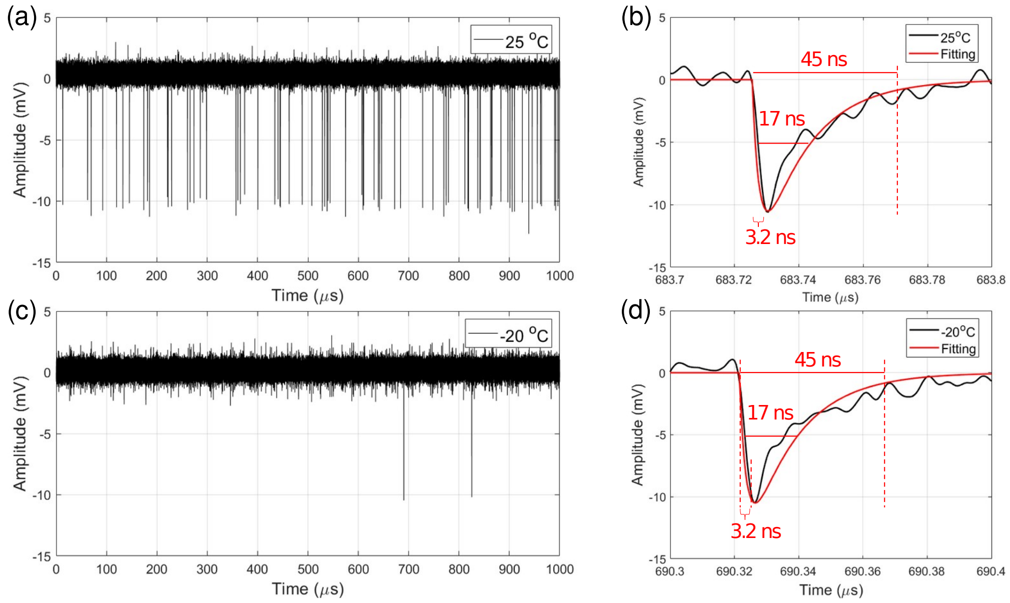

Figure 4.15 Dark pulses during 1 ms period and zoomed-in single pulses under 25℃ and -20℃

Exponential fits to the pulse shape are also shown in Fig. 4.15. These are defined by [160]:

$$A_f(t)=A_0\cdot\left(e^{\frac{-t}{T_r}}-e^{\frac{-t}{T_f}}\right) \quad (4.6)$$

Where A_0 is the amplitude of the single pulse. T_r and T_f are the rise time and fall time of the single pulse, respectively. The fitting curves show that both pulses have a peak amplitude of approximately 10.5 mV, with a rise time (from 10% to 90% peak amplitude) of 3.2 ns. Thus, the practical 3-dB bandwidth of the UV-C SPD is estimated at 110 MHz, according to Eq. (4.1). The FWHM of the single pulse is 17 ns. The dead time of each pixel is approximately 45 ns, with the dominant contributor being the fall time, constrained by the SiPM's quenching time.

4.4 ULTRALOW PHOTON FLUX OWC LINKS

Ultralow photon flux links were demonstrated to test the sensitivity of the UV-C SPD and the feasibility of building a UV-C QKD link using the UV-C micro-LED and the UV-C SPD.

4.4.1 Experimental Testbed

The experimental setup for the ultralow photon flux links demonstration is shown in Fig. 4.16.

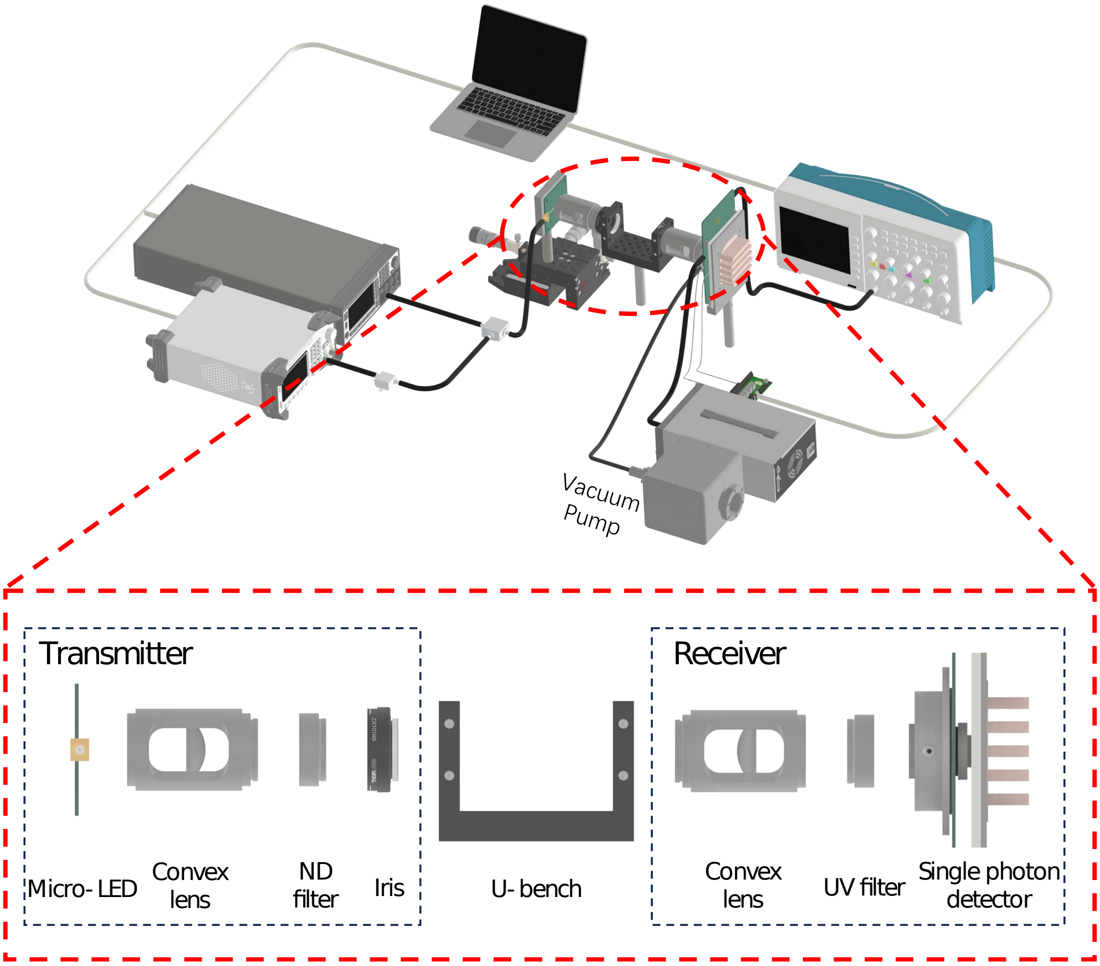

Figure 4.16 Experimental setup for ultralow photon flux links demonstration

At the transmitter, a modulated signal was generated by an arbitrary waveform generator (AWG, Tektronix AWG70002) and amplified by an RF amplifier (iXblue DR-AN-20-MO) with 20 dB gain. An RF amplifier is used, as the output voltage of the AWG is limited to between 250 mV and 500 mV, which is insufficient to modulate the micro-LED. Then, the amplified modulated signal and DC bias from the source meter were combined by a Bias Tee. The combined signal was connected to the micro-LED. A convex lens was placed in a slotted tube (Thorlabs SM1L20C) and used to collimate the light emitted from the micro-LED. A 3-axis stage (Thorlabs RBL13D/M) was used to mount and adjust the micro-LED’s position, ensuring precise collimation by the convex lens. An ND filter (Thorlabs NDUV30A) and an iris (Thorlabs SM1D12CZ) were employed to attenuate the optical power to a specific value. The diameter of the light beam was constrained to 6 mm by the iris. A U-bench (Thorlabs CBB1/M) connected the transmitter and the receiver for precise alignment.

At the receiver, a convex lens focused the collimated light onto the active area of the SiPM. The UV filter (Thorlabs FGUV5M) at the entrance to the SiPM permitted only UV light to enter. The received power can be calculated as:

$$P_{RX} = P_{TX} \cdot T_{lens} \cdot T_{filter} \quad (4.7)$$

Where P_{TX} is the transmitted power. T_{lens} and T_{filter} are the transmission of the convex lens and UV filter, which are 92% and 83%, respectively. These values were measured by placing the convex lens and UV filter (separately) between the UV-C micro-LED and a power meter and comparing transmitted power against the value with no component present.

The received pulses were displayed on the oscilloscope and captured for post-processing. The source meter, AWG, TEC controller, oscilloscope and PCB were all remotely controlled by a PC.

4.4.2 Cascaded Post-Processing Strategy

There are two post-processing strategies used:

- Direct post-processing: The bit decision is achieved directly by comparing the minimum amplitude of the received signal within a detection window with a decision threshold. (Note that the received signal is inverted, so the minimum signal represents a transmitted symbol)

- Cascaded post-processing (CPP): The received signal is differentiated to mitigate the ISI due to the long fall time of pulses [173]. Then, the differentiated signal values are summed within a detection window. For OOK links, the bit decision is achieved by comparing the summed value with a threshold. For PPM links, the symbol decision is achieved by finding the minimum summed value among all time slots within a symbol.

The key to the CPP strategy is the differentiation. Previous research has proven that differentiation can efficiently mitigate the ISI caused by the long fall time of pulses [173, 174]. Fig. 4.17 shows a received pulse with and without differentiation.

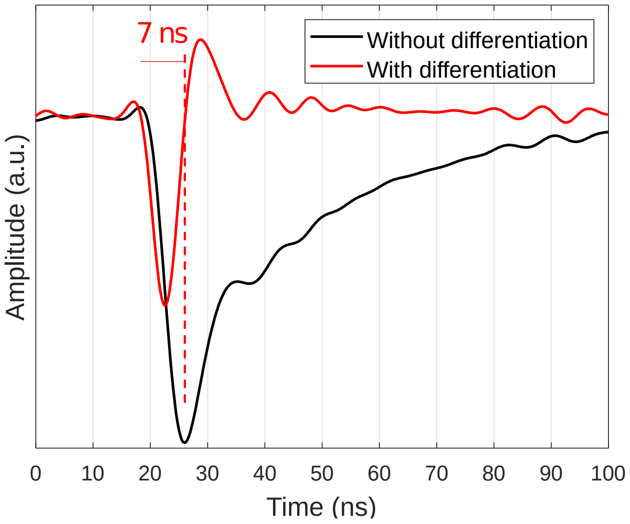

Figure 4.17 Amplitude of a received pulse with and without differentiation

The time duration of a single pulse is reduced to approximately 7 ns with differentiation, compared with 45 ns without differentiation. The effect of the positive peak following the negative peak is negligible because only the points within the detection windows are used for the symbol/bit decision. In our work, the differentiation is achieved by taking the first-order derivative of the received pulse. Higher differentiation orders have been used in other work [174]. However, investigation showed that first-order differentiation worked best in this case.

4.4.3 OOK Link Demonstration

4.4.3.1 OOK links with direct post-processing

At the transmitter, a PRBS sequence with a length of $2^{10} = 1024$ bits was generated by a PC and sent to the AWG, which then drove the micro-LED to emit OOK signals. The data rate varied from 1 Mbit/s to 10 Mbit/s and the pulse width was set at 10 ns. At the receiver, the OOK signal was detected by the UV-C SPD. The detection window was set to 10 ns to match the transmitted pulse width. The decision threshold was fixed at -9 mV (approximately 90% of the peak value of single pulses). The average received photon number per bit was fixed at ~30, corresponding to ~0.22 nW received power at a data rate of 10 Mbit/s [53].

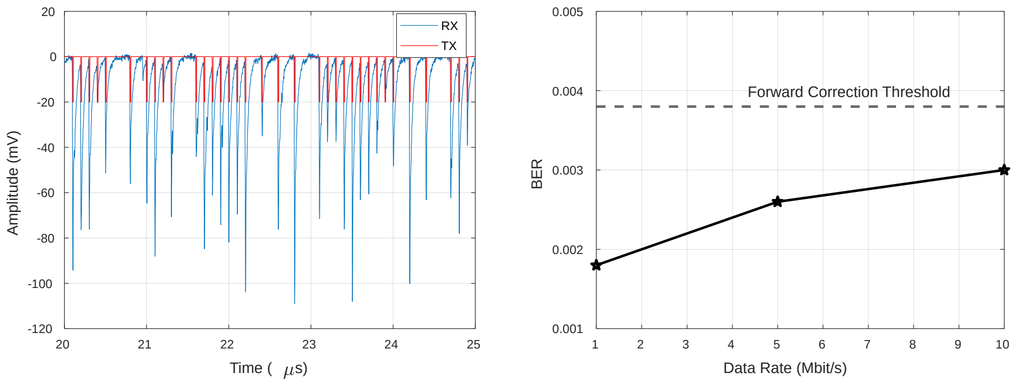

(a) (b)

Figure 4.18 (a) Synchronized received signal and transmitted sequence (b) BER versus data rate for OOK with direct post-processing

Fig. 4.18 (a) shows a synchronized received signal and a transmitted sequence for a data rate of 10 Mbit/s. Note that the received data values are negative, as an inverting amplifier is used on the PCB board. The -20 mV and 0 mV levels in the transmitted sequence represent “1” and “0”, respectively. The measured BER versus data rate is shown in Fig. 4.18 (b). When the data rate is 10 Mbit/s, BER is measured as 3×10^{-3}, which is less than the FEC threshold of 3.8×10^{-3}. The BER increases with the data rate because the ISI caused by afterpulses increases [52].

4.4.3.2 OOK links with CPP

At the transmitter, an OOK signal (generated by a PRBS sequence with a length of 2^{10} = 1024 bits) with a data rate ranging from 5 Mbit/s to 50 Mbit/s, and a pulse width set at 10 ns, was transmitted by the UV-C micro-LED. At the receiver, the signal was received and post-processed using the CPP. There are 8 values within a detection window, due to a 2 ns detection window and a 4 GSa/s sampling rate. After differentiation, 8 values (corresponding to a detection window) were summed and compared with a decision threshold. The decision threshold was fixed at “-10”, which is approximately 8 times 90 % of the peak amplitude of a single-photon pulse after the differentiation. If the summed value was less than the threshold, the bit was “1”, otherwise “0”.

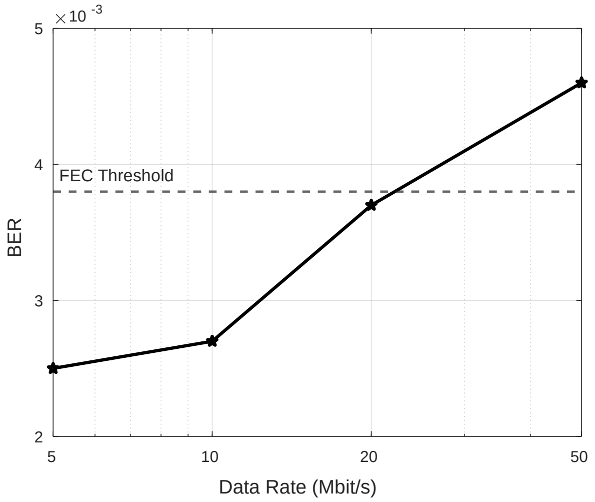

Figure 4.19 BER versus data rate for OOK with CPP

The measured BER versus data rate is plotted in Fig. 4.19. The result shows the BER increases as the data rate rises. The maximum data rate below the FEC threshold reaches 20 Mbit/s with a BER of 3.7×10^{-3}. Compared with the result in Fig. 4.18 (b), due to the CPP, the maximum data rate is improved from 10 Mbit/s to 20 Mbit/s because of lower ISI.

4.4.4 PPM Link Demonstration

A PPM modulation scheme was used to further reduce the transmitted power. PPM encodes information by transmitting a pulse within one of the multiple time slots in each symbol period. For example, an 8-PPM scheme uses 8 time slots per symbol, thus 3 bits per symbol. Previous research has demonstrated that the PPM scheme is an effective approach to improving power efficiency, a critical factor in building deep-space and underwater optical communication systems [160-162, 175]. However, it requires precise timing synchronization at the receiver and generally has lower spectral efficiency compared to simpler modulation schemes such as OOK.

At the transmitter, a PRBS sequence was modulated onto a PPM sequence with a length of 2^7 = 128 symbols to drive the micro-LED (The AWG has a waveform memory of 16 Gsamples). The sequence length was limited by the oscilloscope’s memory, which supports up to 4000000 samples per data capture. The pulse width of a time slot within each symbol was set as 2 ns, considering the measured micro-LED’s E-O bandwidth of around 500 MHz. The average transmitted photon number per symbol was 60 and the symbol rate varied from 100 kilobaud per second (kb/s) to 50 Mb/s. The corresponding PPM index *M*, bit rate, photons per bit and transmitted power are shown in Tables 4.2 and 4.3. Considering the maximum transmitted power of 2.16 nW and 6 mm beam diameter, the irradiance is calculated as $76\,\mu W/m^2$, less than the safety exempt level $1\,mW/m^2$.

Table 4.2 Parameters and values of 128-PPM links at the transmitter

Symbol rate (Mb/s)	**0.1**	**0.2**	**0.5**	**1**	**2**	**3**
Bit rate (Mbit/s)	0.7	1.4	3.5	7	14	21
Photons per bit	8.5	8.5	8.5	8.5	8.5	8.5
Transmitted power (pW)	4.32	8.64	21.6	43.2	86.4	129.6

Table 4.3 Parameters and values of 8-PPM links at the transmitter

Symbol rate (Mb/s)	**2**	**5**	**10**	**20**	**40**	**50**
Bit rate (Mbit/s)	6	15	30	60	120	150
Photons per bit	20	20	20	20	20	20
Transmitted power (pW)	86.4	216	432	864	1728	2160

At the receiver, the detection window was set as 2 ns to match the pulse width at the transmitter. The received signal was synchronized to the transmitted PPM sequence by correlation. The received signal was converted to a received PPM sequence based on either direct post-processing or the CPP. Then, the received PPM sequence was demodulated and compared with the PRBS sequence in the transmitter to obtain the BER. The symbol error rate (SER) was obtained by comparing the transmitted PPM sequence and the received PPM sequence.

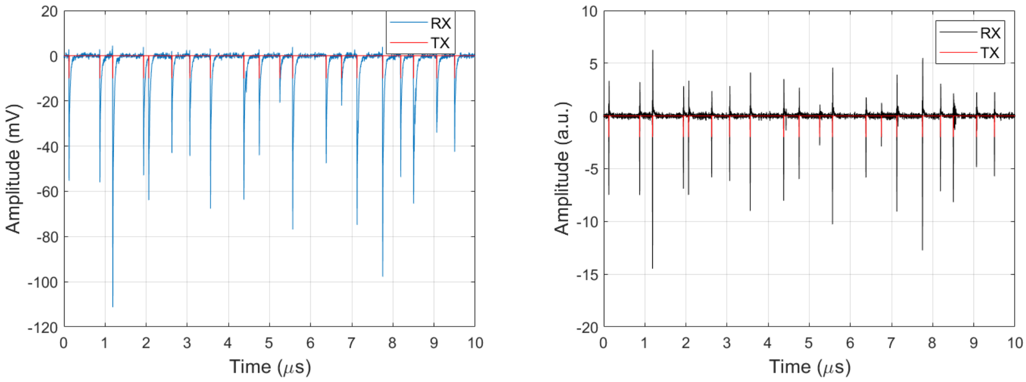

(a) (b)

Figure 4.20 Synchronized received signal and transmitted PPM sequence for the 2 Mb/s 8-PPM link (a) received signal without CPP (b) received signal with CPP

The synchronized received signal (RX) and transmitted PPM sequences (TX) for 8-PPM links are illustrated in Fig. 4.20, 21 and 22, with symbol rates of 2 Mb/s, 10 Mb/s and 40 Mb/s, respectively. The -10 mV (or “–2”) and 0 mV (or “0”) in TX lines represent values of “1” and “0” in the transmitted PPM sequences, respectively. The amplitude of the received signal is variable because the number of detected photons in each symbol is changing, following a Poisson distribution. Comparing Fig. 4.20 (a), 4.21 (a) and 4.22 (a), the ISI of the received signal where there is no CPP is increasingly severe with the increasing symbol rate. However, the usage of CPP significantly mitigates the ISI, which can be seen in Fig. 4.22.

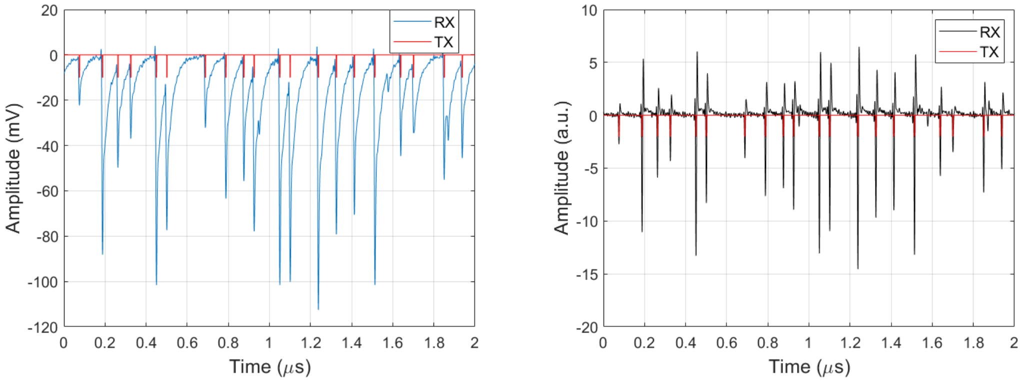

(a) (b)

Figure 4.21 Synchronized received signal and transmitted PPM sequence for the 10 Mb/s 8-PPM link (a) received signal without CPP (b) received signal with CPP

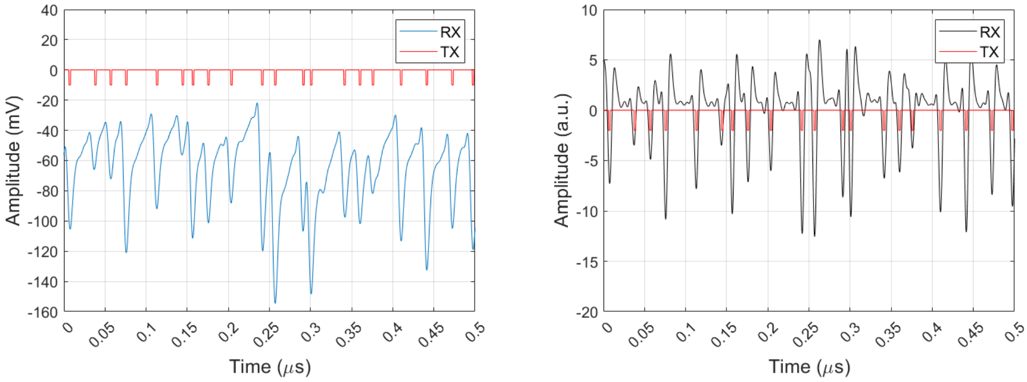

(a) (b)

Figure 4.22 Synchronized received signal and transmitted PPM sequence for the 40 Mb/s 8-PPM link (a) received signal without CPP (b) received signal with CPP

Fig. 23 shows both the transmitted sequence and received signal (10 symbols) of the 40 Mb/s 8-PPM link in detail, further highlighting the advantage of using CPP. The figure shows that the detection of symbol 3 is incorrect without CPP, as the transmitted time slot 3 is incorrectly decided as time slot 8. However, the usage of CPP removed this incorrect detection.

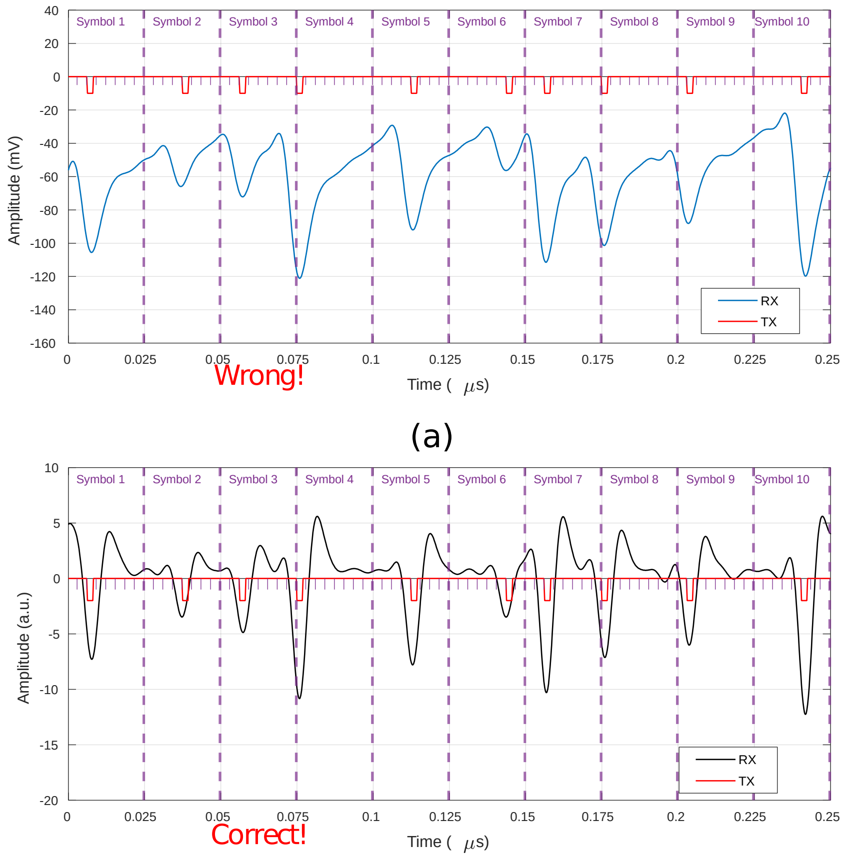

(a)

(b)

Figure 4.23 Ten synchronized symbols for the 40 Mb/s 8-PPM link (a) without CPP (b) with CPP

The calculated SER and BER versus symbol rate are shown in Fig. 4.24 (a) and Fig. 4.24 (b). Each point of the BER or SER curves was calculated by transmitting $100\times2^7=12800$ symbols. In this context, each symbol in 128-PPM (8-PPM) represents 7 (3) bits, meaning the bit rate is 7 (3) times the symbol rate. The SER represents the probability that a transmitted symbol is incorrectly received, while the bit error rate (BER) is the error probability per bit. Since each symbol contains multiple bits, and a symbol error does not imply that all bits are incorrect, the SER is typically higher than the BER under the same conditions. The result shows that, using direct post-processing, the BER increases from 1.8×10^{-3} to 1.17×10^{-2} and the SER increases from 3.6×10^{-3} to 2.96×10^{-2} as the symbol rate increases from 100 kb/s to 3 Mb/s for 128-PPM links. Both SER and BER increase with the symbol rate because of the ISI (due to the long fall time and afterpulses) [159].

The CPP mitigates the ISI, so both SER and BER are reduced. For the 3 Mb/s 128-PPM link, the BER is reduced to 2.9×10^{-3}, lower than the FEC threshold. Due to the limitation of the transmitter bandwidth, the symbol rate cannot be further increased. This is because the minimum detection window will be larger than the time slot required to support higher symbol rates. It can also be seen that CPP contributes little improvement to performance at low symbol rates. This is because the detection time slot is large enough to accommodate the response of the UV-C SPD, so there is no ISI in the received signals. For 8-PPM links, when the symbol rate rises from 2 Mb/s to 50 Mb/s, the BER increases from 1.9×10^{-3} to 7.43×10^{-2} and the SER increases from 3.4×10^{-3} to 1.33×10^{-1}. With the CPP, the BER of 40 Mb/s 8-PPM link decreases to 2.9×10^{-3}. In this case, a maximum bit rate of 120 Mbit/s is achieved before ISI becomes too substantial.

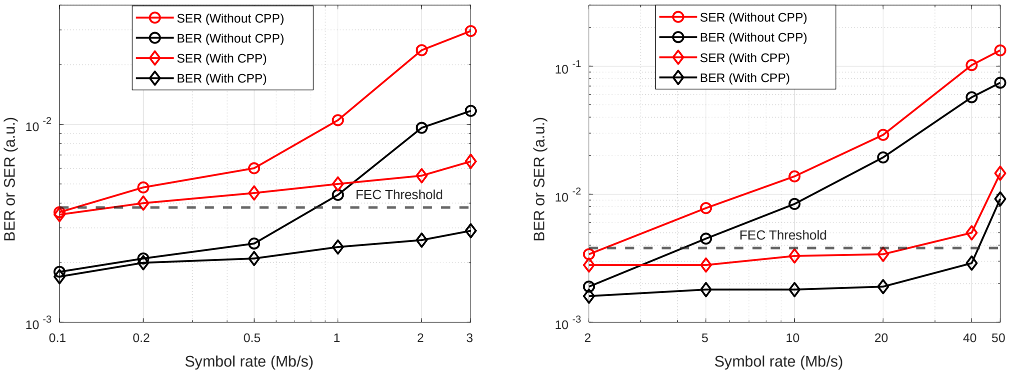

(a) (b)

Figure 4.24 (a) BER and SER versus symbol rate at 128-PPM links (b) BER and SER versus symbol rate at 8-PPM links

To further explore the sensitivity limit of the UV-C SPD, the average transmitted photon number per symbol was varied from 40 to 70 for 128-PPM links with a symbol rate of 1 Mb/s (corresponding to transmitted power between 28.8 pW and 50.4 pW). Fig. 4.25 shows the BER and SER versus transmitted power for 1 Mb/s 128-PPM links. Both BER and SER decrease with the increase in transmitted power (the received power can be obtained according to Eq. (4.7)). This is because the probability of symbols being received with zero detected photons is reduced, due to the increasing mean of the Poisson distribution. When the transmitted power is 38.85 pW, corresponding to 7.7 (54) transmitted photons per bit (symbol), the BER is equal to the FEC threshold. Based on the Poisson distribution, the standard quantum limit for PPM is 5 detected photons per symbol for a BER of 3.8×10^{-3} [158]. In this work, considering the losses due to convex lens transmission, UV filter transmission and SiPM PDE, the 54 transmitted photons per symbol correspond to 6.1 detected photons per symbol. To achieve the quantum limit of 5 detected photons per symbol, the SiPM's temperature or active area should be further reduced to minimize the DCR, while advancements in manufacturing technology are needed to mitigate the impact of afterpulses.

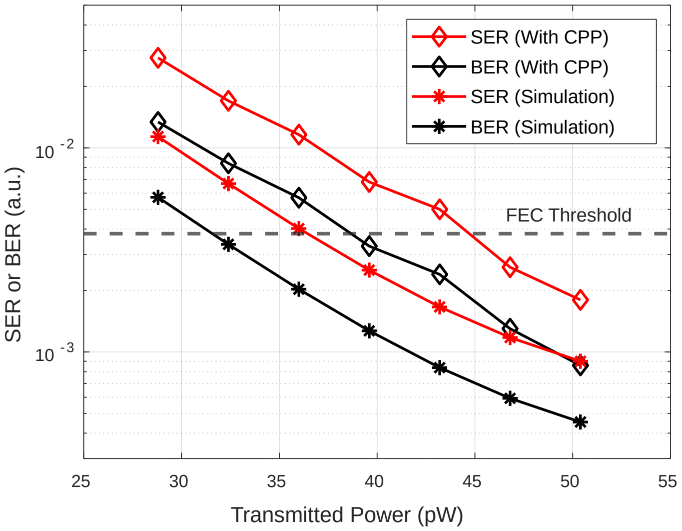

Figure 4.25 BER and SER versus transmitted power at 1Mb/s 128-PPM links with CPP

Additionally, simulation results are added to Fig. 4.25 to compare with the experimental result. The theoretical analysis of SER and BER refers to section 3.2.2. The simulation result performs better than the experimental result in terms of SER and BER. This is because the simulation does not consider ISI, due to the long fall time and afterpulses. Typically, an additional 7-10 pW of power is required to compensate for the effects of ISI at 1 Mb/s for 128-PPM links, in order to achieve similar BER and SER.

To further investigate the impact of long fall time and afterpulses, the simulated (see Fig. 4.25) and experimental results (see Fig. 4.24) for 128-PPM links at 1 Mb/s and 0.1 Mb/s are compared. Both the long fall time and afterpulses contribute to ISI at 1 Mb/s, whereas only afterpulses contribute at 0.1 Mb/s (as the detection window is longer than the pulse duration). The simulated BER is calculated as $8.4 \times 10^{-4}$for both symbol rates. The experimental BER is $2.4 \times 10^{-3}$and 1.7×10^{-3}at 1 Mb/s and 0.1 Mb/s respectively. Thus, the difference in BER between experiment and simulation is reduced from 1.56×10^{-3} to 8.6×10^{-4}. This reduction occurs because the effect of long fall time is eliminated, leaving afterpulses as the source of the remaining difference. The change in SER follows a similar trend to that of the BER.

In addition to differentiation, the matched filter is another method to reduce ISI [160]. Based on using the matched filter or/and differentiation, there are four options: (1) differentiation, (2) matched filter, (3) matched filter followed by the differentiation and (4) differentiation followed by the matched filter.

The matched filter was implemented using a simple ‘integrate and dump’ scheme. For each timeslot, the measured pulse shape was multiplied by the simulated pulse shape, and the result was integrated. Decisions were then based on whether the result was above or below a threshold. Different simulated pulse shapes are required, depending on whether the signal has been differentiated. For options (2) and (3), data from Fig. 4.15 (d) is used, and data from Fig. 4.17 is used for option (4).

The SER and BER of 40 Mb/s 8-PPM links using these four options are shown in Table 4.4. The result shows using only differentiation achieves the best SER and BER performance. This is because the shape of received pulses is changing due to the overlap of multiple single pulses. Thus, an optimal matched filter does not exist.

Table 4.4. SER and BER based on using a matched filter or/and differentiation

Option	SER	BER
(1) Differentiation	0.0050	0.0029
(2) Matched filter	0.1130	0.0627
(3) Matched filter followed by the differentiation	0.2595	0.1316
(4) Differentiation followed by the matched filter	0.0298	0.0182

4.4.5 Single-Photon Link Demonstration

In addition to OOK and PPM links, a single-photon link was built to verify the UV-C SPD’s single-photon counting ability towards building a BB84 QKD system.

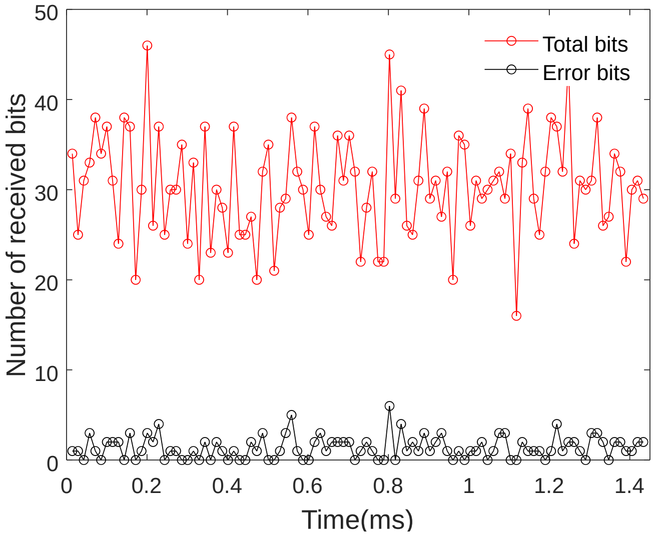

Figure 4.26 Number of received bits versus time (over 1.43 ms) for a 500 MHz repetition rate.

The demonstration of a single-photon link uses the same approaches and methods for the OOK links with the CPP, as shown in section 4.4.3.2. In this case, the transmitted optical power was attenuated to 0.07 photon per bit “1”. Fig. 4.26 shows the number of received bits per 7×2^{10} transmitted bits (corresponding to ~14.3 μs) for a repetition rate of 500 MHz. The repetition rate was 500 MHz. The results show that the total numbers of received bits per 7×2^{10} transmitted bits fluctuate at around 30. This measured number is similar to an expected number of $7 \times 2^{10} \times 0.07 \times 0.92 \times 0.83 \times 0.1476 \approx 29$, according to Eq. (4.7).

The BER and bit rate versus repetition rate are plotted in Fig. 4.27. BER increases from 0.26% to 4.32% with a repetition rate ranging from 50 MHz to 500 MHz. A maximum bit rate of 2.12 Mbit/s is achieved. Although the BER is insufficient for communications purposes it is within the range that allows QKD operation, as will be discussed in the next Chapter.

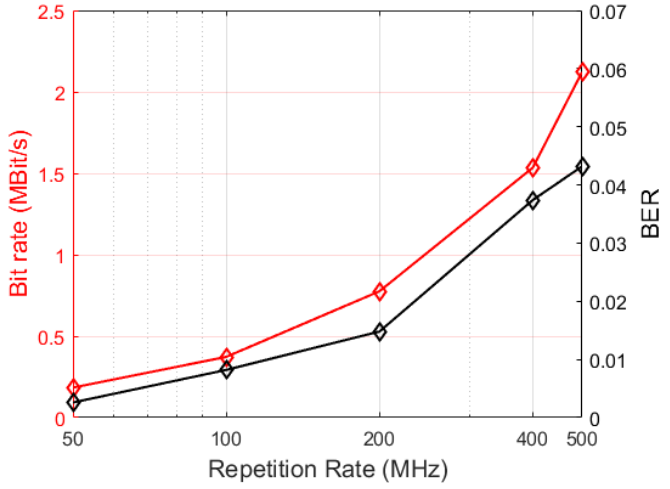

Figure 4.27 Bit rate and BER versus repetition rate for the single-photon link

4.5 CONCLUSIONS

This Chapter presents work on establishing ultralow photon flux links based on a UV-C micro-LED and a UV-C SPD. The micro-LED has a bandwidth of over 400 MHz and a central wavelength of 276 nm. The UV-C SPD has a PDE of 14.76 % and a DCR of 2.1 kcps at a temperature of -20 ℃. A minimum transmitted average photon number per bit of 7.7 was demonstrated in 1 Mb/s 128-PPM links and a maximum data rate of 120 Mbit/s was achieved in 40 Mb/s 8-PPM links. Moreover, a 500 MHz repetition rate single-photon link was demonstrated, resulting in a BER of 4.32% and a measured bit rate of 2.12 Mbit/s. This shows that UV-C SPD is sufficiently sensitive for establishing a Mbit/s-level UV-C QKD link using a UV-C micro-LED.

The next Chapter will report the modelling and demonstration of a UV-C wireless QKD link based on the single-photon link demonstrated in this Chapter.

Chapter 5:

UV-C Short-Range Wireless B92 QKD

5.1 INTRODUCTION

Quantum Key Distribution (QKD) is a cryptographic technique that ensures secure communication based on the principles of quantum mechanics [23]. Among the various QKD protocols shown in Chapter 2, the B92 protocol stands out as a simple and effective method for quantum encryption [90]. Compared with the BB84 protocol, which utilizes two non-orthogonal bases (four states), the B92 protocol employs only two non-orthogonal quantum states for key generation. Thus, the B92 protocol is more hardware-efficient as it requires only half the number of light sources and detectors compared to the BB84 protocol. However, this comes at the cost of half the rate of key transmission.

B92 QKD has been demonstrated in fibre-based systems, and theoretical analysis of wireless B92 QKD has been explored [176-180]. However, no experimental implementations of wireless B92 QKD links have been reported to date. Chapter 4 presents single-photon links, using a UV-C micro-LED and a UV-C SPD. Based on this foundation, this Chapter will focus on implementing a wireless B92 QKD link using these devices.

In this Chapter, a theoretical model of the UV-C wireless B92 QKD system is first proposed. QBER & SKR estimation and simulation show the feasibility of a practical QKD system robust to sunlight interference. Then, a practical QKD transmitter and receiver are presented and characterized. Horizontal (H) or diagonal (D) polarizations are used to encode bits in the transmitter, and anti-diagonal (A) or vertical (V) polarizations are used to decode bits in the receiver. The QKD links are demonstrated with an inferred SKR of over 1 Mbit/s. Finally, the ambient light rejection performance of our QKD system is analyzed, and the strategy for full robustness to sunlight is proposed.

5.2 MODELLING OF UV-C WIRELESS B92 QKD

A block diagram of a wireless B92 QKD system is shown in Fig. 5.1. At the transmitter (Alice), two sources, S1 (H, horizontal polarization) and S2 (D, diagonal polarization), are used. Each source includes a UV-C micro-LED, a convex lens and a polarizer. The convex lens collimates light emitted from the UV-C micro-LED, followed by a linear polarizer (H or D) to determine the polarization of emitted photons. The collimated and polarized light from each source is combined by a non-polarizing beam splitter and directed to a spatial filter. The spatial filter contains two convex lenses and a pinhole. The filter ensures that the beams of light from S1 and S2 are identical spatially. The filter operates as follows: the first convex lens focuses the light into the pinhole and the second convex lens recollimated the light. An optical filter (a narrow bandpass filter) is placed after the spatial filter to reshape the spectrum of S1 and S2 to ensure they are identical spectrally. The diameter of the transmitter beam is defined by an iris placed at the transmitter output. Identical output intensity is achieved by adjusting the driving voltage of S1 and S2.

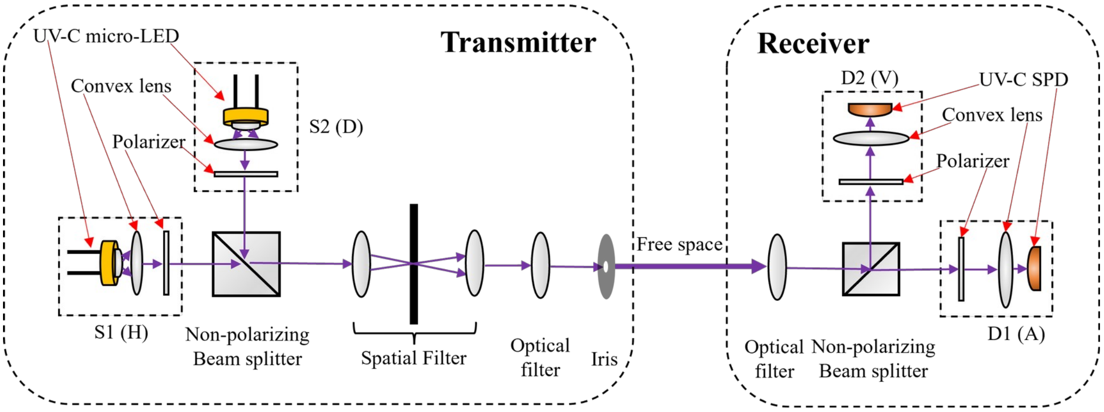

Figure 5.1 Structure of a wireless B92 QKD system

At the receiver, an optical filter (a narrow bandpass filter) passes the wavelength of incident light and rejects the ambient light at other wavelengths. Then, a non-polarizing beam splitter splits the incoming light. The output beams from the beam splitter are received by two UV-C SPDs. The polarizer (A, anti-diagonal or V, vertical) determines the detection polarization, and a convex lens focuses the light onto the active area of two UV-C SPDs.

The total link loss is made up of the geometric loss and optical loss due to optics. The collimated light emitted from the transmitter is modelled as a Gaussian beam. The corresponding power density follows:

$$I(L)=I_0\left(\frac{W_0}{W(L)}\right)^2\exp\left(\frac{-2L^2}{W(L)^2}\right) \quad (5.1)$$

where L is the link length between the transmitter and receiver. $W_0=\frac{\lambda}{\pi\Theta n}$ is the waist radius, where θ is the beam's half FOV, λ is the wavelength and n is the refractive index of the atmosphere. $W(L)$ is given by $\sqrt{1+\left(\frac{L}{L_0}\right)^2}$, where $L_0=\frac{\pi W_0^2 n}{\lambda}$. I_0 is the power density factor which is given by $\frac{2P_0}{\pi W_0^2}$, where P_0 is the initial beam power. Thus, the geometric transmission is calculated by integration (assuming the transmitter and receiver are aligned):

$$T_g(L)=\begin{cases}\int_0^{r_c} 2\pi r I(L)\,dr, L\cdot\tan(\theta)\geq r_c\\ \int_0^{L\cdot\tan(\theta)} 2\pi r I(L)\,dr, L\cdot\tan(\theta)\leq r_c\end{cases} \quad (5.2)$$

where r_c is the radius of the receiver’s collection area.

The calculation of QBER is as follows. The photon number in each qubit follows the Poisson distribution due to a single-photon level qubit. The probability of getting no less than one detected photon per qubit is [52]:

$$P_s=1-e^{-PDE\cdot N_p\cdot T_g(L)\cdot T_o(L)} \quad (5.3)$$

where N_p is the transmitted average photon number per qubit. $T_o(L)$ is the total transmission of all optics used in the receiver.

The noise consists of noise due to ambient light and dark counts. The noise due to ambient light comes from sunlight interference, which is defined by the ASTM 1.5 Spectra [51]. The optical power from the ambient light is calculated as:

$$U_a=I_a A_c \Delta\lambda \frac{\tan^2\left(\frac{FOV}{2}\right)}{2} \quad (5.4)$$

where I_a is the irradiance of sunlight and A_c is the receiver’s collection area, in this case the area of the convex lens. The FOV is the receiver's field of view (FOV) and $\Delta\lambda$ is the optical bandwidth of the receiver's optical filter. Then, the probability of detecting pulses created from ambient light per bit is:

$$P_a=\frac{U_a\lambda}{hc}\cdot PDE\cdot t_d \quad (5.5)$$

where h is Planck's constant and t_d is the duration of the detection window (similar to Eq. (3.1)). The probability of detecting dark counts per bit is:

$$P_d=1-e^{-DCR\cdot t_d} \quad (5.6)$$

Then, the QBER can be calculated as [21]:

$$QBER=\frac{\frac{1}{2}(P¿¿d+P_a)}{P_s+\frac{1}{2}(P¿¿d+P_a)+n_i¿} \quad (5.7)$$
$$¿$$

The coefficient $1/2$ indicates that dark counts and pulses created by ambient light have a 50% chance of occurring in the UV-C SPD detection channel which will contribute to errors. n_i represents the error due to system imperfection, such as polarization state imperfection due to component (i.e. beamsplitter) performance, optical misalignment and timing jitter [21]. A typical value of n_i is 1%.

The SKR is calculated based on the QBER. The transmitter sends *N* qubits to the receiver, with only N_μ qubits are used for key transmission. Within these N_μ qubits, N_μ^S is the number of qubits using matched polarizations in the transmitter and receiver, such as horizontal → in the transmitter while anti-diagonal   in the receiver (see details in section 2.2.1.2). Within these N_{μ}^{S} bits, K_{μ}^{S} is the number of qubits where the receiver correctly detects the received photons. The normalized SKR is the number of generated secure keys when one qubit is transmitted, which can be obtained from [181, 182]:

$$SKR \geq q\left\{-Q_{\mu} H\left(E_{\mu}\right)+Q_{1}\left[1-H\left(e_{1}\right)\right]\right\} \tag{5.8}$$

where *q* is N_{μ}^{s}/N and Q_{μ} is K_{μ}^{s}/N_{μ}^{s}. $H(x)=-x\log_{2}x-(1-x)\log_{2}(1-x)$ is the Shannon binary entropy function and E_{μ} is equal to $QBER$. Q_{1} and e_{1} are the gain and QBER of single-photon qubits respectively. When we assume all loss and errors come from qubits with a single photon, e_{1} is [182]:

$$e_{1}=\frac{Q_{\mu}E_{\mu}}{Q_{1}} \tag{5.9}$$

The value of Q_{μ} and Q_{1} are obtained, assuming the transmitter has a weak coherent source which generates Poisson distribution pulses. The density function of the Poisson distribution $\rho(i)$is:

$$\rho(i)=\frac{\mu^{i}}{i!}e^{-\mu} \tag{5.10}$$

where i represents *i*-photon qubits, where each qubit contains i photons, and μ is the average number of photons per qubit. The link transmission of *i*-photon qubits Y_{i} is:

$$Y_i = 1 - \left(1 - PDE \cdot T_g(L) \cdot T_o(L)\right)^i \quad (5.11)$$

Thus, the probability of detecting *i*-photon qubits is:

$$Q_i = Y_i \frac{\mu^i}{i!} e^{-\mu} \quad (5.12)$$

Thus, Q_μ can be obtained:

$$Q_\mu = \sum_{i=1}^{\infty} Y_i \frac{\mu^i}{i!} e^{-\mu} \quad (5.13)$$

Therefore, considering Eq. (5.7), (5.9), (5.12), (5.13) and using the result in Eq. (5.8), the normalized SKR can be obtained.

A simulation was carried out, based on the above system model, to investigate the potential of establishing a practical UV-C wireless B92 QKD link. The parameters and corresponding values are listed in Table 5.1. At the transmitter, an average photon number per qubit of 0.1 and a transmitter FOV of 1° was used. At the receiver, the detection window is set as 2 ns. The error correction efficiency and system imperfection are typical values used in QKD demonstrations. Other values are all obtained based on commercial devices.

Table 5.1 Parameters and values for UV-C wireless B92 QKD simulation

Part	Parameter	Value
Transmitter	Average photon number per qubit	0.1
	Half transmitter FOV	1°
Receiver	Detection window	2 ns

Optical bandwidth (set by optical filter)	10 nm
Diameter of convex lens	50.8 mm
Half receiver FOV	1°
PDE (HAMAMATSU S13360-1350 SPL)	14.76 %
Error correction efficiency	1/1.22 [64]
System imperfection	1 % [21]
(a) Transmission of optical filter	60%
(b) Transmission of BS	49.49%
(c) Reflectance of BS	49.46%
(d) Transmission of polarizer	86.54%
(e) Transmission of convex lens	92.46%

Note: The optics used in (a) to (e) are: (a) Edmund 280 nm OD4 10 nm bandpass filter, (b) Thorlabs BSW20R, (c) Thorlabs BSW20R, (d) Thorlabs GLB10-UV and (e) Thorlabs LA4052-UV. Parameter values are from the respective data sheets.

The simulation also assumes: (1) no eavesdroppers interrupt the QKD link (2) Decoy states are not applied, so all qubits are used for generating keys (3) The transmitter and receiver are aligned and (4) The PDE is constant with varying wavelengths.

The operating wavelength of a UV-C QKD system was first investigated. The link length and DCR are set as 1 m and 5 kcps, respectively. The wavelength used is varied from 270 nm to 290 nm, in order to examine the influence of ambient light. Fig. 5.2 (a) shows the QBER versus wavelength. It can be seen that the QBER is nearly unchanged between 270 nm and 286 nm, as the DCR and system imperfection dominate the total noise, and both of these are constants. When wavelength increases to longer than 286 nm, the ambient interference dominates the total noise. This is because the power density of ambient sunlight increases extremely quickly between 280 nm and 300 nm, as indicated by the ASTM 1.5 Spectra. Thus, the QBER rises over the QKD threshold, and the QKD system will not be feasible.

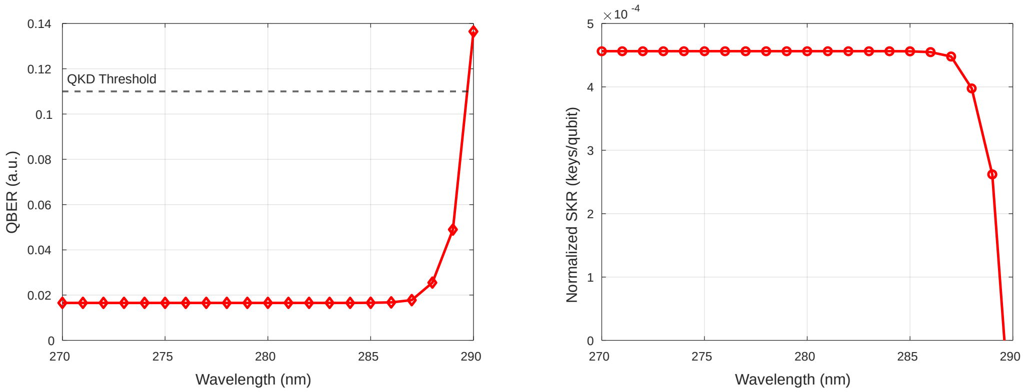

(a) (b)

Figure 5.2 (a) QBER versus wavelength (b) SKR versus wavelength

Fig. 5.2 (b) shows the plot of the normalized SKR vs wavelength, where the normalized SKR is defined as the ratio of the number of final secure keys to the total transmitted qubits. The result shows that the operating wavelength must be less than 289 nm.

The next challenge is to find an acceptable value of DCR. A link was simulated for a wavelength of 280 nm and a link length of 1 m (other values in Table 5.1). The QBER and SKR versus DCR are shown in Fig. 5.3 (a) and (b), respectively. The result shows the QBER rises from 1 % to approximately 11.5 %, as the DCR increases from 0 kcps to 100 kcps. Fig 5.3 shows the required DCR for a theoretical QKD link should be below 80 kcps to obtain a non-zero SKR. Previously reported practical wireless QKD links typically maintain a QBER below 5% to ensure a reliable SKR [47, 48, 119]. Therefore, a DCR below 30 kcps is a more realistic target, with lower values being preferable. Notably, in previous Chapters, we already achieved a DCR below 5 kcps, which corresponds to a QBER of approximately 1.7 % (as shown in Fig. 5.3 (a)).

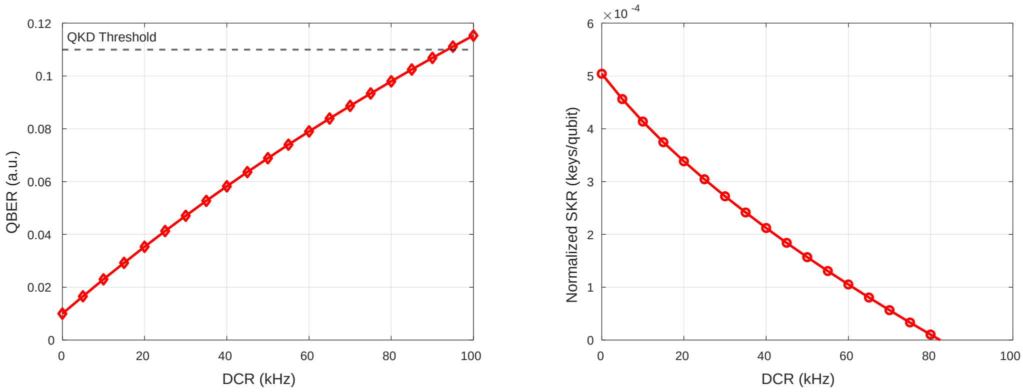

(a) (b)

Figure 5.3 (a) QBER versus DCR (b) SKR versus DCR

The last factor to consider is the link length/link loss. The wavelength and DCR are set as 280 nm and 5 kcps respectively, and the QBER vs link length is estimated and shown in Fig. 5.4 (a). The result shows that QBER is almost unchanged when the link length is less than 3m. The reason is that the geometric loss is unchanged, as all the light from the transmitter is incident on the receiver. When the link length is more than 3m, the beam spot at the receiver is larger than the collection area. The increasing geometric loss then increases rapidly, which results in a rapid rise in QBER. The corresponding plot of normalized SKR vs link length is in Fig. 5.4 (b). It can be seen that the maximum link length must be less than 16 m for operation below the QKD threshold. Furthermore, the link length is converted into link loss, considering both geometric loss and optical loss. The corresponding QBER and SKR performance is shown in Fig. 5.4 (c) and (d).

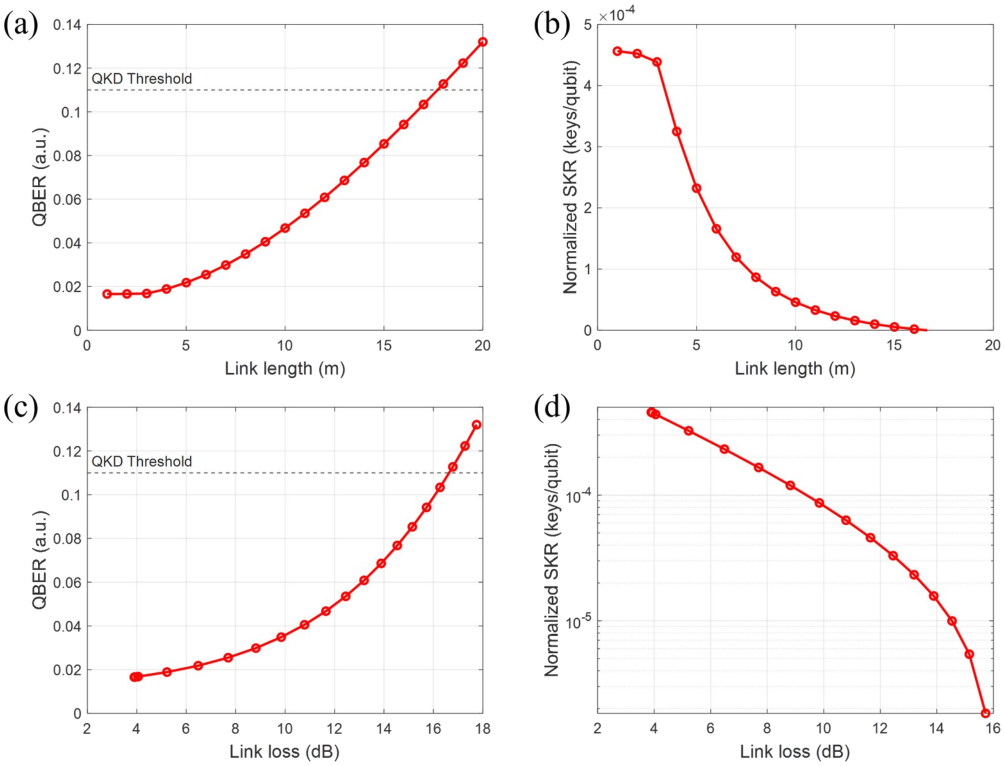

Figure 5.4 (a) QBER versus link length (b) SKR versus link length (c) QBER versus link loss (b) SKR versus link loss

In conclusion, based on simulation results, the requirements for building a UV-C short-range wireless B92 QKD system are an operating wavelength of less than 289 nm and a DCR of below 30 kcps. The central wavelength of the UV-C micro-LED and the DCR of the UV-C SPD presented in Chapter 4 are 276 nm and 2.1 kcps respectively, and these satisfy the requirements determined by simulation. In the next section, the elements of an experimental system are described, beginning with the transmitter.

5.3 TRANSMITTER SETUP AND CHARACTERIZATION

The experimental setup of the QKD transmitter consists of both an electrical and an optical subsystem. Fig. 5.5 (a) and (b) shows the photograph and block diagram of the electrical subsystem. This uses two channels (H and D) for driving two separate micro-LEDs, each of which generates light with a specific polarization, either horizontal (H) or diagonal (D). In each channel, the AC signal from an AWG (Tektronix AWG70002A) is amplified by an RF amplifier (iXblue DR-AN-20-MO). An attenuator is used to prevent high voltage damage to the micro-LED (The voltage supplied to the micro-LED must be less than 12 V according to Figure 4.2). The amplified AC signal is combined with a DC signal from a source meter (KEITHLEY 2636B) by a Bias Tee (Mini-Circuits ZFBT-6GW), and the combined signal is used to drive the micro-LED.

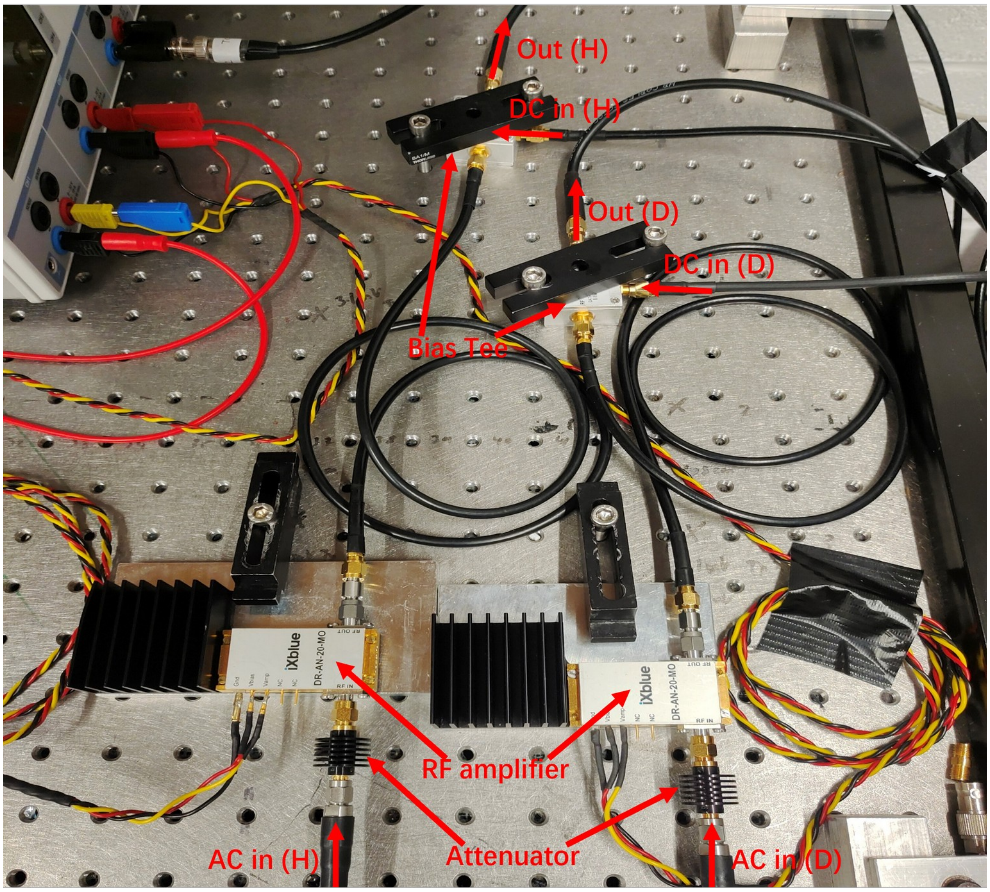

(a)

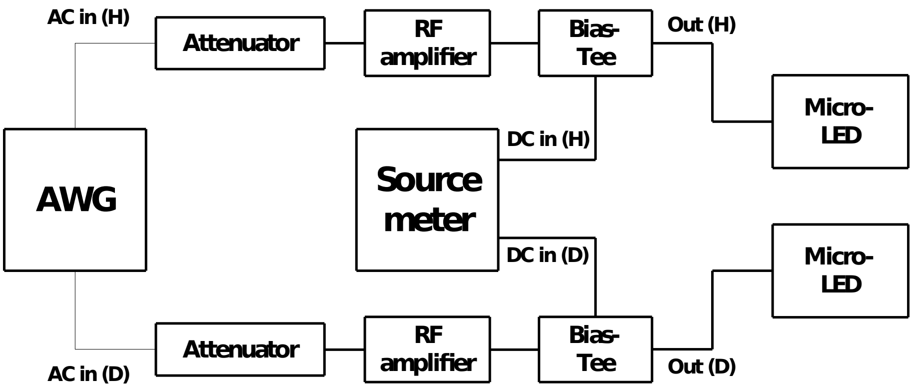

(b)

Figure 5.5 QKD transmitter electrical subsystem (a) Photograph (b) Block diagram

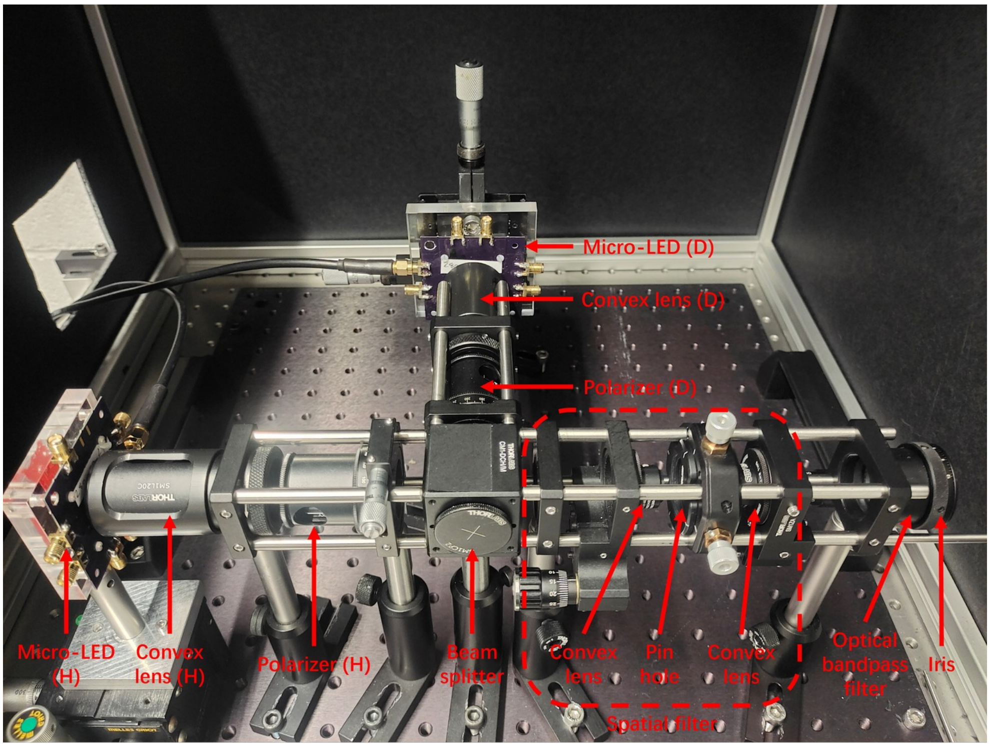

Figure 5.6 Photograph of the QKD transmitter optical subsystem

Fig 5.6 shows a photograph of the QKD transmitter optical subsystem. Two micro-LEDs (H and D) are used as sources for the two QKD channels. In each channel, the light emitted from the micro-LED is collimated by a convex lens (Thorlabs LA4052-UV). Each micro-LED is mounted on a 3-axis stage (Thorlabs RBL13D/M) and aligned with a convex lens, which is placed in a slotted tube

(Thorlabs SM1L30C). The polarization is defined by a crystal linear polarizer (Thorlabs GLB10-UV) and the light from two channels is combined by a non-polarizing beam splitter (Thorlabs BSW20R). The combined light propagates through a spatial filter, which consists of two convex lenses (Thorlabs LA4647-UV-ML) and a pinhole (Thorlabs P100K). The positions of two convex lenses and a pinhole are adjusted by Z-axis Translation Mounts (Thorlabs SM1ZA) and XY Translation Mounts (CXY1A), respectively. Finally, an optical bandpass filter (Edmund 280nm hard coated OD4 10nm bandpass filter) reshapes the spectrum, and an iris constrains the beam aperture to 2 mm. An ND2 filter (Thorlabs NDUV20A) is placed at the end of the QKD transmitter to attenuate the transmitted light power to a single-photon level. All the optics are mounted on a movable base plate, which is fixed on an optical table. The whole QKD transmitter is enclosed, preventing the UV-C light from potentially causing hazards to operators.

The I-V-I curves and bandwidth of the micro-LED used have been measured as part of the work described in Chapter 4, and the data shown in Fig. 4.2 and 4.3 are used here. QKD requires sources that are spectrally indistinguishable, so a series of experiments were undertaken to assess this. First, the spectrum of sources without a narrow bandpass filter was measured by placing an optical spectrum analyzer (Ocean Insight OFX00951) at the output of the transmitter and measuring the spectrum. The driving current of two micro-LEDs was varied from 10 mA to 20 mA and the spectrum measured in both cases.

Then, the narrow bandpass filter was placed at the end of the transmitter and the spectrum of filtered sources was measured with the same process. Fig. 5.7 shows the spectrum of two sources with and without the filter. The results show the spectrum of two sources without the optical bandpass filter is different so that Eve can distinguish the light from the two sources and eavesdrop on information. However, the reshaped spectrum using the optical bandpass filter is indistinguishable, which ensures the security of QKD.

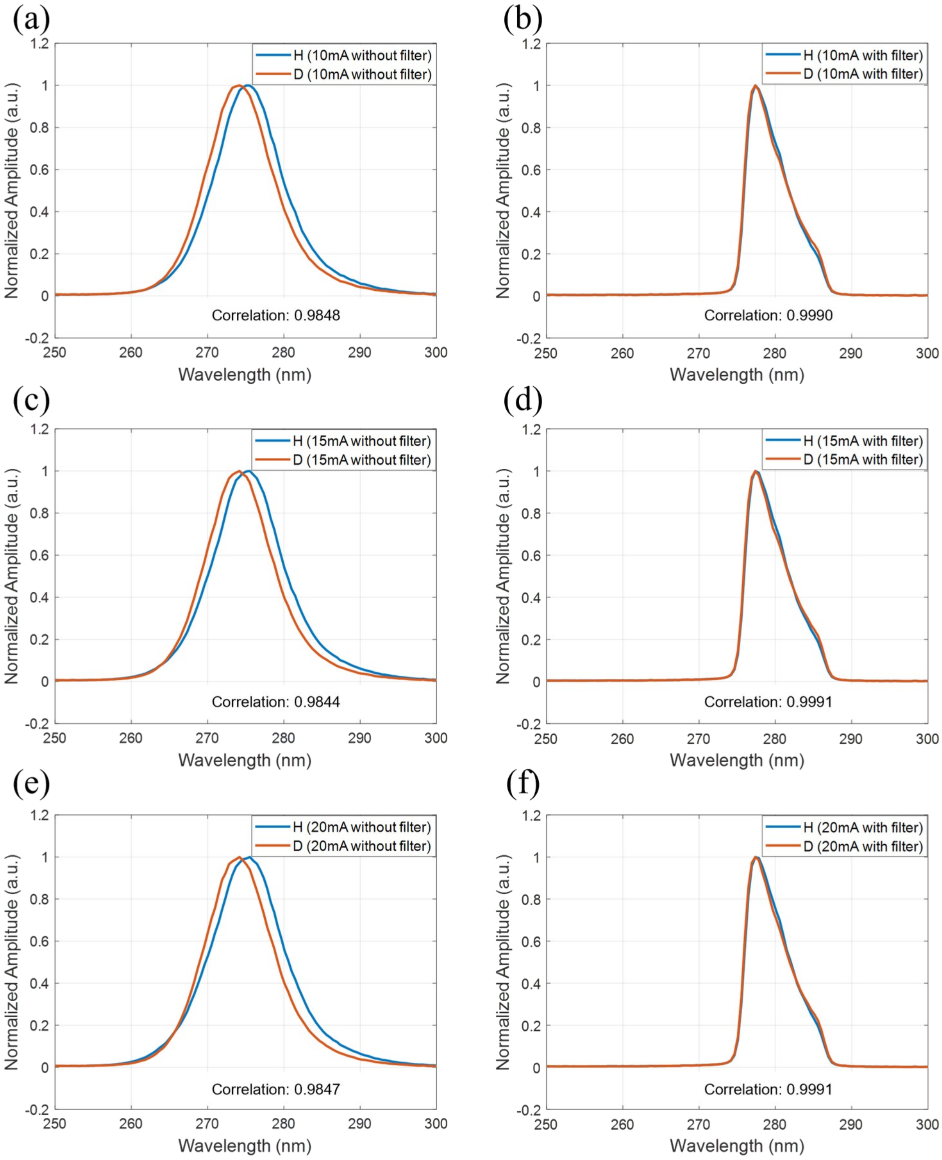

Figure 5.7 The spectrum of the S1 and S2 micro-LEDs (a) 10 mA current without filter (b) 10 mA current with filter (c) 15 mA current without filter (d) 15 mA current with filter (e) 20 mA current without

filter (f) 20 mA current with filter

Additionally, the correlation value between the two curves in each figure was calculated (see Fig. 5.7) to quantitatively assess the indistinguishability. The correlation is obtained by:

$$corr=\frac{\sum(x-\bar{x})(y-\bar{y})}{\sqrt{\sum(x-\bar{x})^2}\sqrt{\sum(y-\bar{y})^2}} \quad (5.14)$$

where x and y are values of two curves. $\bar{x}$ and $\bar{y}$ are the means of two curves. The result shows that the correlation value between the spectrum of the two sources is improved by using the filter.

5.4 RECEIVER SETUP AND CHARACTERIZATION

Fig. 5.8 shows the experimental setup of the QKD receiver. An optical bandpass filter (Edmund 280nm hard coated OD4 10nm bandpass filter) is placed at the input of the receiver to block ambient light at wavelengths different from the light from the transmitter. The incident light is split by a non-polarizing beam splitter (Thorlabs BSW20R) into two channels (A and V). In each channel, a crystal linear polarizer (Thorlabs GLB10-UV) is rotated to a particular polarization (diagonal or antidiagonal). A convex lens (Thorlabs LA4052-UV) collects light and focuses it on the active area of a UV-C SPD. Each UV-C SPD is mounted on a 3-axis stage, which adjusts the SPD’s position to achieve maximum received light power. The design and operation details of the UV-C SPD can be found in Section 4.3. The signals generated by the two UV-C SPDs are sent to two channels of the oscilloscope (AGILENT MSO6104A). The corresponding data displayed on the two channels are collected by a PC for postprocessing. The QKD receiver is mounted on a movable base plate to allow alignment and is enclosed in a light-tight box. The distance between the transmitter and receiver is 25 cm.

Experiments were undertaken to characterize receiver performance. DCR is a key factor affecting the performance of a QKD system. The measurement of the two UV-C SPDs' DCRs is carried out using the same method presented in Section 4.3.3. The temperature is reduced from 25℃ to -15℃ with the bias voltage varied from 54.34 V to 52 V to maintain a constant overvoltage. Table 5.2 presents the DCR measurement. The result shows the DCR of two UV-C SPDs is reduced from 103.4 kcps and 110.5 kcps to 3 kcps and 2.9 kcps, respectively.

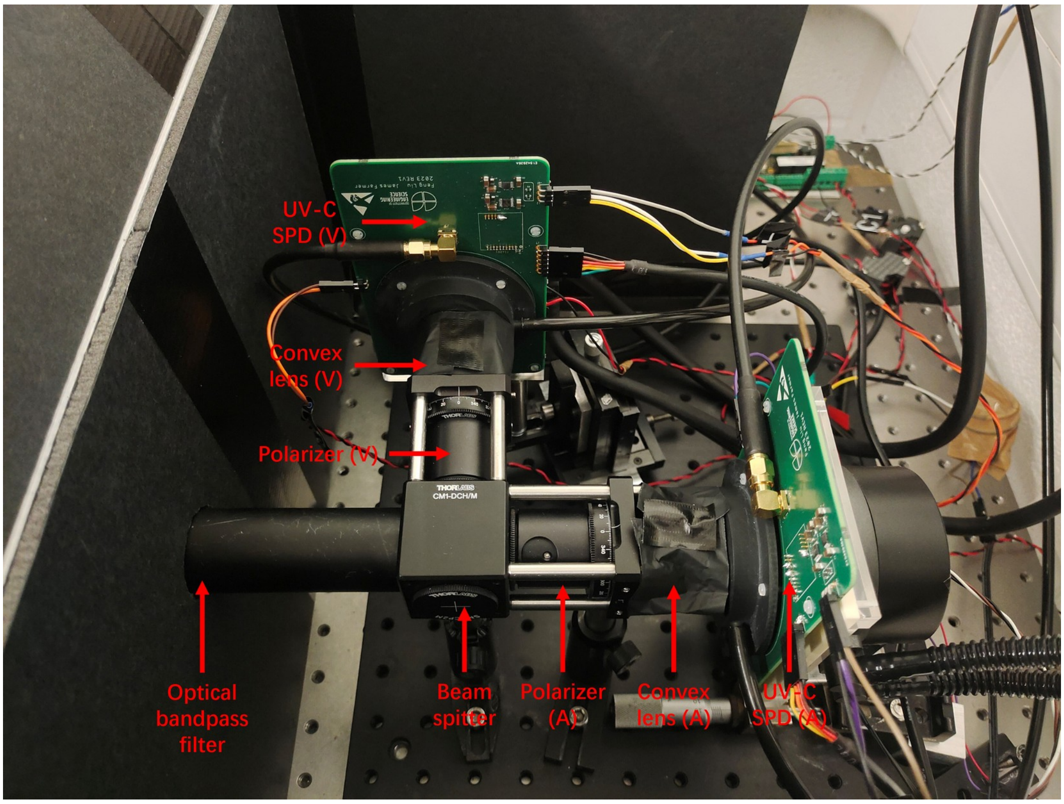

Figure 5.8 The experimental setup of the QKD receiver

Table 5.2 DCR of SPDs under different conditions

	DCR at 25℃	DCR at -15℃
SPD (A)	103.4 kcps	3 kcps
SPD (V)	110.5 kcps	2.9 kcps

5.5 UV-C WIRELESS B92 QKD DEMONSTRATION

At the transmitter, a PRBS sequence with a length of 4000 bits was generated by a PC and sent to the AWG. A bit “1” was used to generate a pulse to modulate the micro-LED corresponding to the (H) polarization and a bit “0” was used to generate a pulse to modulate the micro-LED corresponding to the (D) polarization. The pulse width was set as 2 ns to match the measured micro-LED’s E-O bandwidth of around 500 MHz. The average photon number per qubit was set as 0.1, and the transmitted repetition rate was varied from 100 MHz to 500 MHz. The corresponding transmitted power is shown in Table 5.3.

Table 5.3 Transmitted power versus repetition rate

Repetition rate	100 MHz	200 MHz	400 MHz	500 MHz
Transmitted power	7.1 pW	14.2 pW	28.4 pW	35.5 pW

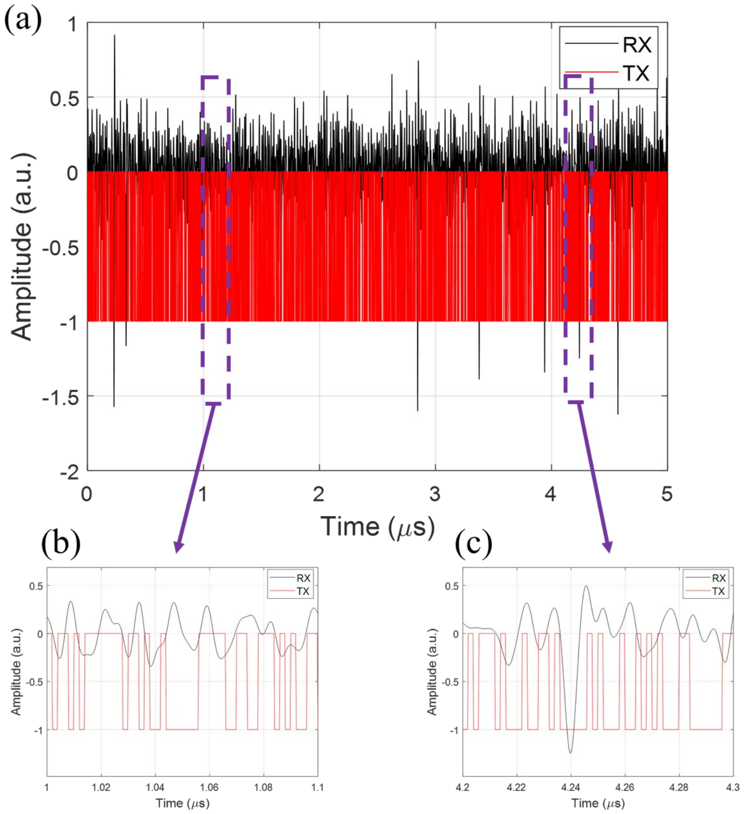

Figure 5.9 Synchronized received pulses (channel A) and the corresponding transmitted qubits (channel H)

At the receiver, the received pulses from the two UV-C SPDs were captured by an oscilloscope for post-processing using the CPP technique (see section 4.4.2). For the data from each UV-C SPD, the detection window was fixed at 2 ns and synchronization between transmitted sequence and received pulses was achieved by correlation. Fig. 5.9 (a) shows the synchronized received pulses (from channel A) and the corresponding transmitted PRBS sequence (from channel H) over a period of 1 μs for a pulse repetition rate of 500 MHz. The received pulses have been differentiated, following the differentiation process in the CPP procedure shown in Chapter 4. The values “-1” and “0” in the red line represent “1” and “0” in the transmitted sequences, respectively. The diagram shows very few qubits resulting in pulses detected by the receiver. This is due to the low probability of a photon being generated from each electrical pulse (0.1), the link loss (see section 5.2) and PDE (14.76 %). The left zoomed-in diagram (Fig. 5.9 (b)) shows no pulses generated in the receiver and the right zoomed-in one (Fig. 5.9 (c)) shows one pulse occurring at around 4.24 μs. The average peak amplitude of received pulses over this 5 μs duration (7 pulses) is approximately “-1.4”.

The peak amplitude of a single pulse is a little less than “-1” (see Fig. 5.9) and each detection window (2 ns) consists of 8 sampling points. The decision threshold was set as -8. If the values of each pulse summarized within a detection window are less than the threshold, the bit is set to “1”, otherwise “0”. If the corresponding two qubits obtained from two different UV-C SPDs are both “1”, the received bit is “1” for UV-C SPD (A) and “0” for UV-C SPD (V). Then, the received sequence is compared with the transmitted sequence to obtain the raw key (transmitter and receiver use the matched polarizations) and QBER. Finally, error correction and privacy amplification were undertaken theoretically to infer the SKR.

Table 5.4 Summary of raw key rate and QBER

Repetition rate	50 MHz	100 MHz	200 MHz	400 MHz	500 MHz
QBER (%)	0.38	0.37	0.77	1.56	1.76
Raw key rate	0.12135	0.24435	0.4357	1.0198	1.3405

For each repetition rate, 40000×50 qubits were transmitted and detected to obtain the raw key rate and QBER. Table 5.4 shows the measured raw key rate and QBER. The results show that the QBER is nearly unchanged with a repetition rate from 50 MHz to 100 MHz. Then, the QBER increases because of the emergence and growth of

ISI. Fig. 5.10 shows the number of raw keys/errors per 40000 transmitted qubits versus time. The results show the number of raw keys fluctuates at around 100 per 40000 qubits.

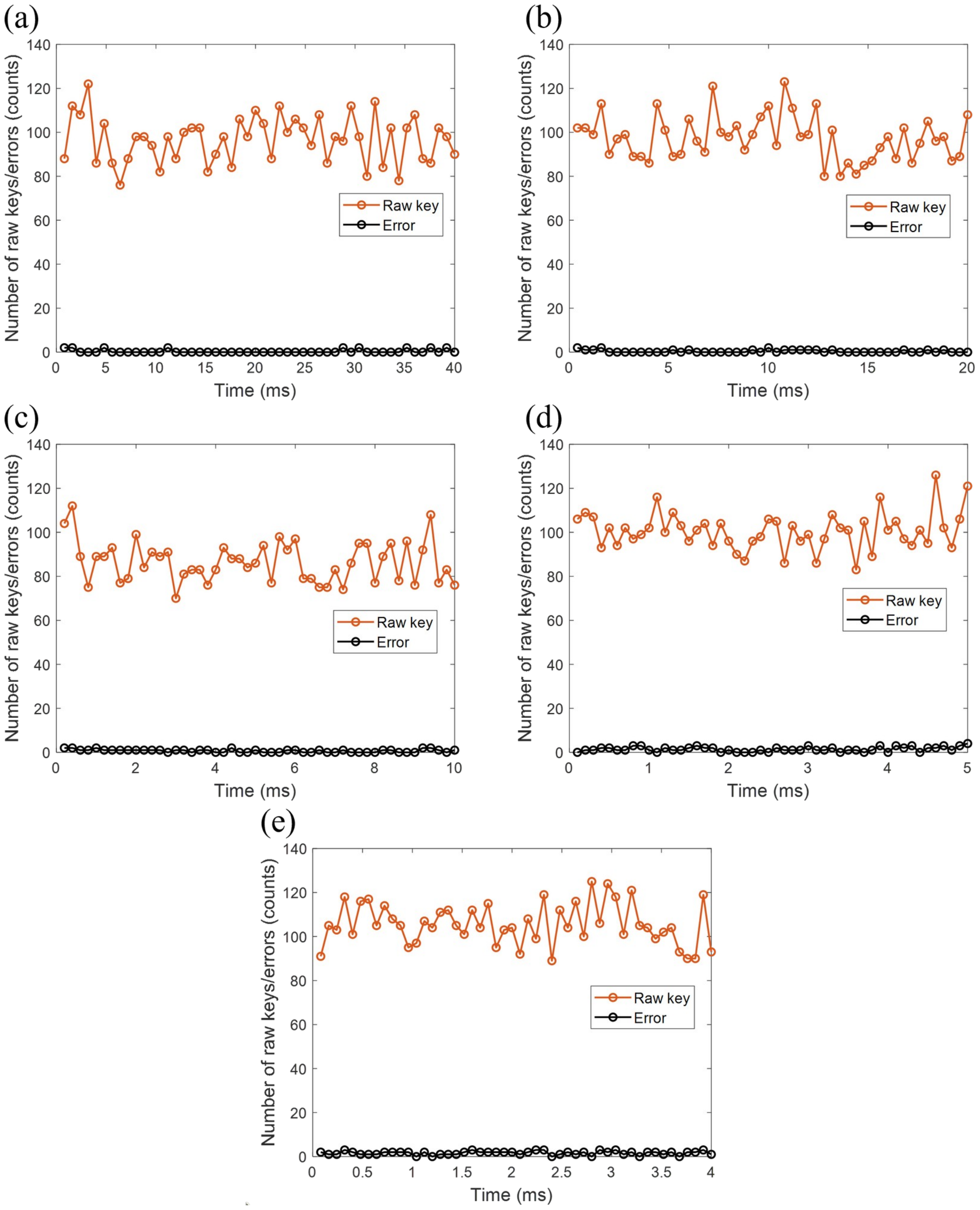

Figure 5.10 Number of raw keys/errors (per 40000 transmitted qubits) versus time with a repetition rate of (a) 50 MHz (b) 100 MHz (c) 200 MHz (d) 400 MHz (e) 500 MHz

Error correction and privacy amplification are carried out according to [181] through the classical channel. For error correction, redundant information is added to implement an efficient correction protocol. Based on the Shannon theorem [183], the ratio between the minimum number of redundant bits L_{EC} needed to correct a raw key of length L_{raw} is:

$$\frac{L_{EC}}{L_{raw}} = -E_\mu \log_2 E_\mu - (1-E_\mu)\log_2(1-E_\mu) \quad (5.14)$$

where E_μ is equal to QBER. However, Shannon's theorem is conditional on the infinite length of raw keys. To get close to the Shannon limit, a more efficient bidirectional code can be used [184], which uses $f(e)L_{EC}$ bits for error correction. Values of $f(e)$ that correspond to particular values of QBER are listed in Table 5.5.

Table 5.5 values of $f(e)$ taken from [184]

E_μ	$f(e)$
1%	1.16
5%	1.16
10%	1.22
15%	1.35

For privacy amplification, the corrected keys are shorted by using hash functions to remove the effect of eavesdroppers [181, 185]. The proportion that the corrected keys need to be shorted L_{PA}/L_{raw} is given by:

$$\frac{L_{PA}}{L_{raw}} = \begin{cases} \log_2\left(1+4E_\mu - 4E_\mu^2\right) for\ E_\mu \leq 1/2 \\ 1\ for\ E_\mu > 1/2 \end{cases} \quad (5.15)$$

Thus, the SKR is calculated as:

$$SKR = L_{raw} - L_{EC} - L_{PA} \quad (5.16)$$

Table 5.6 presents the SKR versus repetition rate. The results show that the SKR increases with the repetition rate, and the maximum value achieved is 1.0127 Mbit/s, with a repetition rate of 500 MHz. The QBER and SKR versus repetition rate are shown in Fig. 5.11.

Table 5.6 SKR versus repetition rate

Repetition Rate	50 MHz	100 MHz	200 MHz	400 MHz	500 MHz
SKR (Mbit/s)	0.11373	0.22937	0.38374	0.79444	1.0127

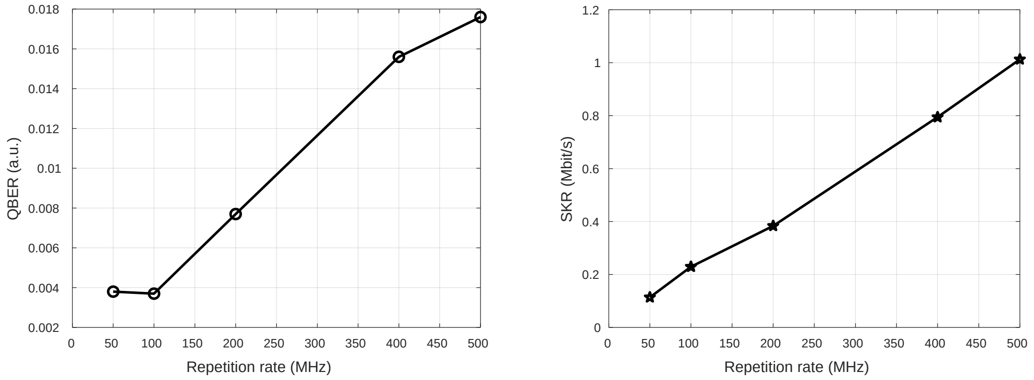

(a) (b)

Figure 5.11 UV-C B92 QKD performance under different repetition rate (a) QBER versus repetition rate (b) SKR versus repetition rate

5.6 RESISTANCE TO AMBIENT LIGHT

These results show that the link functions well with no ambient light incident on the detector. In this section, the influence of ambient light on the system performance will be assessed.

The major sources of ambient light are artificial lighting and sunlight. Most artificial lighting uses white LEDs (or is likely to use them in the future), so it is essential to evaluate the use of the QKD system under such illumination. In this work, the white LED-based ambient light is provided by the artificial lighting in the laboratory where experiments are conducted. The characterization of this LED’s light is presented first below.

The spectrum of LED-based ambient light at the input of the QKD receiver was measured by the optical spectrum analyzer (Ocean Insight OFX00951). This is calibrated using a cosine corrector provided by the manufacturer to measure the irradiance. The analyzer input fibre was positioned horizontally to align with the orientation of the QKD receiver. The LED light was turned up to the maximum brightness, and the measured LED-based ambient light spectrum is shown in Fig. 5.12. The result shows the spectrum ranges from ~400 nm to ~800 nm, and the total horizontal irradiance is $87.4\,mW/m^2$.

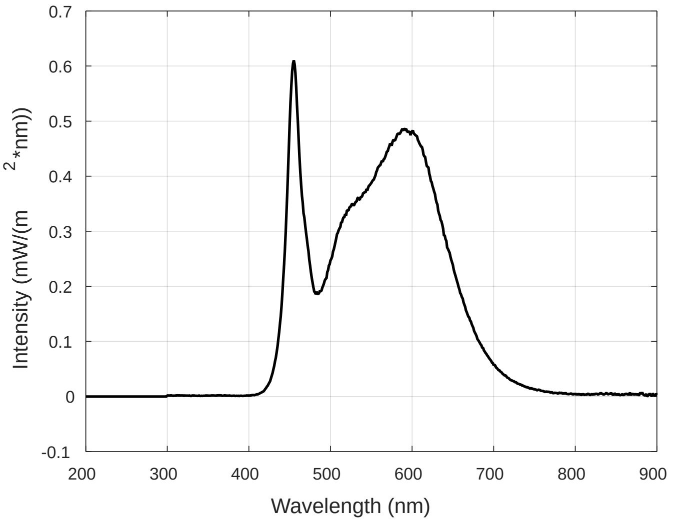

Figure 5.12 Optical spectrum of the ambient light from LED lighting

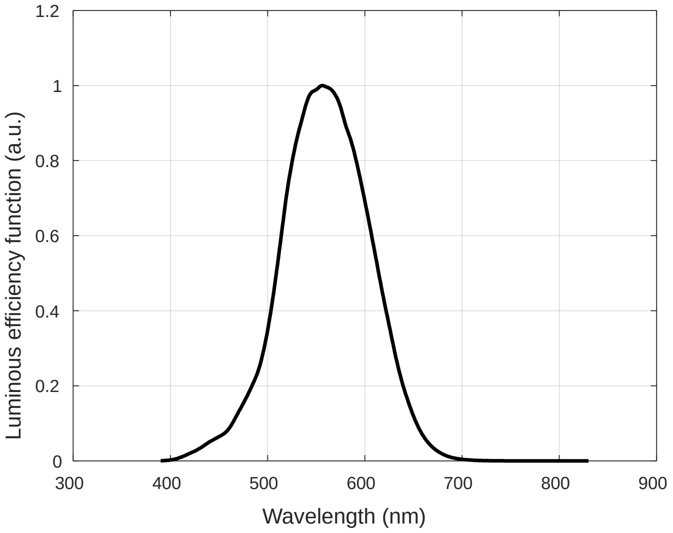

Figure 5.13 Luminous efficiency function [186]

Additionally, the illuminance is calculated based on the Commission Internationale de I’Eclariage (CIE) photopic luminosity function [187, 188]. The CIE 2008 curve (see Fig. 5.13) defines the luminous efficiency function, considering light ranging from 390 nm to 830 nm [186].

Based on the CIE 2008 curve, the illuminance can be obtained from irradiance:

$$Illuminance = K \int_{390}^{830} V(\lambda) E(\lambda) d\lambda \quad (5.17)$$

where $V(\lambda)$ is the light irradiance and $E(\lambda)$ is the luminous efficiency function. K is $683\,lm/W$, representing the human eye's ability to perceive color. Thus, the horizontal illuminance of the LED at the input of the QKD receiver is calculated to be 29.8 lux at maximum brightness. In order to verify this, an illuminance meter (Light Meter

DT-1308) was used to measure the horizontal illuminance at the input of the QKD receiver. The measured illuminance was 22 lux, which is lower than the estimated 29.8 lux.

Once the irradiance and luminance from the LED were determined, the QKD link was operated whilst varying this ambient illumination. The horizontal irradiance of the LED-based ambient light at the input of the QKD receiver was varied from $4.37\, mW/m^2$ to $87.4\, mW/m^2$. Other parameters are the same as those used in section 5.5. The measured QBER and SKR versus irradiance at a repetition rate of 100 MHz and 500 MHz are shown in Fig. 5.14. Note that the QBER and SKR results with no LED illumination are obtained from Fig. 5.11. The results show the QBER increases linearly with irradiance following Eq. (5.7). The maximum QBER reaches 11.98 % and 13.83 % for 100 MHz and 500 MHz repetition rates, respectively. These two values already exceed the QKD threshold of 11 %. The SKR decreases as a consequence of the higher QBER. The irradiance resulting in a QBER of 11 % is $74.7\, mW/m^2$ and $61.3\, mW/m^2$ for 100 MHz and 500 MHz repetition rates.

The corresponding illuminance of the LED-based ambient light is calculated according to Eq. (5.17). The QBER versus illuminance is plotted in Fig. 5.15. The illuminance resulting in a QBER of 11 % is 25.5 lux and 20.9 lux for 100 MHz and 500 MHz repetition rates.

The LED light rejection of our QKD system is limited because the optical bandpass filter in the receiver can only block ambient light up to 600 nm, whereas the SiPM used in the UV-C SPD is sensitive up to 900 nm (see Fig. 4.4). Consequently, the ambient light in the 600-900 nm region contributes significant interference, leading to a high QBER.

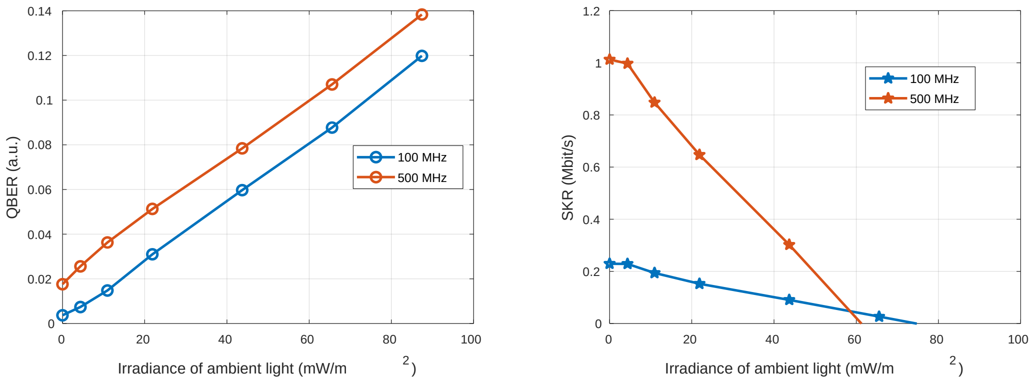

(a) (b)

Figure 5.14 UV-C B92 QKD performance under different irradiance of ambient light (a) QBER versus irradiance (b) SKR versus irradiance

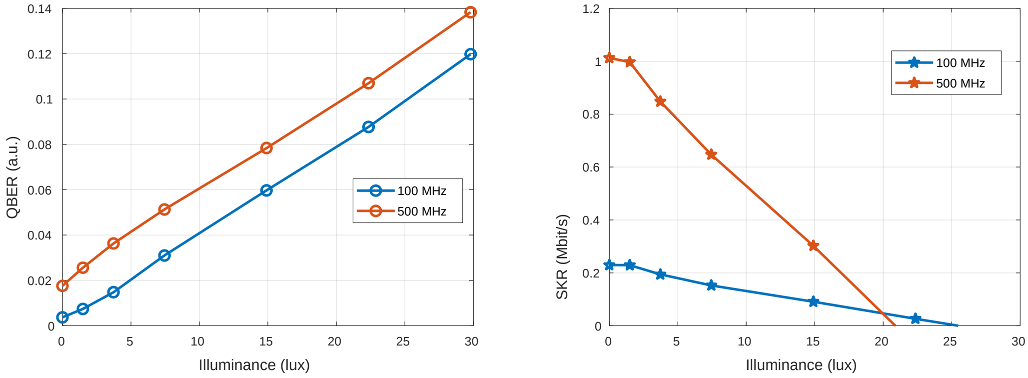

(a) (b)

Figure 5.15 UV-C B92 QKD performance under different illuminance of ambient light (a) QBER versus illuminance (b) SKR versus illuminance

5.7 Sunlight Interference Rejection Design

The LED light rejection performance of the QKD system was presented in Section 5.6. However, the spectrum of LED light (see Fig. 5.12) is different from the sunlight (see the ASTM 1.5 Spectra in Fig. 2.11). The illuminance of sunlight is 115650 lux, calculated based on the ASTM 1.5 Spectra and Eq. (5.17), while the LED in section 5.6 provides illuminance less than 100 lux. This means the

QKD link would be very likely to suffer much more severe interference from sunlight in outdoor applications.

A simulation was undertaken to estimate the ambient count rate caused by sunlight and LED light across the 200-900 nm spectrum. The ambient count rate is defined as the number of detection counts created by ambient light (sunlight or LED light) per second. The sunlight spectrum used was the ASTM 1.5 Spectra and the LED light spectrum was the same as that shown in Fig. 5.12, with an irradiance of $61.3 mW/m^2$ (corresponding to a QBER of 11 % at 500 MHz repetition rate in section 5.6).

The model and parameters in Fig. 5.1 and Table 5.1 are applied here, with the following modifications: (1) the operating wavelength is set to 280 nm; (2) the DCR is 3 kcps; (3) the PDE versus wavelength follows Fig.4.4; (4) Total transmission (see section 5.2) versus wavelength is obtained based on device datasheets (Table 5.7 shows device numbers).

Table 5.7 Optics and corresponding device numbers

Optical filter	Edmund 280 nm OD4 10 nm bandpass filter
Beam splitter	Thorlabs BSW20R
Polarizer	Thorlabs GLB10-UV
Convex lens	Thorlabs LA4052-UV
UV filter	Thorlabs FGUV5M

A plot of the simulated ambient count rate versus wavelength is shown in Fig. 5.16. The results show both sunlight and LED light create severe interference in the region from 650 nm to 900 nm, in the region where the SiPM is sensitive. The total ambient count rates created by the LED light and sunlight are 68.368 kcps and 6.529 Gcps, respectively. This means that the maximum tolerable ambient count rate is 68.368 kcps, while sunlight generates approximately 95,500 times this threshold ($6.529\,Gcps/68.368\,kcps$).

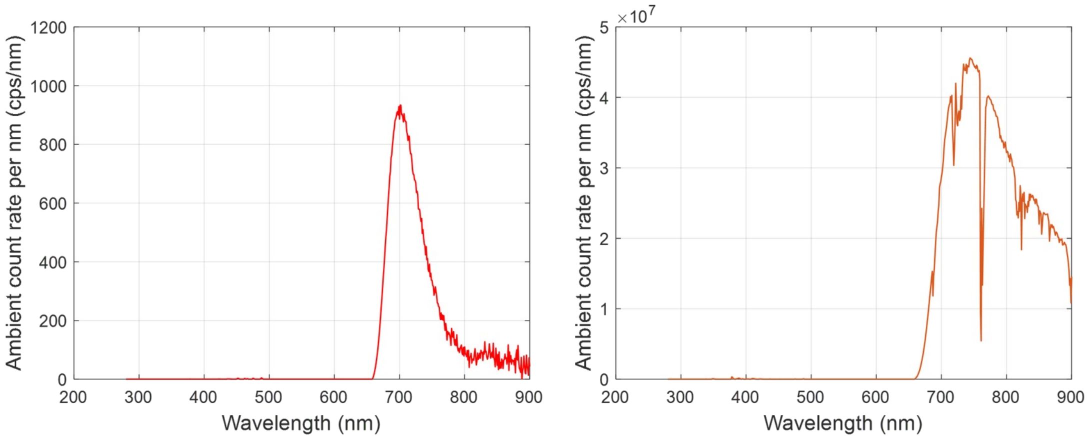

(a) (b)

Figure 5.16 Simulated ambient count rate versus wavelength (a) LED light (b) Sunlight

Therefore, to realize indoor applications at realistic light levels and outdoor applications exposed to sunlight, the interference between 650 nm and 900 nm must be mitigated. Using additional optical filters at the entrance of the receiver to further attenuate the ambient light is a potential approach. A total attenuation of OD ≥ 5 between 650 nm and 900 nm is needed. One potential solution is a short-pass filter, an example would be an ASAHI SPECTRA XUV0310. This filter can block light from 310 nm to 1000 nm with OD 4 attenuation, while the transmission between 270 nm and 310 nm is over 80 %.

The transmission of this filter versus wavelength was introduced into the simulation model. The simulation was conducted to examine the feasibility of using this short-pass filter. Fig. 5.17 shows the ambient count rate from sunlight versus wavelength with one or two short-pass filters. The result shows the total ambient count rate is 654.4 kcps with one short-pass filter. This is still higher than the maximum tolerable ambient count rate of 68.368 kcps. However, with two short-pass filters, the total ambient count rate is further reduced to 273 cps. Moreover, the corresponding QBER is calculated as 1.71 %. This shows the potential of our QKD system operating under sunlight conditions.

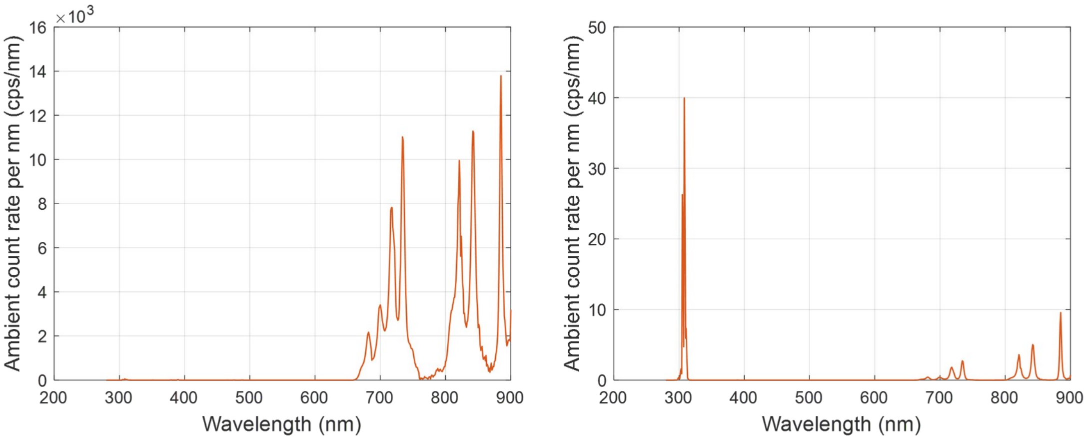

(a) (b)

Figure 5.17 Simulated ambient count rate versus wavelength with (a) one short-pass filter (b) two short-pass filters (ASAHI SPECTRA XUV0310)

5.8 CONCLUSIONS

This Chapter presents a UV-C short-range wireless B92 QKD system. To the best of our knowledge, this is the first record of a QKD system working in the UV-C region. A theoretical model of a B92 QKD system is described, and simulation results show the potential of a practical short-range wireless QKD system with an operating wavelength of less than 289 nm. Then, a practical B92 QKD transmitter and receiver are described and characterized. The UV-C wireless QKD links are demonstrated with a repetition rate from 50 MHz to 500 MHz. The QBER increases from 0.38 % to 1.76

%, and the inferred SKR increases from 113.73 kbit/s to 1.0127 Mbit/s. Additionally, the LED ambient light was characterized, and our QKD system can work at a maximum LED light irradiance of $74.7 mW/m^2$ and $61.3 mW/m^2$ for 100 MHz and 500 MHz repetition rates, respectively. These correspond to 25.5 lux and 20.9 lux respectively, which is lower than a normal indoor LED illuminance level of ~ 500 lux. Finally, a strategy of using short-pass filters to achieve sunlight rejection is proposed. An ambient count rate of 273 cps and a QBER of 1.71 % can be expected with two additional short-pass filters. Thus, our UV-C wireless QKD system has the potential to be robust to both sunlight and normal indoor LED light with the addition of short-pass filters.

Chapter 6:

Conclusions and Future Work

6.1 CONCLUSIONS

This thesis reports an in-depth investigation into UV-C communications. Given the challenges associated with OWC operating in the visible and near-infrared spectrum, this thesis focuses on exploiting the "solar blind" region within the UV-C spectrum. This region offers a unique opportunity due to its extremely low sunlight irradiance, which significantly reduces the impact of sunlight interference and enhances both the sensitivity and reliability of photon-counting communications. Three key contributions of this thesis are as follows.

- The development of two photon-counting receivers based on SiPMs (see Chapters 3 and 4). Unlike previously reported UV photon-counting receivers [128-132], one advantage of these two receivers is that they are designed based on commercial devices. The receiver in Chapter 3 features a cooled SiPM along with a separate amplification circuit. This receiver shows a PDE of 15.38 %, a DCR of 35 kcps and a bandwidth of 5 MHz. The receiver in Chapter 4 (UV-C SPD) integrates the cooled SiPM with the PCB. Compared with the receiver in Chapter 3, the UV-C SPD exhibits improved performance, including a DCR of 2.1 kcps and a bandwidth of 110 MHz. Its excellent UV-C sensitivity allows it to play a crucial role in quantum communication or conventional communication scenarios with significant link losses.

- The establishment of UV-C ultralow photon flux OWC links, including OOK links and PPM links (see Chapter 4). For OOK links, the maximum data rate achieved was 20 Mbit/s with a received photon number per bit of 30. In terms of PPM links, the maximum data rate reaches 120 Mbit/s, meeting eye safety standards. Additionally, a minimum transmitted photon number per bit of 7.7 was demonstrated in a 1 Mb/s 128-PPM link, marking the first reported Mbit/s-level UV-C wireless communication link operating with fewer than 10 transmitted photons per bit [189, 190]. The demonstration of these ultralow photon flux links explores the UV-C spectrum and provides a novel approach for exploring UV-C wireless communication scenarios facing significant link losses.

- The demonstration of what is, to the best of our knowledge, the first wireless QKD link operating in the UV-C region (see Chapter 5), which has the potential to be robust to ambient light. This provides a new solution for securing communications for mobile terminal devices. The QKD link infers a record SKR of over 1 Mbit/s based on the measured raw keys. The QKD system can tolerate at most levels of $74.7 mW/m^2$ (equal to 25.5 lux) white LED ambient light, and a design for rejecting sunlight and normal indoor LED light was also proposed and analysed.

6.2 FUTURE WORK

Ultralow photon flux OWC and QKD links operating in the UV-C region have been demonstrated in this thesis, using micro-LEDs and UV-C SPDs. However, further performance enhancements remain to be explored, particularly in achieving higher data rates and improved robustness to sunlight interference. Three potential future improvements are outlined below.

6.2.1 Higher-Speed Ultralow Photon Flux Links

The highest data rate of demonstrated ultralow photon flux links in this thesis is 120 Mbit/s, as detailed in Section 4.4.4, specifically with the 40 Mb/s 8-PPM link. The primary factors obstructing further enhancement of data rates include the bandwidth of the transmitter (UV-C micro-LED) and receiver (UV-C SPD). Several potential solutions are as follows.

For the transmitter, reducing the size of the micro-LED can further increase the modulation bandwidth. UV-C micro-LEDs with approximately 1 GHz bandwidth have been reported with a diameter of less than 40 µm [147].

For the receiver, the bandwidth of both SiPM and amplifier should be considered. Reducing the pixel size of the SiPM can improve its bandwidth. HAMAMATSU offers SiPMs with a pixel size of 25 µm, compared to the 50 µm pixel size used in the UV-C SPD. Moreover, Onsemi provides SiPMs with pixel sizes of 20 or 10 µm [133, 191]. The fast output of these SiPMs has a rise time of ~0.3 ns, corresponding to a bandwidth of over 1 GHz. The bandwidth of an amplifier depends on its GBWP, the SiPM's capacitance and the trans-impedance load according to Eq. 3.7. The 8 GHz GBWP of Texas OPA855-Q1 is currently the highest available in the market. The trans-impedance load must be large enough to allow single-photon pulses to be observed by commercial oscilloscopes. Thus, reducing the active area of the SiPM to decrease its capacitance is a feasible solution. In addition, the cascade amplifier design is another potential solution because of its easily achieved high bandwidth.

6.2.2 Sunlight Interference Rejection

In addition to the strategy using additional filters in section 5.7, another approach is to use a holographic grating and a slit to select the UV-C light to enter the QKD receiver. Due to the diffraction of the holographic grating, the light of different wavelengths will be reflected in different directions. A slit is then used to select the desired wavelengths to pass through to the QKD receiver. For our UV-C wireless QKD system, light ranging from 270 nm to 290 nm can be selected, while wavelengths exceeding 290 nm will be blocked. Compared with the strategy using additional filters, this approach increases the complexity of the QKD receiver but can fully eliminate ambient light interference from wavelengths outside the working range.

6.2.3 QKD Integrated with Tracking

The UV-C wireless B92 QKD system presented in this thesis is static. To enable terminal mobile applications, a tracking system should be integrated with the existing static wireless QKD system. Many studies have been conducted to combine QKD systems with tracking systems [61, 192-195]. A typical tracking system's structure uses two mirrors, which can be automatically adjusted to steer the signal beam from the transmitter towards the receiver. A practical tracking system is more complex, but ways to enhance this static link with approaches for mobile data links would be of value.

Bibliography

[1] Z. Ghassemlooy, S. Arnon, M. Uysal, Z. Xu, and J. Cheng, "Emerging Optical Wireless Communications-Advances and Challenges," *IEEE Journal on Selected Areas in Communications,* vol. 33, no. 9, pp. 1738–1749, 2015.

[2] D. O. Brien, R. Turnbull, H. L. Minh, G. Faulkner, O. Bouchet, P. Porcon, M. E. Tabach, E. Gueutier, M. Wolf, L. Grobe, and J. Li, "High-Speed Optical Wireless Demonstrators: Conclusions and Future Directions," *Journal of Lightwave Technology,* vol. 30, no. 13, pp. 2181–2187, 2012.

[3] M. Uysal and H. Nouri, "Optical wireless communications — An emerging technology," in *2014 16th International Conference on Transparent Optical Networks (ICTON)*, 6–10 July 2014 2014, pp. 1–7.

[4] H. Tataria, M. Shafi, A. F. Molisch, M. Dohler, H. Sjöland, and F. Tufvesson, "6G Wireless Systems: Vision, Requirements, Challenges, Insights, and Opportunities," *Proceedings of the IEEE,* vol. 109, no. 7, pp. 1166–1199, 2021.

[5] Y. Horst, B. I. Bitachon, L. Kulmer, J. Brun, T. Blatter, J.-M. Conan, A. Montmerle-Bonnefois, J. Montri, B. Sorrente, C. B. Lim, N. Védrenne, D. Matter, L. Pommarel, B. Baeuerle, and J. Leuthold, "Tbit/s line-rate satellite feeder links enabled by coherent modulation and full-adaptive optics," *Light: Science & Applications,* vol. 12, no. 1, p. 153, 2023/06/20 2023.

[6] L.-Y. Wei, S.-I. Chen, C.-H. Yeh, Y. Liu, G.-H. Chen, C.-W. Peng, W. H. Gunawan, Y.-H. Chang, P.-C. Guo, and C.-W. Chow, "2.333-Tbit/s bi-directional optical mobile networks using optical wireless communication (OWC)," *Optics Communications,* vol.

475, p. 126187, 2020/11/15/ 2020.

[7] A. Schreier, O. Alia, R. Wang, R. Singh, G. Faulkner, G. Kanellos, R. Nejabati, D. Simeonidou, J. Rarity, and D. O. Brien, "Coexistence of Quantum and 1.6 Tbit/s Classical Data Over Fibre-Wireless-Fibre Terminals," *Journal of Lightwave Technology,* pp. 1–7, 2023.

[8] H. Huang, G. Xie, Y. Yan, N. Ahmed, Y. Ren, Y. Yue, D. Rogawski, M. J. Willner, B. I. Erkmen, K. M. Birnbaum, S. J. Dolinar, M. P. J. Lavery, M. J. Padgett, M. Tur, and A. E. Willner, "100 Tbit/s free-space data link enabled by three-dimensional multiplexing of orbital angular momentum, polarization, and wavelength," *Optics Letters,* vol. 39, no. 2, pp. 197–200, 2014/01/15 2014.

[9] C. Weedbrook, S. Pirandola, R. García-Patrón, N. J. Cerf, T. C. Ralph, J. H. Shapiro, and S. Lloyd, "Gaussian quantum information," *Reviews of Modern Physics,* vol. 84, no. 2, pp. 621–669, 05/01/ 2012.

[10] A. Lvovsky, *Quantum Physics: An Introduction Based on Photons*. Springer, 2018.

[11] R. L. Rivest, A. Shamir, and L. Adleman, "A method for obtaining digital signatures and public-key cryptosystems," *Commun. ACM,* vol. 26, no. 1, pp. 96–99, 1983.

[12] N. Koblitz, "Elliptic curve cryptosystems," *Mathematics of computation,* vol. 48, no. 177, pp. 203–209, 1987.

[13] W. Diffie and M. Hellman, "New directions in cryptography," *IEEE Transactions on Information Theory,* vol. 22, no. 6, pp. 644–654, 1976.

[14] K. A. G. Fisher, A. Broadbent, L. K. Shalm, Z. Yan, J. Lavoie, R. Prevedel, T. Jennewein, and K. J. Resch, "Quantum computing on encrypted data," *Nature Communications,* vol. 5, no. 1, p.

3074, 2014/01/21 2014.

[15] Y. Cao, Y. Zhao, X. Yu, and Y. Wu, "Resource assignment strategy in optical networks integrated with quantum key distribution," *Journal of Optical Communications and Networking,* vol. 9, no. 11, pp. 995–1004, 2017.

[16] S. Debnath, N. M. Linke, C. Figgatt, K. A. Landsman, K. Wright, and C. Monroe, "Demonstration of a small programmable quantum computer with atomic qubits," *Nature,* vol. 536, no. 7614, pp. 63–66, 2016/08/01 2016.

[17] M. Caleffi, D. Chandra, D. Cuomo, S. Hassanpour, and A. S. Cacciapuoti, "The Rise of the Quantum Internet," *Computer,* vol. 53, no. 6, pp. 67–72, 2020.

[18] D. Cuomo, M. Caleffi, and A. S. Cacciapuoti, "Towards a distributed quantum computing ecosystem," *IET Quantum Communication,* vol. 1, no. 1, pp. 3–8, 2020.

[19] A. S. Cacciapuoti, M. Caleffi, R. V. Meter, and L. Hanzo, "When Entanglement Meets Classical Communications: Quantum Teleportation for the Quantum Internet," *IEEE Transactions on Communications,* vol. 68, no. 6, pp. 3808–3833, 2020.

[20] P. W. Shor, "Algorithms for quantum computation: discrete logarithms and factoring," in *Proceedings 35th annual symposium on foundations of computer science*, 1994: Ieee, pp. 124–134.

[21] N. Gisin, G. Ribordy, W. Tittel, and H. Zbinden, "Quantum cryptography," *Reviews of Modern Physics,* vol. 74, no. 1, pp. 145–195, 03/08/ 2002.

[22] P. Sharma, A. Agrawal, V. Bhatia, S. Prakash, and A. K. Mishra, "Quantum Key Distribution Secured Optical Networks: A Survey," *IEEE Open Journal of the Communications Society,*

vol. 2, pp. 2049–2083, 2021.

[23] C. H. Bennett and G. Brassard, "Quantum cryptography: Public key distribution and coin tossing," *Theoretical Computer Science,* vol. 560, pp. 7–11, 2014/12/04/ 2014.

[24] C. H. Bennett, G. Brassard, C. Crépeau, R. Jozsa, A. Peres, and W. K. Wootters, "Teleporting an unknown quantum state via dual classical and Einstein-Podolsky-Rosen channels," *Physical Review Letters,* vol. 70, no. 13, pp. 1895–1899, 03/29/ 1993.

[25] D. J. Bernstein, "Post-quantum cryptography," in *Encyclopedia of Cryptography, Security and Privacy*: Springer, 2025, pp. 1846–1847.

[26] D. Joseph, R. Misoczki, M. Manzano, J. Tricot, F. D. Pinuaga, O. Lacombe, S. Leichenauer, J. Hidary, P. Venables, and R. Hansen, "Transitioning organizations to post-quantum cryptography," *Nature,* vol. 605, no. 7909, pp. 237–243, 2022.

[27] O. Regev, "On lattices, learning with errors, random linear codes, and cryptography," *Journal of the ACM (JACM),* vol. 56, no. 6, pp. 1–40, 2009.

[28] W. Heisenberg, Eckhart, and Hoyt, *The Physical Principles of the Quantum Theory*. New York, UNITED STATES: Dover Publications, 1949.

[29] C. A. Fuchs and A. Peres, "Quantum-state disturbance versus information gain: Uncertainty relations for quantum information," *Physical Review A,* vol. 53, no. 4, pp. 2038–2045, 04/01/ 1996.

[30] W. K. Wootters and W. H. Zurek, "A single quantum cannot be cloned," *Nature,* vol. 299, no. 5886, pp. 802–803, 1982/10/01 1982.

[31] D. Dieks, "Communication by EPR devices," *Physics Letters A,*

vol. 92, no. 6, pp. 271–272, 1982/11/22/ 1982.

[32] N. J. Cerf and S. Iblisdir, "Optimal N-to-M cloning of conjugate quantum variables," *Physical Review A,* vol. 62, no. 4, p. 040301, 09/18/ 2000.

[33] F. Grosshans and P. Grangier, "Quantum cloning and teleportation criteria for continuous quantum variables," *Physical Review A,* vol. 64, no. 1, p. 010301, 06/12/ 2001.

[34] H.-K. Lo and H. F. Chau, "Unconditional Security of Quantum Key Distribution Over Arbitrarily Long Distances," *Science,* vol. 283, no. 5410, pp. 2050–2056, 1999. [Online]. Available: http://ezproxy-prd.bodleian.ox.ac.uk:2154/stable/2896688.

[35] J. Bos, L. Ducas, E. Kiltz, T. Lepoint, V. Lyubashevsky, J. M. Schanck, P. Schwabe, G. Seiler, and D. Stehlé, "CRYSTALS-Kyber: a CCA-secure module-lattice-based KEM," in *2018 IEEE European symposium on security and privacy (EuroS&P)*, 2018: IEEE, pp. 353–367.

[36] R. Overbeck and N. Sendrier, "Code-based cryptography," in *Post-quantum cryptography*: Springer, 2009, pp. 95–145.

[37] D. J. Bernstein, D. Hopwood, A. Hülsing, T. Lange, R. Niederhagen, L. Papachristodoulou, M. Schneider, P. Schwabe, and Z. Wilcox-O'Hearn, "SPHINCS: practical stateless hash-based signatures," in *Annual international conference on the theory and applications of cryptographic techniques*, 2015: Springer, pp. 368–397.

[38] J. Ding and D. Schmidt, "Rainbow, a new multivariable polynomial signature scheme," in *International conference on applied cryptography and network security*, 2005: Springer, pp. 164–175.

[39] F. Grosshans and P. Grangier, "Continuous Variable Quantum

Cryptography Using Coherent States," *Physical Review Letters,* vol. 88, no. 5, p. 057902, 01/16/ 2002.

[40] C. Jiang, X.-L. Hu, Z.-W. Yu, and X.-B. Wang, "Measurement-device-independent quantum key distribution protocol with phase post-selection," *Photon. Res.,* vol. 10, no. 7, pp. 1703–1711, 2022/07/01 2022.

[41] M. Lucamarini, Z. L. Yuan, J. F. Dynes, and A. J. Shields, "Overcoming the rate–distance limit of quantum key distribution without quantum repeaters," *Nature,* vol. 557, no. 7705, pp. 400–403, 2018/05/01 2018.

[42] Y. Liu, W.-J. Zhang, C. Jiang, J.-P. Chen, C. Zhang, W.-X. Pan, D. Ma, H. Dong, J.-M. Xiong, C.-J. Zhang, H. Li, R.-C. Wang, J. Wu, T.-Y. Chen, L. You, X.-B. Wang, Q. Zhang, and J.-W. Pan, "Experimental Twin-Field Quantum Key Distribution over 1000 km Fiber Distance," *Physical Review Letters,* vol. 130, no. 21, p. 210801, 05/25/ 2023.

[43] W. Li, L. Zhang, H. Tan, Y. Lu, S.-K. Liao, J. Huang, H. Li, Z. Wang, H.-K. Mao, B. Yan, Q. Li, Y. Liu, Q. Zhang, C.-Z. Peng, L. You, F. Xu, and J.-W. Pan, "High-rate quantum key distribution exceeding 110 Mb/s–1," *Nature Photonics,* vol. 17, no. 5, pp. 416–421, 2023/05/01 2023.

[44] J. Yin, Y. Cao, Y.-H. Li, S.-K. Liao, L. Zhang, J.-G. Ren, W.-Q. Cai, W.-Y. Liu, B. Li, H. Dai, G.-B. Li, Q.-M. Lu, Y.-H. Gong, Y. Xu, S.-L. Li, F.-Z. Li, Y.-Y. Yin, Z.-Q. Jiang, M. Li, J.-J. Jia, G. Ren, D. He, Y.-L. Zhou, X.-X. Zhang, N. Wang, X. Chang, Z.-C. Zhu, N.-L. Liu, Y.-A. Chen, C.-Y. Lu, R. Shu, C.-Z. Peng, J.-Y. Wang, and J.-W. Pan, "Satellite-based entanglement distribution over 1200 kilometers," *Science,* vol. 356, no. 6343, pp. 1140–1144, 2017.

[45] S.-K. Liao, W.-Q. Cai, W.-Y. Liu, L. Zhang, Y. Li, J.-G. Ren, J. Yin,

Q. Shen, Y. Cao, Z.-P. Li, F.-Z. Li, X.-W. Chen, L.-H. Sun, J.-J. Jia, J.-C. Wu, X.-J. Jiang, J.-F. Wang, Y.-M. Huang, Q. Wang, Y.-L. Zhou, L. Deng, T. Xi, L. Ma, T. Hu, Q. Zhang, Y.-A. Chen, N.-L. Liu, X.-B. Wang, Z.-C. Zhu, C.-Y. Lu, R. Shu, C.-Z. Peng, J.-Y. Wang, and J.-W. Pan, "Satellite-to-ground quantum key distribution," *Nature,* vol. 549, no. 7670, pp. 43–47, 2017/09/01 2017.

[46] H. Chun, I. Choi, G. Faulkner, L. Clarke, B. Barber, G. George, C. Capon, A. Niskanen, J. Wabnig, D. O’Brien, and D. Bitauld, "Handheld free space quantum key distribution with dynamic motion compensation," *Opt. Express,* vol. 25, no. 6, pp. 6784–6795, 2017/03/20 2017.

[47] D. Lowndes, S. Frick, A. Hart, and J. Rarity, "A low cost, short range quantum key distribution system," *EPJ Quantum Technology,* vol. 8, no. 1, p. 15, 2021/05/26 2021.

[48] A. Tello Castillo, E. Eso, and R. Donaldson, "In-lab demonstration of coherent one-way protocol over free space with turbulence simulation," *Opt. Express,* vol. 30, no. 7, pp. 11671–11683, 2022/03/28 2022.

[49] X.-T. Zheng, Q.-F. Zhang, J.-y. Han, J. Ling, G.-c. Guo, and Z.-F. Han, "Experimental realization of free-space continuous-variable quantum key distribution based on fiber Sagnac interferometer," *Optics Letters,* vol. 48, no. 18, pp. 4837–4840, 2023/09/15 2023.

[50] A. T. Castillo, U. Zanforlin, G. S. Buller, and R. J. Donaldson, "Experimental demonstration of a reconfigurable free-space receiver implementing polarization routing and filtering for daytime quantum key distribution," *Opt. Express,* vol. 31, no. 24, pp. 40317–40327, 2023/11/20 2023.

[51] "Reference Air Mass 1.5 Spectra." NREL. [Online]. Available: https://www.nrel.gov/grid/solar-resource/spectra-am1.5.html.

[52] F. Liu, J. Farmer, A. Schreier, G. Faulkner, H. Chun, W. Matthews, Z. Wang, and D. O'Brien, "Ultra-sensitive UV solar-blind optical wireless communications with an SiPM," *Optics Letters,* vol. 48, no. 20, pp. 5387–5390, 2023/10/15 2023.

[53] F. Liu, J. Farmer, G. Faulkner, Z. Wang, J. Wang, D. O. Brien, E. Xie, J. Hill, J. Herrnsdorf, J. J. D. McKendry, and M. D. Dawson, "10 Mbit/s UV Solar-Blind OWC at 30 Photons Per Bit," in *2024 Conference on Lasers and Electro-Optics (CLEO)*, 5–10 May 2024 2024, pp. 1–2.

[54] F. Liu, J. Farmer, G. Faulkner, J. J. D. McKendry, E. Xie, Q. Zheng, Z. Wang, J. Wang, J. Hill, J. Herrnsdorf, M. D. Dawson, and D. O'Brien, "Ultralow Photon Flux OWC Links Using UV-C Single-Photon Detection," *Laser & Photonics Reviews,* vol. n/a, no. n/a, p. 2401804, 2025.

[55] X. Ma, P. Zeng, and H. Zhou, "Phase-Matching Quantum Key Distribution," *Physical Review X,* vol. 8, no. 3, p. 031043, 08/16/ 2018.

[56] Z. Wang, R. Malaney, and B. Burnett, "Satellite-To-Earth Quantum Key Distribution via Orbital Angular Momentum," *Physical Review Applied,* vol. 14, no. 6, p. 064031, 12/09/ 2020.

[57] F. Xu, X. Ma, Q. Zhang, H.-K. Lo, and J.-W. Pan, "Secure quantum key distribution with realistic devices," *Reviews of modern physics,* vol. 92, no. 2, p. 025002, 2020.

[58] T. Ferreira da Silva, G. B. Xavier, G. P. Temporão, and J. P. von der Weid, "Impact of Raman scattered noise from multiple telecom channels on fiber-optic quantum key distribution

systems," *Journal of lightwave technology,* vol. 32, no. 13, pp. 2332–2339, 2014.

[59] L.-J. Wang, K.-H. Zou, W. Sun, Y. Mao, Y.-X. Zhu, H.-L. Yin, Q. Chen, Y. Zhao, F. Zhang, and T.-Y. Chen, "Long-distance copropagation of quantum key distribution and terabit classical optical data channels," *Physical Review A,* vol. 95, no. 1, p. 012301, 2017.

[60] V. Lee and D. O'Brien, "Indoor Optical Wireless Communications using Quantum Key Distribution at 1370 nm," in *2020 IEEE Photonics Conference (IPC)*, 28 Sept.–1 Oct. 2020 2020, pp. 1–2.

[61] D. O. Brien, A. Schreier, and V. Lee, "Building a quantum wireless network," in *49th European Conference on Optical Communications (ECOC 2023)*, 1–5 Oct. 2023 2023, vol. 2023, pp. 1547–1550.

[62] M. Ghalaii and S. Pirandola, "Quantum communications in a moderate-to-strong turbulent space," *Communications Physics,* vol. 5, no. 1, p. 38, 2022.

[63] L. O. Mailloux, M. R. Grimaila, D. D. Hodson, G. Baumgartner, and C. McLaughlin, "Performance Evaluations of Quantum Key Distribution System Architectures," *IEEE Security & Privacy,* vol. 13, no. 1, pp. 30–40, 2015.

[64] E. Kiktenko, A. Trushechkin, Y. Kurochkin, and A. Fedorov, "Post-processing procedure for industrial quantum key distribution systems," *Journal of Physics: Conference Series,* vol. 741, p. 012081, 2016/08 2016.

[65] D. Elkouss, J. Martinez-Mateo, and V. Martin, "Information reconciliation for quantum key distribution," *arXiv preprint arXiv:1007.1616,* 2010.

[66] G. Brassard and L. Salvail, "Secret-key reconciliation by public discussion," in *Workshop on the Theory and Application of of Cryptographic Techniques*, 1993: Springer, pp. 410–423.

[67] D. Elkouss, J. Martinez, D. Lancho, and V. Martin, "Rate compatible protocol for information reconciliation: An application to QKD," in *2010 IEEE Information Theory Workshop on Information Theory (ITW 2010, Cairo)*, 2010: IEEE, pp. 1–5.

[68] C.-H. F. Fung, X. Ma, and H. Chau, "Practical issues in quantum-key-distribution postprocessing," *Physical Review A,* vol. 81, no. 1, p. 012318, 2010.

[69] R. Konig and R. Renner, "Sampling of Min-Entropy Relative to Quantum Knowledge," *IEEE Transactions on Information Theory,* vol. 57, no. 7, pp. 4760–4787, 2011.

[70] R. Wolf, *Quantum Key Distribution: An Introduction with Exercises*. Springer Nature, 2021.

[71] J. Kilian, *Theory of cryptography*. Springer, 2005.

[72] V. Scarani and R. Renner, "Quantum Cryptography with Finite Resources: Unconditional Security Bound for Discrete-Variable Protocols with One-Way Postprocessing," *Physical Review Letters,* vol. 100, no. 20, p. 200501, 05/22/ 2008.

[73] R. Y. Q. Cai and V. Scarani, "Finite-key analysis for practical implementations of quantum key distribution," *New Journal of Physics,* vol. 11, no. 4, p. 045024, 2009/04/30 2009.

[74] A. Leverrier, F. Grosshans, and P. Grangier, "Finite-size analysis of a continuous-variable quantum key distribution," *Physical Review A,* vol. 81, no. 6, p. 062343, 06/28/ 2010.

[75] H. Weier, H. Krauss, M. Rau, M. Fürst, S. Nauerth, and H. Weinfurter, "Quantum eavesdropping without interception: an

attack exploiting the dead time of single-photon detectors," *New Journal of Physics,* vol. 13, no. 7, p. 073024, 2011/07/15 2011.

[76] Y.-L. Tang, H.-L. Yin, X. Ma, C.-H. F. Fung, Y. Liu, H.-L. Yong, T.-Y. Chen, C.-Z. Peng, Z.-B. Chen, and J.-W. Pan, "Source attack of decoy-state quantum key distribution using phase information," *Physical Review A,* vol. 88, no. 2, p. 022308, 08/08/ 2013.

[77] V. Scarani, A. Acín, G. Ribordy, and N. Gisin, "Quantum Cryptography Protocols Robust against Photon Number Splitting Attacks for Weak Laser Pulse Implementations," *Physical Review Letters,* vol. 92, no. 5, p. 057901, 02/06/ 2004.

[78] W.-Y. Hwang, "Quantum Key Distribution with High Loss: Toward Global Secure Communication," *Physical Review Letters,* vol. 91, no. 5, p. 057901, 08/01/ 2003.

[79] H.-K. Lo, X. Ma, and K. Chen, "Decoy State Quantum Key Distribution," *Physical Review Letters,* vol. 94, no. 23, p. 230504, 06/16/ 2005.

[80] C. Gobby, Z. L. Yuan, and A. J. Shields, "Quantum key distribution over 122 km of standard telecom fiber," *Applied Physics Letters,* vol. 84, no. 19, pp. 3762–3764, 2004/05/10 2004.

[81] B. Fröhlich, J. F. Dynes, M. Lucamarini, A. W. Sharpe, Z. Yuan, and A. J. Shields, "A quantum access network," *Nature,* vol. 501, no. 7465, pp. 69–72, 2013/09/01 2013.

[82] J. F. Dynes, W. W. S. Tam, A. Plews, B. Fröhlich, A. W. Sharpe, M. Lucamarini, Z. Yuan, C. Radig, A. Straw, T. Edwards, and A. J. Shields, "Ultra-high bandwidth quantum secured data

transmission," *Scientific Reports,* vol. 6, no. 1, p. 35149, 2016/10/13 2016.

[83] A. Boaron, G. Boso, D. Rusca, C. Vulliez, C. Autebert, M. Caloz, M. Perrenoud, G. Gras, F. Bussières, M.-J. Li, D. Nolan, A. Martin, and H. Zbinden, "Secure Quantum Key Distribution over 421 km of Optical Fiber," *Physical Review Letters,* vol. 121, no. 19, p. 190502, 11/05/ 2018.

[84] C.-X. Zhu, Z.-Y. Chen, Y. Li, X.-Z. Wang, C.-Z. Wang, Y.-L. Zhu, F.-T. Liang, W.-Q. Cai, G. Jin, S.-K. Liao, and C.-Z. Peng, "Experimental Quantum Key Distribution with Integrated Silicon Photonics and Electronics," *Physical Review Applied,* vol. 17, no. 6, p. 064034, 06/16/ 2022.

[85] F. Beutel, F. Brückerhoff-Plückelmann, H. Gehring, V. Kovalyuk, P. Zolotov, G. Goltsman, and W. H. P. Pernice, "Fully integrated four-channel wavelength-division multiplexed QKD receiver," *Optica,* vol. 9, no. 10, pp. 1121–1130, 2022/10/20 2022.

[86] F. Grünenfelder, A. Boaron, G. V. Resta, M. Perrenoud, D. Rusca, C. Barreiro, R. Houlmann, R. Sax, L. Stasi, S. El-Khoury, E. Hänggi, N. Bosshard, F. Bussières, and H. Zbinden, "Fast single-photon detectors and real-time key distillation enable high secret-key-rate quantum key distribution systems," *Nature Photonics,* vol. 17, no. 5, pp. 422–426, 2023/05/01 2023.

[87] J. A. Dolphin, T. K. Paraiso, H. Du, R. I. Woodward, D. G. Marangon, and A. J. Shields, "A Hybrid Integrated Quantum Key Distribution Transceiver Chip," *arXiv preprint arXiv:2308.02238,* 2023.

[88] A. Ruiz Alba Gaya, D. Calvo Díaz-Aldagalán, V. García Muñoz, A. Martínez García, W. A. Amaya Ocampo, J. G. ROZO CHICUE,

J. Mora Almerich, and J. Capmany Francoy, "Practical quantum key distribution based on the BB84 protocol," in *Waves*, 2011, vol. 1, no. 3: Instituto de Telecomunicaciones y Aplicaciones Multimedia (iTEAM), pp. 4–14.

[89] P. D. Townsend, "Quantum Cryptography on Optical Fiber Networks," *Optical Fiber Technology,* vol. 4, no. 4, pp. 345–370, 1998/10/01/ 1998.

[90] C. H. Bennett, "Quantum cryptography using any two nonorthogonal states," *Physical review letters,* vol. 68, no. 21, p. 3121, 1992.

[91] D. Bruß, "Optimal Eavesdropping in Quantum Cryptography with Six States," *Physical Review Letters,* vol. 81, no. 14, pp. 3018–3021, 10/05/ 1998.

[92] H. Bechmann-Pasquinucci and N. Gisin, "Incoherent and coherent eavesdropping in the six-state protocol of quantum cryptography," *Physical Review A,* vol. 59, no. 6, pp. 4238–4248, 06/01/ 1999.

[93] G. Brassard, N. Lütkenhaus, T. Mor, and B. C. Sanders, "Limitations on Practical Quantum Cryptography," *Physical Review Letters,* vol. 85, no. 6, pp. 1330–1333, 08/07/ 2000.

[94] A. Acín, N. Gisin, and V. Scarani, "Coherent-pulse implementations of quantum cryptography protocols resistant to photon-number-splitting attacks," *Physical Review A,* vol. 69, no. 1, p. 012309, 01/15/ 2004.

[95] M. Mubashir Khan, M. Murphy, and A. Beige, "High error-rate quantum key distribution for long-distance communication," *New Journal of Physics,* vol. 11, no. 6, p. 063043, 2009/06/22 2009.

[96] M. Lucamarini, K. A. Patel, J. F. Dynes, B. Fröhlich, A. W. Sharpe,

A. R. Dixon, Z. L. Yuan, R. V. Penty, and A. J. Shields, "Efficient decoy-state quantum key distribution with quantified security," *Opt. Express,* vol. 21, no. 21, pp. 24550–24565, 2013/10/21 2013.

[97] N. Gisin, G. Ribordy, H. Zbinden, D. Stucki, N. Brunner, and V. Scarani, "Towards practical and fast quantum cryptography," *arXiv preprint quant-ph/0411022,* 2004.

[98] D. Stucki, N. Brunner, N. Gisin, V. Scarani, and H. Zbinden, "Fast and simple one-way quantum key distribution," *Applied Physics Letters,* vol. 87, no. 19, p. 194108, 2005/11/07 2005.

[99] T. Debuisschert and W. Boucher, "Time coding protocols for quantum key distribution," *Physical Review A,* vol. 70, no. 4, p. 042306, 2004.

[100] N. J. Cerf, M. Lévy, and G. V. Assche, "Quantum distribution of Gaussian keys using squeezed states," *Physical Review A,* vol. 63, no. 5, p. 052311, 04/18/ 2001.

[101] F. Grosshans, G. Van Assche, J. Wenger, R. Brouri, N. J. Cerf, and P. Grangier, "Quantum key distribution using gaussian-modulated coherent states," *Nature,* vol. 421, no. 6920, pp. 238–241, 2003/01/01 2003.

[102] C. Weedbrook, A. M. Lance, W. P. Bowen, T. Symul, T. C. Ralph, and P. K. Lam, "Quantum Cryptography Without Switching," *Physical Review Letters,* vol. 93, no. 17, p. 170504, 10/22/ 2004.

[103] R. García-Patrón and N. J. Cerf, "Continuous-Variable Quantum Key Distribution Protocols Over Noisy Channels," *Physical Review Letters,* vol. 102, no. 13, p. 130501, 03/31/ 2009.

[104] H.-K. Lo, M. Curty, and B. Qi, "Measurement-device-independent quantum key distribution," *Physical review*

letters, vol. 108, no. 13, p. 130503, 2012.

[105] P. Jouguet, S. Kunz-Jacques, A. Leverrier, P. Grangier, and E. Diamanti, "Experimental demonstration of long-distance continuous-variable quantum key distribution," *Nature Photonics,* vol. 7, no. 5, pp. 378–381, 2013/05/01 2013.

[106] N. Walenta, A. Burg, D. Caselunghe, J. Constantin, N. Gisin, O. Guinnard, R. Houlmann, P. Junod, B. Korzh, N. Kulesza, M. Legré, C. W. Lim, T. Lunghi, L. Monat, C. Portmann, M. Soucarros, R. T. Thew, P. Trinkler, G. Trolliet, F. Vannel, and H. Zbinden, "A fast and versatile quantum key distribution system with hardware key distillation and wavelength multiplexing," *New Journal of Physics,* vol. 16, no. 1, p. 013047, 2014/01/23 2014.

[107] K. A. Patel, J. F. Dynes, M. Lucamarini, I. Choi, A. W. Sharpe, Z. L. Yuan, R. V. Penty, and A. J. Shields, "Quantum key distribution for 10 Gb/s dense wavelength division multiplexing networks," *Applied Physics Letters,* vol. 104, no. 5, p. 051123, 2014.

[108] Y.-L. Tang, H.-L. Yin, S.-J. Chen, Y. Liu, W.-J. Zhang, X. Jiang, L. Zhang, J. Wang, L.-X. You, and J.-Y. Guan, "Measurement-device-independent quantum key distribution over 200 km," *Physical review letters,* vol. 113, no. 19, p. 190501, 2014.

[109] B. Korzh, C. C. W. Lim, R. Houlmann, N. Gisin, M. J. Li, D. Nolan, B. Sanguinetti, R. Thew, and H. Zbinden, "Provably secure and practical quantum key distribution over 307 km of optical fibre," *Nature Photonics,* vol. 9, no. 3, pp. 163–168, 2015/03/01 2015.

[110] D. Huang, D. Lin, C. Wang, W. Liu, S. Fang, J. Peng, P. Huang, and G. Zeng, "Continuous-variable quantum key distribution

with 1 Mbps secure key rate," *Opt. Express,* vol. 23, no. 13, pp. 17511–17519, 2015/06/29 2015.

[111] H.-L. Yin, T.-Y. Chen, Z.-W. Yu, H. Liu, L.-X. You, Y.-H. Zhou, S.-J. Chen, Y. Mao, M.-Q. Huang, and W.-J. Zhang, "Measurement-device-independent quantum key distribution over a 404 km optical fiber," *Physical review letters,* vol. 117, no. 19, p. 190501, 2016.

[112] Z. Yuan, A. Plews, R. Takahashi, K. Doi, W. Tam, A. W. Sharpe, A. R. Dixon, E. Lavelle, J. F. Dynes, A. Murakami, M. Kujiraoka, M. Lucamarini, Y. Tanizawa, H. Sato, and A. J. Shields, "10-Mb/s Quantum Key Distribution," *Journal of Lightwave Technology,* vol. 36, no. 16, pp. 3427–3433, 2018.

[113] S. Wang, D.-Y. He, Z.-Q. Yin, F.-Y. Lu, C.-H. Cui, W. Chen, Z. Zhou, G.-C. Guo, and Z.-F. Han, "Beating the Fundamental Rate-Distance Limit in a Proof-of-Principle Quantum Key Distribution System," *Physical Review X,* vol. 9, no. 2, p. 021046, 06/04/ 2019.

[114] X.-T. Fang, P. Zeng, H. Liu, M. Zou, W. Wu, Y.-L. Tang, Y.-J. Sheng, Y. Xiang, W. Zhang, H. Li, Z. Wang, L. You, M.-J. Li, H. Chen, Y.-A. Chen, Q. Zhang, C.-Z. Peng, X. Ma, T.-Y. Chen, and J.-W. Pan, "Implementation of quantum key distribution surpassing the linear rate-transmittance bound," *Nature Photonics,* vol. 14, no. 7, pp. 422–425, 2020/07/01 2020.

[115] H. Liu, C. Jiang, H.-T. Zhu, M. Zou, Z.-W. Yu, X.-L. Hu, H. Xu, S. Ma, Z. Han, J.-P. Chen, Y. Dai, S.-B. Tang, W. Zhang, H. Li, L. You, Z. Wang, Y. Hua, H. Hu, H. Zhang, F. Zhou, Q. Zhang, X.-B. Wang, T.-Y. Chen, and J.-W. Pan, "Field Test of Twin-Field Quantum Key Distribution through Sending-or-Not-Sending over 428 km," *Physical Review Letters,* vol. 126, no. 25, p.

250502, 06/22/ 2021.

[116] J.-P. Chen, C. Zhang, Y. Liu, C. Jiang, W.-J. Zhang, Z.-Y. Han, S.-Z. Ma, X.-L. Hu, Y.-H. Li, H. Liu, F. Zhou, H.-F. Jiang, T.-Y. Chen, H. Li, L.-X. You, Z. Wang, X.-B. Wang, Q. Zhang, and J.-W. Pan, "Twin-field quantum key distribution over a 511 km optical fibre linking two distant metropolitan areas," *Nature Photonics,* vol. 15, no. 8, pp. 570–575, 2021/08/01 2021.

[117] L. Li, T. Wang, X. Li, P. Huang, Y. Guo, L. Lu, L. Zhou, and G. Zeng, "Continuous-variable quantum key distribution with on-chip light sources," *Photon. Res.,* vol. 11, no. 4, pp. 504–516, 2023/04/01 2023.

[118] T. Wang, P. Huang, L. Li, y. zhou, and G. Zeng, "High key rate continuous-variable quantum key distribution using telecom optical components," *New Journal of Physics,* 2024.

[119] M. Avesani, L. Calderaro, M. Schiavon, A. Stanco, C. Agnesi, A. Santamato, M. Zahidy, A. Scriminich, G. Foletto, G. Contestabile, M. Chiesa, D. Rotta, M. Artiglia, A. Montanaro, M. Romagnoli, V. Sorianello, F. Vedovato, G. Vallone, and P. Villoresi, "Full daylight quantum-key-distribution at 1550 nm enabled by integrated silicon photonics," *npj Quantum Information,* vol. 7, no. 1, p. 93, 2021/06/08 2021.

[120] Y.-H. Li, S.-L. Li, X.-L. Hu, C. Jiang, Z.-W. Yu, W. Li, W.-Y. Liu, S.-K. Liao, J.-G. Ren, H. Li, L. You, Z. Wang, J. Yin, F. Xu, Q. Zhang, X.-B. Wang, Y. Cao, C.-Z. Peng, and J.-W. Pan, "Free-Space and Fiber-Integrated Measurement-Device-Independent Quantum Key Distribution under High Background Noise," *Physical Review Letters,* vol. 131, no. 10, p. 100802, 09/06/ 2023.

[121] F. Honz, M. Hentschel, P. Walther, H. Hübel, and B. Schrenk, "Solar-Blind QKD over Simplified Short-Range FSO Link," in

2024 Optical Fiber Communications Conference and Exhibition (OFC), 24–28 March 2024 2024, pp. 1–3.

[122] Y. Li, P. N. Nesterenko, B. Paull, R. Stanley, and M. Macka, "Performance of a New 235 nm UV-LED-Based On-Capillary Photometric Detector," *Analytical Chemistry,* vol. 88, no. 24, pp. 12116–12121, 2016/12/20 2016.

[123] T. Olatunde, R. Shelley, A. Chilton, P. Serra, G. Ciani, G. Mueller, and J. Conklin, "240 nm UV LEDs for LISA test mass charge control," *Journal of Physics: Conference Series,* vol. 610, p. 012034, 2015/05/11 2015.

[124] J. Hill, C. Chen, E. Xie, J. J. D. McKendry, J. Herrnsdorf, E. Gu, H. Haas, and M. D. Dawson, "Effects of LED Device Size on UV-C Short-Range LoS Optical Wireless Communication," *IEEE Photonics Journal,* vol. 15, no. 6, pp. 1–8, 2023.

[125] J. J. D. McKendry, E. Xie, J. Hill, H. Zimi, J. Herrnsdorf, E. Gu, R. K. Henderson, and M. D. Dawson, "Deep Ultraviolet CMOS-Controlled Micro Light-Emitting Diode Array," *IEEE Photonics Journal,* pp. 1–6, 2023.

[126] R. H. Hadfield, "Single-photon detectors for optical quantum information applications," *Nature Photonics,* vol. 3, no. 12, pp. 696–705, 2009/12/01 2009.

[127] F. Ceccarelli, G. Acconcia, A. Gulinatti, M. Ghioni, I. Rech, and R. Osellame, "Recent Advances and Future Perspectives of Single-Photon Avalanche Diodes for Quantum Photonics Applications," *Advanced Quantum Technologies,* vol. 4, no. 2, p. 2000102, 2021/02/01 2021.

[128] E. E. Wollman, V. B. Verma, A. D. Beyer, R. M. Briggs, B. Korzh, J. P. Allmaras, F. Marsili, A. E. Lita, R. P. Mirin, S. W. Nam, and M. D. Shaw, "UV superconducting nanowire single-photon

detectors with high efficiency, low noise, and 4 K operating temperature," *Opt. Express,* vol. 25, no. 22, pp. 26792–26801, 2017/10/30 2017.

[129] L. Su, D. Zhou, H. Lu, R. Zhang, and Y. Zheng, "Recent progress of SiC UV single photon counting avalanche photodiodes," *Journal of Semiconductors,* vol. 40, no. 12, p. 121802, 2019/12/01 2019.

[130] A. Vert, S. Soloviev, J. Fronheiser, and P. Sandvik, "Solar-Blind 4H-SiC Single-Photon Avalanche Diode Operating in Geiger Mode," *IEEE Photonics Technology Letters,* vol. 20, no. 18, pp. 1587–1589, 2008.

[131] L. Li, D. Zhou, F. Liu, H. Lu, F. Ren, D. Chen, R. Zhang, and Y. Zheng, "High Fill-Factor 4H-SiC Avalanche Photodiodes With Partial Trench Isolation," *IEEE Photonics Technology Letters,* vol. 28, no. 22, pp. 2526–2528, 2016.

[132] E. Cicek, Z. Vashaei, R. McClintock, C. Bayram, and M. Razeghi, "Geiger-mode operation of ultraviolet avalanche photodiodes grown on sapphire and free-standing GaN substrates," *Applied Physics Letters,* vol. 96, no. 26, 2010.

[133] "Silicon Photomultiplier Sensors, J-Series (SiPM)." Onsemi. [Online].Available: https://www.onsemi.com/products/sensors/photodetectors-sipm-spad/silicon-photomultipliers-sipm/j-series.

[134] C. W. Chow, C. H. Yeh, Y. Liu, Y. Lai, L. Y. Wei, C. W. Hsu, G. H. Chen, X. L. Liao, and K. H. Lin, "Enabling Techniques for Optical Wireless Communication Systems," in *2020 Optical Fiber Communications Conference and Exhibition (OFC)*, 8–12 March 2020 2020, pp. 1–3.

[135] X. Chen, F. Ren, S. Gu, and J. Ye, "Review of gallium-oxide-

based solar-blind ultraviolet photodetectors," *Photon. Res.,* vol. 7, no. 4, pp. 381–415, 2019/04/01 2019.

[136] J. Lu, Z. Lv, X. Qiu, S. Lai, and H. Jiang, "Ultrasensitive and high-speed AlGaN/AlN solar-blind ultraviolet photodetector: a full-channel-self-depleted phototransistor by a virtual photogate," *Photon. Res.,* vol. 10, no. 9, pp. 2229–2238, 2022/09/01 2022.

[137] K. Wang, X. Qiu, Z. Lv, Z. Song, and H. Jiang, "Ultrahigh detectivity, high-speed and low-dark current AlGaN solar-blind heterojunction field-effect phototransistors realized using dual-float-photogating effect," *Photon. Res.,* vol. 10, no. 1, pp. 111–119, 2022/01/01 2022.

[138] G. Shen, Z. Liu, C.-K. Tan, M. Jiang, S. Li, Y. Guo, and W. Tang, "Solar-blind UV communication based on sensitive β-Ga2O3 photoconductive detector array," *Applied Physics Letters,* vol. 123, no. 4, 2023.

[139] C. Lin, Y. Lu, Y. Tian, C. Gao, M. Fan, X. Yang, L. Dong, and C. Shan, "Diamond based photodetectors for solar-blind communication," *Opt. Express,* vol. 27, no. 21, pp. 29962–29971, 2019/10/14 2019.

[140] U. Varshney, N. Aggarwal, and G. Gupta, "Current advances in solar-blind photodetection technology: Using Ga 2 O 3 and AlGaN," *Journal of Materials Chemistry C,* vol. 10, no. 5, pp. 1573–1593, 2022.

[141] Q. Cai, H. You, H. Guo, J. Wang, B. Liu, Z. Xie, D. Chen, H. Lu, Y. Zheng, and R. Zhang, "Progress on AlGaN-based solar-blind ultraviolet photodetectors and focal plane arrays," *Light: Science & Applications,* vol. 10, no. 1, p. 94, 2021/04/30 2021.

[142] O. Alkhazragi, F. Hu, P. Zou, Y. Ha, Y. Mao, T. K. Ng, N. Chi, and

B. S. Ooi, "2.4-Gbps Ultraviolet-C Solar-Blind Communication Based on Probabilistically Shaped DMT Modulation," in *Optical Fiber Communication Conference (OFC) 2020*, San Diego, California, 2020/03/08 2020: Optica Publishing Group, in OSA Technical Digest, p. M3I.5.

[143] K. Kojima, Y. Yoshida, M. Shiraiwa, Y. Awaji, A. Kanno, N. Yamamoto, and S. Chichibu, "1.6-Gbps LED-Based Ultraviolet Communication at 280 nm in Direct Sunlight," in *2018 European Conference on Optical Communication (ECOC)*, 23–27 Sept. 2018 2018, pp. 1–3.

[144] Y. Yoshida, K. Kojima, M. Shiraiwa, Y. Awaji, A. Kanno, N. Yamamoto, S. F. Chichibu, A. Hirano, and M. Ippommatsu, "An Outdoor Evaluation of 1-Gbps Optical Wireless Communication using AlGaN-based LED in 280-nm Band," in *2019 Conference on Lasers and Electro-Optics (CLEO)*, 5–10 May 2019 2019, pp. 1–2.

[145] *BS EN 62471: Photobiological safety of lamps and lamp systems*, E. C. f. E. Standardization, 2008.

[146] S. Zhu, P. Qiu, Z. Qian, X. Shan, Z. Wang, K. Jiang, X. Sun, X. Cui, G. Zhang, D. Li, and P. Tian, "2 Gbps free-space ultraviolet-C communication based on a high-bandwidth micro-LED achieved with pre-equalization," *Optics Letters,* vol. 46, no. 9, pp. 2147–2150, 2021/05/01 2021.

[147] D. M. Maclure, J. J. D. McKendry, M. S. Islim, E. Xie, C. Chen, X. Sun, X. Liang, X. Huang, H. Abumarshoud, J. Herrnsdorf, E. Gu, H. Haas, and M. D. Dawson, "10 Gbps wavelength division multiplexing using UV-A, UV-B, and UV-C micro-LEDs," *Photon. Res.,* vol. 10, no. 2, pp. 516–523, 2022/02/01 2022.

[148] W. Ali, R. Chen, M. Crisp, and R. V. Penty, "8.2 Gbps Optical

Wireless Link using SiPM at NIR Wavelength," *Journal of Lightwave Technology,* pp. 1–6, 2023.

[149] W. Matthews, Z. Ahmed, W. Ali, and S. Collins, "A 3.45 Gigabits/s SiPM-Based OOK VLC Receiver," *IEEE Photonics Technology Letters,* vol. 33, no. 10, pp. 487–490, 2021.

[150] S. Huang, C. Chen, R. Bian, H. Haas, and M. Safari, "5 Gbps optical wireless communication using commercial SPAD array receivers," *Optics Letters,* vol. 47, no. 9, pp. 2294–2297, 2022/05/01 2022.

[151] C. Bruschini, H. Homulle, I. M. Antolovic, S. Burri, and E. Charbon, "Single-photon avalanche diode imagers in biophotonics: review and outlook," *Light: Science & Applications,* vol. 8, no. 1, p. 87, 2019/09/18 2019.

[152] J. Riu, M. Sicard, S. Royo, and A. Comerón, "Silicon photomultiplier detector for atmospheric lidar applications," *Optics Letters,* vol. 37, no. 7, pp. 1229–1231, 2012/04/01 2012.

[153] A. N. Otte, D. Garcia, T. Nguyen, and D. Purushotham, "Characterization of three high efficiency and blue sensitive silicon photomultipliers," *Nuclear Instruments and Methods in Physics Research Section A: Accelerators, Spectrometers, Detectors and Associated Equipment,* vol. 846, pp. 106–125, 2017/02/21/ 2017.

[154] "MPPC Technical Note." HAMAMATSU. [Online]. Available: https://www.hamamatsu.com/content/dam/hamamatsu-photonics/sites/documents/99_SALES_LIBRARY/ssd/mppc_kapd9008e.pdf.

[155] E. Sarbazi, M. Safari, and H. Haas, "The Bit Error Performance and Information Transfer Rate of SPAD Array Optical

Receivers," *IEEE Transactions on Communications,* vol. 68, no. 9, pp. 5689–5705, 2020.

[156] P. Horowitz and W. Hill, *The art of electronics*. Cambridge university press Cambridge, 2015.

[157] G.-J. Fan-Yuan, C. Wang, S. Wang, Z.-Q. Yin, H. Liu, W. Chen, D.-Y. He, Z.-F. Han, and G.-C. Guo, "Afterpulse Analysis for Quantum Key Distribution," *Physical Review Applied,* vol. 10, no. 6, p. 064032, 12/13/ 2018.

[158] D. Hall, Y. H. Liu, L. Yan, Y. Yu, and Y. H. Lo, "Approaching the Quantum Limit of Photodetection in Solid-State Photodetectors," *IEEE Transactions on Electron Devices,* vol. 64, no. 12, pp. 4812–4822, 2017.

[159] W. Matthews, W. Ali, Z. Ahmed, G. Faulkner, and S. Collins, "Inter-Symbol Interference and Silicon Photomultiplier VLC Receivers in Ambient Light," *IEEE Photonics Technology Letters,* vol. 33, no. 9, pp. 449–452, 2021.

[160] H. Hao, Q.-Y. Zhao, Y.-H. Huang, J. Deng, F. Yang, S.-Y. Ru, Z. Liu, C. Wan, H. Liu, Z.-J. Li, H.-B. Wang, X.-C. Tu, L.-B. Zhang, X.-Q. Jia, X.-L. Wu, J. Chen, L. Kang, and P.-H. Wu, "A compact multi-pixel superconducting nanowire single-photon detector array supporting gigabit space-to-ground communications," *Light: Science & Applications,* vol. 13, no. 1, p. 25, 2024/01/22 2024.

[161] J. A. Mendenhall, L. M. Candell, P. I. Hopman, G. Zogbi, D. M. Boroson, D. O. Caplan, C. J. Digenis, D. R. Hearn, and R. C. Shoup, "Design of an Optical Photon Counting Array Receiver System for Deep-Space Communications," *Proceedings of the IEEE,* vol. 95, no. 10, pp. 2059–2069, 2007.

[162] H. Kaushal and G. Kaddoum, "Optical Communication in

Space: Challenges and Mitigation Techniques," *IEEE Communications Surveys & Tutorials,* vol. 19, no. 1, pp. 57–96, 2017.

[163] P. Tian, X. Shan, S. Zhu, E. Xie, J. J. D. McKendry, E. Gu, and M. D. Dawson, "AlGaN Ultraviolet Micro-LEDs," *IEEE Journal of Quantum Electronics,* vol. 58, no. 4, pp. 1–14, 2022.

[164] T. Lu, X. Lin, W. Guo, C.-C. Tu, S. Liu, C.-J. Lin, Z. Chen, H.-C. Kuo, and T. Wu, "High-speed visible light communication based on micro-LED: A technology with wide applications in next generation communication," *Opto-Electronic Science,* vol. 1, no. 12, pp. 220020–1–220020–24, 2022.

[165] X. He, E. Xie, M. S. Islim, A. A. Purwita, J. J. D. McKendry, E. Gu, H. Haas, and M. D. Dawson, "1 Gbps free-space deep-ultraviolet communications based on III-nitride micro-LEDs emitting at 262 nm," *Photon. Res.,* vol. 7, no. 7, pp. B41–B47, 2019/07/01 2019.

[166] D. M. Maclure, C. Chen, J. J. D. McKendry, E. Xie, J. Hill, J. Herrnsdorf, E. Gu, H. Haas, and M. D. Dawson, "Hundred-meter Gb/s deep ultraviolet wireless communications using AlGaN micro-LEDs," *Opt. Express,* vol. 30, no. 26, pp. 46811–46821, 2022/12/19 2022.

[167] M.-T. Chen, M.-P. Lu, Y.-J. Wu, J. Song, C.-Y. Lee, M.-Y. Lu, Y.-C. Chang, L.-J. Chou, Z. L. Wang, and L.-J. Chen, "Near UV LEDs Made with in Situ Doped p-n Homojunction ZnO Nanowire Arrays," *Nano Letters,* vol. 10, no. 11, pp. 4387–4393, 2010/11/10 2010.

[168] C.-H. Lin and C.-T. Lee, "Ga2O3-based solar-blind deep ultraviolet light-emitting diodes," *Journal of Luminescence,* vol. 224, p. 117326, 2020/08/01/ 2020.

[169] L. Wang, Q. Guo, J. Duan, W. Xie, G. Ji, S. Li, C. Chen, J. Li, L. Yang, Z. Tan, L. Xu, Z. Xiao, J. Luo, and J. Tang, "Exploration of Nontoxic Cs3CeBr6 for Violet Light-Emitting Diodes," *ACS Energy Letters,* vol. 6, no. 12, pp. 4245–4254, 2021/12/10 2021.

[170] G. Brisebois. "Op Amp Combines Femtoamp Bias Current with 4GHz Gain Bandwidth Product, Shines New Light on Photonics Applications." Analog Devices. [Online]. Available: https://www.analog.com/cn/resources/technical-articles/op-amp-combines-femtoamp-bias-current-with-4ghz-gain-bandwidth-product.html.

[171] H. Hashemi. "Transimpedance Amplifiers (TIA): Choosing the BestAmplifier for the Job." Texas Instruments. [Online]. Available: https://www.tij.co.jp/jp/lit/an/snoa942a/snoa942a.pdf.

[172] "Convective Heat Transfer Coefficient." Nuclear Power. [Online]. Available: https://www.nuclear-power.com/nuclear-engineering/heat-transfer/convection-convective-heat-transfer/convective-heat-transfer-coefficient/.

[173] M. C. Gursoy, M. Nasiri-Kenari, and U. Mitra, "Towards high data-rate diffusive molecular communications: A review on performance enhancement strategies," *Digital Signal Processing,* vol. 124, p. 103161, 2022/05/01/ 2022.

[174] M. C. Gursoy and U. Mitra, "Higher Order Derivatives: Improved Pre-Processing and Receivers for Molecular Communications," in *GLOBECOM 2020 - 2020 IEEE Global Communications Conference*, 7–11 Dec. 2020 2020, pp. 1–6.

[175] Z. Zeng, S. Fu, H. Zhang, Y. Dong, and J. Cheng, "A Survey of Underwater Optical Wireless Communications," *IEEE*

2
3

Communications Surveys & Tutorials, vol. 19, no. 1, pp. 204–238, 2017.

[176] F. A. Mendonça, D. B. de Brito, J. B. R. Silva, G. A. P. Thé, and R. V. Ramos, "Experimental implementation of B92 quantum key distribution protocol," *Microwave and Optical Technology Letters,* vol. 50, no. 1, pp. 236–241, 2008.

[177] M. Canale, D. Bacco, S. Calimani, F. Renna, N. Laurenti, G. Vallone, and P. Villoresi, "A prototype of a free-space QKD scheme based on the B92 protocol," presented at the Proceedings of the 4th International Symposium on Applied Sciences in Biomedical and Communication Technologies, Barcelona, Spain, 2011.

[178] R. Chatterjee, K. Joarder, S. Chatterjee, B. C. Sanders, and U. Sinha, "qkdSim, a Simulation Toolkit for Quantum Key Distribution Including Imperfections: Performance Analysis and Demonstration of the B92 Protocol Using Heralded Photons," *Physical Review Applied,* vol. 14, no. 2, p. 024036, 08/13/ 2020.

[179] A. Dutta, Muskan, S. Banerjee, and A. Pathak, "Analysis for Satellite-Based High-Dimensional Extended B92 and High-Dimensional BB84 Quantum Key Distribution," *Advanced Quantum Technologies,* vol. 7, no. 11, p. 2400149, 2024.

[180] E. Zhang and F. Liu, *Free space B92 quantum key distribution analysis under different atmospheric conditions* (Applied Optics and Photonics China 2024 (AOPC2024)). SPIE, 2024.

[181] N. Lütkenhaus, "Security against individual attacks for realistic quantum key distribution," *Physical Review A,* vol. 61, no. 5, p. 052304, 04/06/ 2000.

[182] X. Ma, "Unconditional security at a low cost," *Physical Review*

A, vol. 74, no. 5, p. 052325, 11/16/ 2006.

[183] C. E. Shannon, "A mathematical theory of communication," *The Bell System Technical Journal,* vol. 27, no. 3, pp. 379–423, 1948.

[184] G. Brassard and L. Salvail, "Advances in Cryptology—EUROCRYPT’93," *Lecture Notes in Computer Science,* vol. 765, pp. 410–423, 1994.

[185] J. L. Carter and M. N. Wegman, "Universal classes of hash functions (Extended Abstract)," presented at the Proceedings of the ninth annual ACM symposium on Theory of computing, Boulder, Colorado, USA, 1977.

[186] C. Database, "CIE “physiologically-relevant” luminous efficiency functions consistent with the Stockman & Sharpe cone fundamentals, 2-deg functions," ed: UCL Institute of Ophthalmology London.

[187] C. I. d. l’Éclairage, "Commission internationale de l’eclairage proceedings," ed: Cambridge University Press Cambridge, 1931.

[188] P. R. Michael, D. E. Johnston, and W. Moreno, "A conversion guide: solar irradiance and lux illuminance," *Journal of Measurements in Engineering,* vol. 8, no. 4, pp. 153–166, 2020.

[189] D. Han, Y. Liu, K. Zhang, P. Luo, and M. Zhang, "Theoretical and experimental research on diversity reception technology in NLOS UV communication system," *Opt. Express,* vol. 20, no. 14, pp. 15833–15842, 2012/07/02 2012.

[190] G. Shaw, A. Siegel, J. Model, and D. Greisokh, *Recent progress in short-range ultraviolet communication* (Defense and Security). SPIE, 2005.

[191] "Silicon Photomultipliers (SiPM), C-SERIES." Onsemi. [Online].Available: https://www.onsemi.com/products/sensors/photodetectors-sipm-spad/silicon-photomultipliers-sipm/c-series.

[192] L. Zhou, D. Lowndes, V. Lee, I. Mitra, T. S. G, J. Rarity, G. Faulkner, and D. O. Brien, "Polarization Calibration Scheme for a Practical Handheld Free Space Quantum Key Distribution Link," in *2019 IEEE Globecom Workshops (GC Wkshps)*, 9–13 Dec. 2019 2019, pp. 1–5.

[193] R. Singh, A. Schreier, G. Faulkner, and D. O’Brien, "Fiber-Wireless-Fiber Terminals for Optical Wireless Communication over Multiple Bands," in *2020 IEEE Photonics Conference (IPC)*, 28 Sept.–1 Oct. 2020 2020, pp. 1–2.

[194] D. Lowndes, A. Schreier, D. O'Brien, and J. Rarity, *Characterising a handheld quantum key distribution system with emulated beam steering* (SPIE Photonex). SPIE, 2021.

[195] A. Schreier, J. Sagar, D. Lowndes, H. Chun, S. K. Joshi, G. Faulkner, J. Rarity, and D. O. Brien, "A beam steering platform enabling handheld low-cost quantum key distribution," in *49th European Conference on Optical Communications (ECOC 2023)*, 1–5 Oct. 2023 2023, vol. 2023, pp. 495–498.